UNIVERSITY OF CALIFORNIA
Merced

Effects of heat and mass transport on the hydrodynamics and stability of liquid desiccant films

A Dissertation submitted in partial satisfaction
of the requirements for the degree of

Doctor of Philosophy

in

Mechanical Engineering and Applied Mechanics

by

Sergio M. Pineda Vargas

Committee in Charge:

Professor Roland Winston, Chair

Professor Carlos Coimbra

Professor Gerardo Diaz

May 2013

The Dissertation of
Sergio M. Pineda Vargas is approved:

Professor Carlos Coimbra

Professor Gerardo Diaz

Professor Roland Winston, Committee Chairperson

March 2013

Effects of heat and mass transport on the hydrodynamics and stability of liquid desiccant films

by

Sergio M. Pineda Vargas

To my lovely wife Sandra and my boys Juan Manuel and Manuel Fernando, my life and soul. To the whole big Pineda family and to the spirit of the Pinelopiadas.

Acknowledgements

I wish to express my sincere gratitude to my adviser Gerardo Diaz for his continued support and patience. I am grateful to Professor Roland Winston and Professor Carlos Coimbra for the care with which they reviewed the original manuscript. I am particularly grateful to Neeraj Sharma for his thoughtful and creative comments, and more generally for exploring with me the boundaries of professional friendship.

Curriculum Vitæ
Sergio M. Pineda Vargas

Education

2009	Master of Science in Mechanical Engineering and Applied Mechanics, University of California, Merced.
2000	Bachelor of Civil Engineering, Universidad Industrial de Santander, Colombia.

Experience

2011	Sergio M. Pineda and Gerardo Diaz, Contribution of an internal heat exchanger to the performance of a liquid desiccant dehumidifier operating near freezing conditions, published online, 13 July 2011. International Journal of Thermal Sciences, 50 (2011) 2304-2310.
2011	Sergio M. Pineda, Gerardo Diaz and Carlos F.M. Combra. Approximation of transient 1D Conduction in a Finite Domain Using Parametric Fractional Derivatives, published July 2011. Journal of Heat Transfer. ASME.
2010	S.M. Pineda and G. Diaz, Performance of an adiabatic cross-ow liquid desiccant absorber inside a refrigerated warehouse, International Journal of Refrigeration, received 5 November 2009, revised 27 July 2010, accepted 10 August 2010. Available online 19 August 2010.
2009	S.M. Pineda and G. Diaz, Analysis of Heat and Mass Transfer of an Adiabatic Cross-ow Liquid Desiccant Absorber Operating at Low Temperature, Proceedings of ASME Summer Heat Transfer Conference, Paper # HT2009-88255, pp. 1-9, San Francisco, July 2009.
2009 – 2012	Teaching Assistant, University of California, Merced.
2006 – 2009	Graduate Research Assistant, University of California, Merced.
2000 – 2005	Graduate Research Assistant, UIS, Colombia.

Abstract

Effects of heat and mass transport on the hydrodynamics and stability of liquid desiccant films

Sergio M. Pineda Vargas

The continuous increase in the demand of energy and the high costs of fuels in many areas in the world are fostering improvements in energy efficiency in many sectors. Defrosting due to ice formation on the surface of cooling coils is a major source of inefficiencies in the refrigerated warehouse sector which, just in California, accounts for 1,800 million kWh of energy consumption per year. Liquid desiccants have been identified as a means of reducing latent loads in air conditioning and refrigeration systems. However, the interaction of liquid desiccant films and humid air is a subject that has not been analyzed in detail. In the past, significant efforts have been made in understanding liquid-film absorption processes in heat and mass exchangers for several flow configurations, using various numerical and experimental techniques. However, studies concerning liquid desiccant films near freezing conditions with coupled momentum, heat and mass transfer using non-isothermal thermo-physical properties are rare in the literature. The purpose of this dissertation is to investigate the effect of heat and mass transfer in the interaction of a liquid desiccant film in contact with a humid air stream. Velocity, temperature, and concentration distributions, as well as, film stability are studied experimentally and numerically. The results show a delay in the formation of the ice on the cooling coil due to the reduction of the dew point temperature of the evaporator inlet air, thus reducing operating costs. Moreover, the results show that an effectiveness of the internal heat exchanger less than 60% leads to a desorption process which is opposite to the aims of the dehumidification system. The stability analysis of the liquid film is evaluated using the Orr-Sommerfeld equation with methodologies such as the small wavenumber technique and complete orthonormalization method. Most works found in the literature have focused on the particularly simplified cases of absorption with uniform properties, namely, isothermal systems. The techniques used to analyze film stability allow the inclusion of the effects of heat, mass, and temperature dependent properties, which constitutes a major contribution of this work. Stabilizing and de-stabilizing effects of different parameters are discussed in the results.

Contents

List of Figures

List of Tables

Nomenclature

C	concentration of liquid desiccant (kg_w kg_{sol}^{-1})
Cc	calcium chloride concentration in the desiccant film (kg_{CaCl_2} kg_{sol}^{-1})
COP	coefficient of performance
Cp	specific heat (kJ kg^{-1} K^{-1})
D	relationship between viscosity and local geometry of the control volume
$\mathcal{D}$	diffusion coefficient (m^2 s^{-1})
F	conservative fluxes
fs	cavity width or wall spacing in Chapter 3 (m)
g	gravitational acceleration (m s^{-2})
H	wall height in Chapter 3 and 4. Wall spacing in Chapter 5 (m)
h_{gf}	enthalpy of condensation (kJ kg^{-1})
k	thermal conductivity (W m^{-2} K^{-1})
L	wall width in Chapter 3 and wall length in Chapter 5 (m)
Le	Lewis number
$\dot{m}$	mass flow rate (kg s^{-1})
Nu	Nusselt number
p	pressure (Pa)
p_t	total pressure (Pa)
p_v	vapor pressure (Pa)
p_{v,H_2O}	water vapor pressure (Pa)
Pe	Peclet number
Pr	Prandtl number
$\dot{Q}$	heat transfer rate (kW)
Re	Reynolds number
RH	relative humidity (%)
Sh	Sherwood number
Sc	Schmidt number
T	temperature (°C)
U	nondimensional velocity in the $X-$direction
u	velocity in the $x-$direction (m s^{-1})
V	nondimensional velocity in the $y-$direction
v	velocity in the $y-$direction (m s^{-1})
W	humidity ratio of the air in Chapters 3 and 5 (kg_w kg_{da}^{-1})
X	nondimensional $x-$coordinate
x	$x-$coordinate
Y	nondimensional $y-$coordinate
y	$y-$coordinate
z	$z-$coordinate

Greek Letters

α	thermal diffusivity ($m^2\ s^{-1}$)
δ	subdomain thickness (m)
ϵ	effectiveness
μ	dynamic viscosity (Pa s)
ν	kinematic viscosity ($m^2\ s^{-1}$)
τ	shear stress ($N\ m^{-2}$)
ρ	density ($kg\ m^{-3}$)
ω	humidity ratio ($kg_w\ kg_{da}^{-1}$)
Δ	diference operator
Θ	normalized temperature
Λ	normalized concentration

Subscripts and superscripts

a	air subdomain
Abs	absorber
avg	average
da	dry air
i	initial condition
IHX	internal heat exchanger
int	interfacial region
l	liquid subdomain
ld	liquid desiccant subdomain
m	mass or moisture
max	maximum value
me	mean value
min	minimum value
w	water species
wb	water bulk

Chapter 1

Introduction

The break-up of a liquid desiccant film due to instabilities induced by shear stresses and local property changes at the liquid and humid-air interface near freezing temperatures, is a subject rarely addressed in the literature due to the complexity of this two-phase flow problem [1, 2], and the relatively lack of interest in dehumidifying technologies that has prevailed for many years [3, 4]. The complexity lies in the existence of the interface between the two fluid phases and on the deformation and continuous shape change due to the acting stresses [5]. Furthermore, several discontinuities at the interface need to be considered in order to analyze limiting cases [6]. However, a rising interest in the desiccant systems has appeared recently as a way of reducing the latent load on air conditioning systems, helping with the reduction of both energy and water consumption in industrial applications such as refrigerated warehouses [7–10]. The solution of the coupled momentum, energy and mass transfer equations by using computational methods, such as, finite differences or finite volumes [11] gives us the possibility of obtaining a non-isothermal solution in order to analyze the effects of the non-uniform properties in the stability of the liquid desiccant film by using small disturbance stability analysis procedures [12]. This work includes both experimental and theoretical studies of the interaction of a liquid desiccant film and a stream of humid air. Chapters two, three and four are related to the experimental work; Conversely, chapters five and six it show more theoretical numerical approximations. Chapters 2, 3 and 4 have been published [13–15], and Chapters 5 and 6 will be submitted for publishing consideration.

1.1 Refrigerated Warehouses

Projections of the energy consumption around the world predict an increase in the demand of energy of approximately 50% from 2005 to 2030 having fossil fuels as the main energy source [16]. Industrial applications such as refrigerated warehouses are responsible for 20% of the total electric energy consumption of the food industry in California [17]. Fostering improvements in the efficient use of electricity combined with innovative technologies have become pillars of the sustainable growth of communities by helping to reduce energy consumption and green house gas emissions.

A refrigerated warehouse works as a traditional vapor compression refrigeration cycle, where the evaporator is located inside the cold storage, and where sensible and latent heat are removed from the indoor air to lower the temperature of the produce inside the warehouse. Humid operating conditions translate into a continuous formation of ice on the surface of the evaporator which is usually removed by means of running defrosting cycles, where water is sprayed on the surface of the evaporator to melt the ice. Thus, at the end of the defrosting cycle the surface of the evaporator is near the temperature of the inlet water and the compressors are run to bring the temperature of the evaporator surface back to its design conditions. This procedure is inefficient and involves the use of large quantities of water to defrost the cooling coils. More importantly, such procedure can be avoided by the implementation of a dehumidifying system.

1.2 Liquid desiccant systems

In the past, solid desiccant systems were implemented to deal with the latent heat inside of the warehouse, but they were not suitable for the direct elimination of frost from the cooling coils. Liquid desiccant systems have the capability of providing localized dehumidification since the regeneration stage can be located far away from the dehumidification zone. Liquid desiccants are natural or synthetic substances capable of absorbing moisture from the air due to the difference of vapor pressure between the surrounding air and the desiccant surface [13]. Concentrated solutions of liquid desiccants are often sprayed into air streams or applied as falling films on the surface of dehumidifiers to absorb water vapor from the incoming air [18, 19]. The diluted liquid desiccant solution is then pumped to a regeneration stage where heat is applied to reject the moisture content of the solution, increasing its desiccant concentration. The concentrated desiccant solution is pumped back to the absorber to repeat the cycle. Numerical model-

ing of the liquid desiccant film helps us to understand the experimental data and formulate theoretical approximations.

1.3 Numerical simulations of liquid films

In the present work, the heat, mass, and momentum transfer equations are solved numerically for an incompressible, two-dimensional, parallel flow between a humid air stream and a liquid desiccant film, by using the finite difference and finite volume methods. Heat and mass exchange analyses in liquid films considering prescribed velocity profiles or computing hydrodynamics for an isothermal fluid flow are common in literature [18, 20–23] however, the combining effects of momentum, heat and mass transport are rarely treated [24, 25], even less for systems with temperature dependent properties [26, 27]. A staggered grid is used to discretize the domain together with a semi-implicit pressure linked algorithm to solve the governing equations.

1.4 Stability of liquid desiccant films

The procedure for small disturbance is used as the central structure for stability analysis of one-phase and two-phase flows. The derivations of the disturbance differential equations that govern the problem are shown for both cases, including several forms of the simplified O-S relation. Various methodologies to deal with the governing equations are taken. However, two of them are chosen to solve the effects of the heat and mass transport such as the small wavenumber technique [28] and the complete orthonormalization technique [29]. The small wavenumber technique is suitable for one and two-phase flows with average property profiles, but here it is used to solve the two-phase flow stability problem, after the effect of the heat and mass transfer have been included to compute hydrodynamic profiles. The complete orthonormalization technique is also able to solve one and two-phase flows, but it has the advantage to include directly the distribution of the properties in the colocation points. Finally, using operational values for a liquid desiccant film and humid-air stream for an absorber, stability cases are tested in order to understand the behavior of the two-phase interaction when heat and mass transfer are included.

Chapter 2

Performance of an adiabatic cross-flow liquid-desiccant absorber inside a refrigerated warehouse

Liquid desiccant systems have been extensively studied as a way of reducing the latent load on air conditioning systems. Most of the studies have targeted the removal of moisture from air at ambient conditions. The literature about the use of liquid desiccants in low temperature applications is scarce. In this study, a small-scale liquid-desiccant absorber is installed inside a commercial refrigerated warehouse. Its performance under realistic operating conditions inside a pre-cooling room is analyzed. The results show that the dew point temperature of the air downstream of the absorber is comparable to the evaporator surface temperature suggesting the potential to delay the formation of ice on the cooling coil. An internal heat exchanger is used to lower the temperature of the inlet liquid desiccant flow to the absorber and the regeneration process is performed using only ambient air. The analysis of the reduction in water and energy consumption for a scaled-up system is also performed. Keywords: Refrigerated warehouses, liquid desiccant, defrosting cycle

2.1 Introduction

The projection of the world's market energy consumption predicts an increase in the demand of energy of approximately 50 percent from 2005 to 2030 [16]. Fossil fuels such as petroleum, natural gas and coal are likely to remain as the

main supply of the energy used worldwide until 2030. Consequently, in response to this high demand for energy, and because oil production is concentrated in a small group of countries, oil prices are expected to remain relatively high [30]. Furthermore, the increase of fossil fuel usage in the absence of national policies and/or international agreements that limit or reduce greenhouse gas emissions is expected to result in the increase of emissions from 28.1 billion metric tons in 2005 to 42.3 billion metric tons in 2030 [16]. Thus, policies that encourage more efficient use and production of energy are desperately needed.

The efficient use of electricity combined with innovative technologies are fundamental tools for reaching suitable levels of energy consumption and green house gas emissions. One example is the refrigerated warehouse sector where the energy consumption is clearly intensive and where a large potential for additional energy saving exists.

A cold storage or refrigerated warehouse works as a traditional vapor compression refrigeration cycle. In general, the evaporator is located inside the cold storage, where sensible and latent heat are removed from the indoor air to lower the temperature of the produce inside the warehouse. Heat is rejected outside of the facility by using cooling towers. In order to maintain the quality of the produce, a high relative humidity level is desired inside the cold storage. In addition, produce is transported in and out of the facility allowing hot and humid ambient air inside the warehouse. These operating conditions translate into a continuous formation of ice on the surface of the evaporator which is usually removed by means of running a defrosting cycle several times a day. In a common defrosting cycle implementation, water is sprayed on the surface of the evaporator to melt the ice. Thus, at the end of the defrosting cycle the surface of the evaporator is near the temperature of the inlet water and the compressors are turned on to bring the temperature of the evaporator surface back to its design conditions. This procedure is inefficient and involves the use of large quantities of water to defrost the cooling coils.

Liquid desiccants are natural or synthetic substances capable of absorbing moisture from the air due to the difference of vapor pressure between the surrounding air and the desiccant surface. They are hygroscopic at low temperatures (absorb water) and hydrophobic at higher temperatures (reject water). Liquid desiccants have the capability of providing localized dehumidification since the regeneration stage can be located far away from the dehumidification zone. Concentrated solutions of liquid desiccants are often sprayed into air streams or applied as falling films on the surface of dehumidifiers to absorb water vapor from the incoming air. The diluted liquid desiccant solution is then pumped to a regeneration stage where heat is applied to reject the moisture content of the solution increas-

ing its desiccant concentration. The concentrated desiccant solution is pumped back to the absorber to repeat the cycle.

In the air conditioning systems field, the use of liquid desiccant systems has become more popular in the past decades due to the need for reduction in the consumption of energy and water [18, 19]. The capability of these systems in handling latent heat in the space that will be conditioned by a dehumidifying process also allows control of the humidity without the overcool/reheat scheme as is done in a regular ventilating and air conditioning system (VAC) [31].

Most liquid desiccant applications target cooling and dehumidification at ambient conditions [32–36]. However, a few studies focus on the application of liquid desiccants to refrigerated spaces. A literature review of the theoretical and physical models of a refrigerated warehouse, as well as, the comparisons between a traditional vapor-compression cycle and a liquid desiccant refrigeration cycle are found in Daou et al. [34]. Elsayed et al. [37] analyzed the performance of an air cycle refrigerator combined with a desiccant rotor for an air conditioning application. More recently, the same authors numerically analyzed the performance of an air cycle refrigerator integrated with a desiccant system for cooling and dehumidifying a warehouse [38]. They found that the coefficient of performance can increase more than one hundred percent with respect to a conventional system.

The purpose of this chapter is to analyze the experimental results obtained for the performance of a small-scale prototype liquid desiccant absorber installed at a commercial refrigerated warehouse.

2.2 Description of the installation

The operation of a liquid desiccant absorber inside a commercial refrigerated warehouse was analized by means of installing a small-scale prototype liquid desiccant system at a representative cold storage site in California's San Joaquin valley. The purpose was to measure the performance of an adiabatic absorber under realistic operating conditions inside a commercial cold storage facility. The inlet air conditions to the absorber and facility evaporator were similar so that the air properties downstream of the absorber, T_{Abs}^{out}, were compared with the temperature measured at the surface of the evaporator. If the dew point temperature of the outlet air from the absorber was below or near the surface temperature of the evaporator then a potential exists to eliminate or at least delay the formation of ice at the surface of the cooling coil. Temperature and relative humidity sensors were installed to measure inlet and outlet air conditions at the absorber, and temperature sensors were used to measure the surface temperature of the coil.

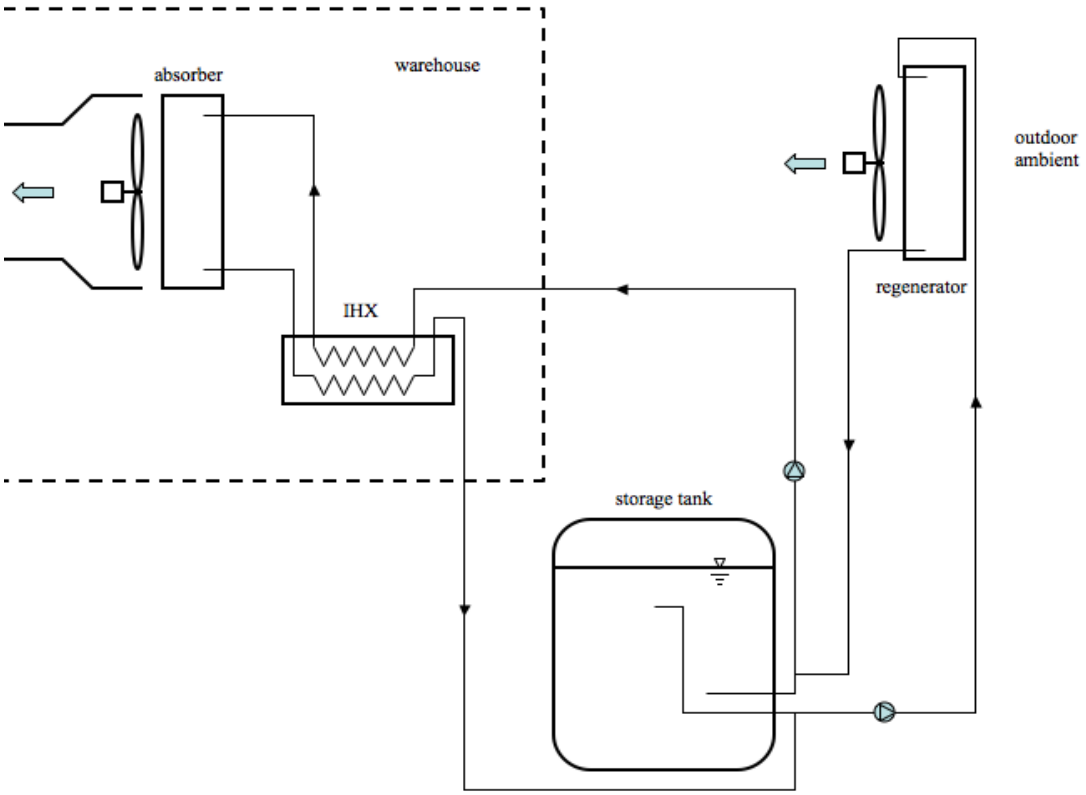

Figure 2.1: Small-scale liquid desiccant prototype system.

Calcium chloride solution was used as the working fluid for the liquid desiccant system which consisted of an absorber, internal heat exchanger (IHX), storage tank, two regenerators, and control unit. The operation of the system is depicted on Fig. 2.1 and consisted of the following processes: concentrated calcium chloride solution was pumped from a storage tank of approximately 1.14 m^3 of capacity to the IHX. The desiccant was cooled at the IHX by using the flow of diluted desiccant coming out of the absorber. The outlet of the high-pressure side of the IHX was fed into the inlet of the absorber. The concentrated liquid desiccant solution falling as a film down the walls of the dehumidifier absorbed moisture from the cold humid air inside the cold storage. The diluted liquid desiccant solution passed through the low-pressure side of the IHX and then was sent to the regenerators that were located outside of the cold storage. After being regenerated, the concentrated liquid desiccant solution was sent to the storage tank to repeat the cycle.

At the absorber the liquid desiccant film interacted with the air flowing in cross-flow configuration. The air speed could be adjusted with a simple speed

Table 2.1: Design operating conditions inside refrigerated warehouse.

Design parameter	Range	Units
Indoor temperature	0 to 1	°C
Relative humidity	85 to 100	%
Coil temperature	-6.7 to -3.9	°C
Evaporator air-flow rate	7 to 40	$m^3\ s^{-1}$
Ammonia flow rate	0.605	$kg\ s^{-1}$
Cooling capacity	351	kW
Condensation temperature	29 to 32	°C

controller connected to the fan. Heat and mass were exchanged at the interface between the air and the liquid desiccant film. Since the liquid desiccant solution is mildly corrosive, the absorber, regenerators, and IHX were built by AIL Research using non metallic materials.

It is noted that since the ambient conditions at California's San Joaquin Valley are hot and dry during several months of the year, only ambient air was used to regenerate the liquid desiccant so that no external source of heat was used. Two regenerating cores with similar design as the absorber were used with the purpose of having a large regeneration surface. During the night when the ambient relative humidity increased, the control unit shut down the flow to the regenerators and only the concentrated liquid desiccant solution from the storage tank was used for the absorption process at the dehumidifier.

The project lasted for two and a half years. The liquid desiccant system effectively operated for twelve months that included the end of season 2007, season 2008, and the start of season 2009. Data was collected at a sampling rate of twenty six channels per minute. The data have been carefully examined and it has been concluded that the operation of the system can be summarized by analyzing representative information for summer and fall conditions.

2.3 Operation conditions inside the refrigerated warehouse

The air inside the cold storage is required to have a high relative humidity to avoid lowering the quality of the produce. The design operating conditions inside the refrigerated warehouse, as well as, the ambient conditions are listed in Tables 2.1 and 2.2, respectively. In particular, pre-cooling rooms have bins with produce that are taken in and out of the cold storage facility allowing hot ambient air into the room. This increases the load on the evaporators and augments the amount

Table 2.2: Historical ambient conditions in San Joaquin Valley, California.

	Range	Units
Summer temperature	16 - 36	°C
Fall temperature	6 - 20	°C
Summer RH	23 - 65	%
Fall RH	30 - 80	%

of moisture that condensates on the surface of the cooling coils resulting in the formation of ice. The defrosting cycle consists on spraying water on the evaporator until the ice has melted. The spraying of water also creates a mist inside the cold storage that helps keeping a high moisture level (above 75%) inside the room. A typical defrosting cycle is shown in Fig. 2.2 where the surface temperature of the evaporator is shown together with the temperature and flow rate of the water sprayed to melt the ice. The air pressure drop measured across the evaporator is also displayed. The cycle stars by turning the fans off as indicated by the reduction in air pressure drop from approximately 53 Pa to zero. At 5:16 pm the flow rate of water is turned on. Water at 22 °C was sprayed on the surface of the evaporators for 17 minutes, approximately. It is observed that the temperature of the cooling coil increases during this process and remains at around 8°C even after the flow of water has ceased. The defrosting cycle ends when the fans and refrigerant flow are turned back on and the surface temperature of the evaporator goes down to its design value. The cycle is repeated one to three times a day depending on the time of the year and type of produce being cooled. It can be observed that the air pressure drop across the evaporator has a lower value after the defrosting cycle has concluded indicating the removal of ice. During the peak of the season, the air pressure drop can reach values near 800 Pa therefore needing a significant amount of water to melt the ice. Integration of the flow rate with respect to time results in 2.3 m^3 of water being used for each defrosting cycle.

2.3.1 Operating of adiabatic absorber and evaporator inside the cold storage

Liquid desiccant systems have received significant attention recently as a way to reduce latent loads on air conditioning systems [20]. Most systems have been installed to dehumidify ambient air before it reaches the evaporator. As the air humidity is absorbed at the dehumidifier, the temperature of the liquid desiccant increases due to the addition of heat from the enthalpy of condensation of water vapor. Thus, the design of a liquid-desiccant absorber includes the flow of a cooling fluid inside its walls that removes heat from the liquid desiccant.

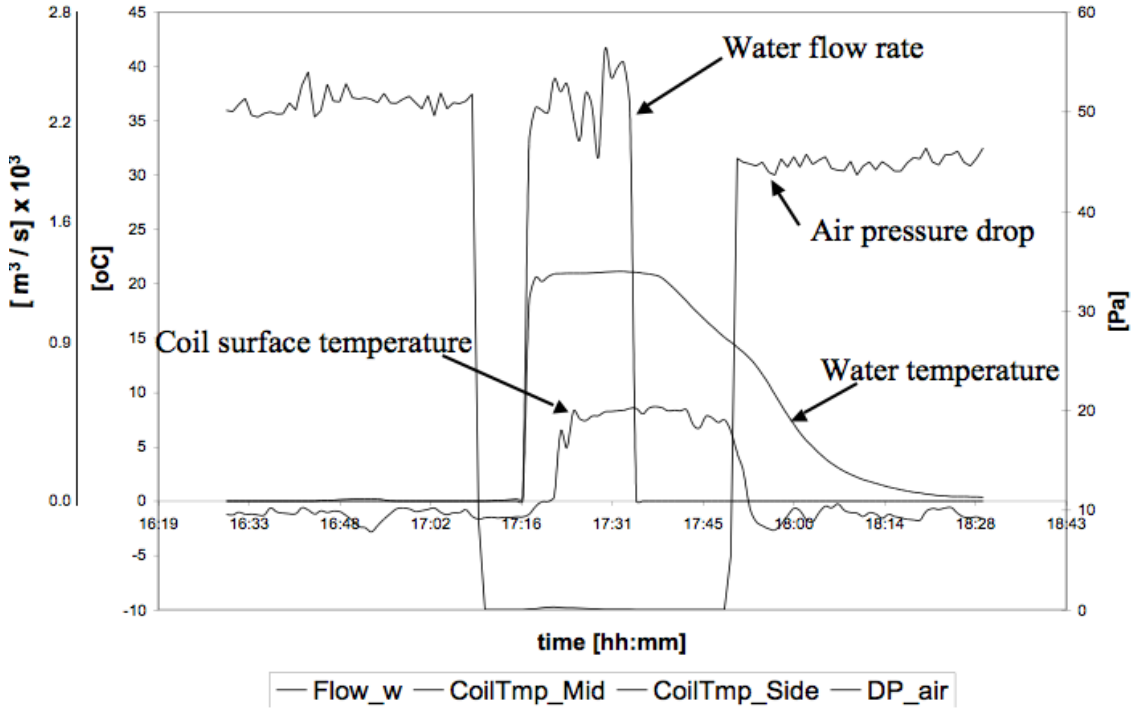

Figure 2.2: Defrosting cycle sequence of steps.

A novel application of liquid desiccant systems corresponds to the localized removal of moisture from the air inside refrigerated warehouses for the food industry which tend to operate with relatively high levels of indoor air humidity. This high indoor air humidity translates into ice formation at the evaporator. The localized removal of moisture by the liquid-desiccant absorber upstream of the evaporator can substantially reduce the formation of ice. Due to the low temperature of the air inside these rooms, no cooling fluid is necessary for the removal of heat from the liquid desiccant. Thus, the absorber can be designed as an adiabatic core in cross-flow configuration, as seen in Fig. 2.3. In this work, non-metallic pleated plates were used to form zig-zag-shaped channels with liquid desiccant entering at the top of the absorber and flowing down the walls as a film that was in contact with humid air in cross-flow configuration. Table 2.3 indicates the operating conditions and geometric parameters of the absorber. Inlet and outlet air temperature and relative humidity at the absorber were measured using Vaisala sensors model HMT330 with a range of -40 to 60°C with accuracy of ± 0.2°C and 0 to 100% relative humidity with accuracy of ± 1%. Based on these measurements, the upstream and downstream air dew point temperatures at the absorber were

calculated. The core had a 53% humidity effectiveness as defined in [20]. Space and operational constraints at the cold storage prevented the air downstream of the absorber to be sent to the inlet of the evaporator. However, as a means of comparison, the surface temperature of the cooling coil, subject to similar air inlet conditions as the absorber, was measured using a Veris RTD model AA10F1 sensor with a range of -50 to 50°C with an accuracy of ± 0.3°C. Similar RTDs were used to measure the temperature of the water used for the defrosting cycle.

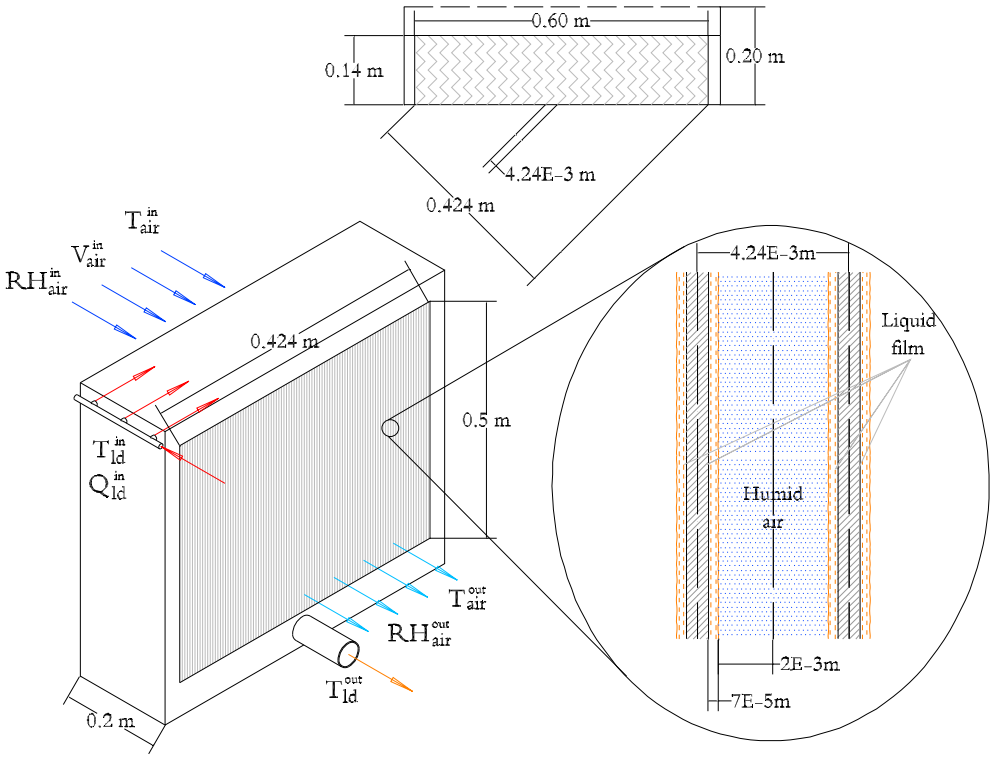

Figure 2.3: Schematic of adiabatic absorber.

Operating conditions at the cold storage vary significantly throughout the year. For instance in November, the ambient temperature is low so the load on the evaporator due to infiltration of outdoor air is less significant than during the summer. Therefore, not all the fans inside the facility are used and the air flow across the evaporator is low. The air-flow rate across the evaporator varies from 7 m^3/s during late-fall conditions to 40 m^3/s during summer. Figure 2.4 (a) shows the performance of the absorber under these operating conditions. Two defrosting cycles are depicted where the air inlet temperature, T_{Air}^{in}, to the absorber is shown together with the inlet temperature of the water used for the defrosting

Table 2.3: Absorber operating conditions and geometric specifications.

	Parameter	Range	Units
Liquid desiccant (Calcium chloride)	Concentration	33 - 36	% (by weight)
	Inlet temperature to IHX	18 - 25	°C
	Volumetric flow rate	1.33×10^{-5}	m^{-3} s^{-1}
Air	Inlet RH	75 - 100	%
	Inlet temperature	0 - 15	°C
	Face velocity	1.6 - 1.8	m s^{-1}
Geometry	Face area	0.3	m^2
	Contact surface area	20	m^2
	Plate spacing	4.2×10^{-3}	m
	Core depth	0.20	m

cycle, T^{in}_{Water}, and the cooling coil surface temperature, T_{Coil}. The calculated dew point temperature upstream, $T^{in}_{DewPoint}$, and downstream, $T^{out}_{DewPoint}$, of the absorber are also shown. It is seen that the inlet dew point temperature is, in general, above the cooling coil surface temperature leading to the formation of ice on the evaporator. The absorber removes moisture from the inlet air and lowers the dew point temperature to a value comparable with the evaporator surface temperature. Therefore, even if the formation of ice is not completely eliminated, this technology has the potential to delay frost formation significantly. Figure 2.4(b) shows that the relative humidity inside the cold storage remains near 80% with spikes occurring during the defrosting cycles. The change in air pressure drop before and after the defrosting cycle, shown in Fig. 2.4(c), is not significant indicating a low rate of ice formation.

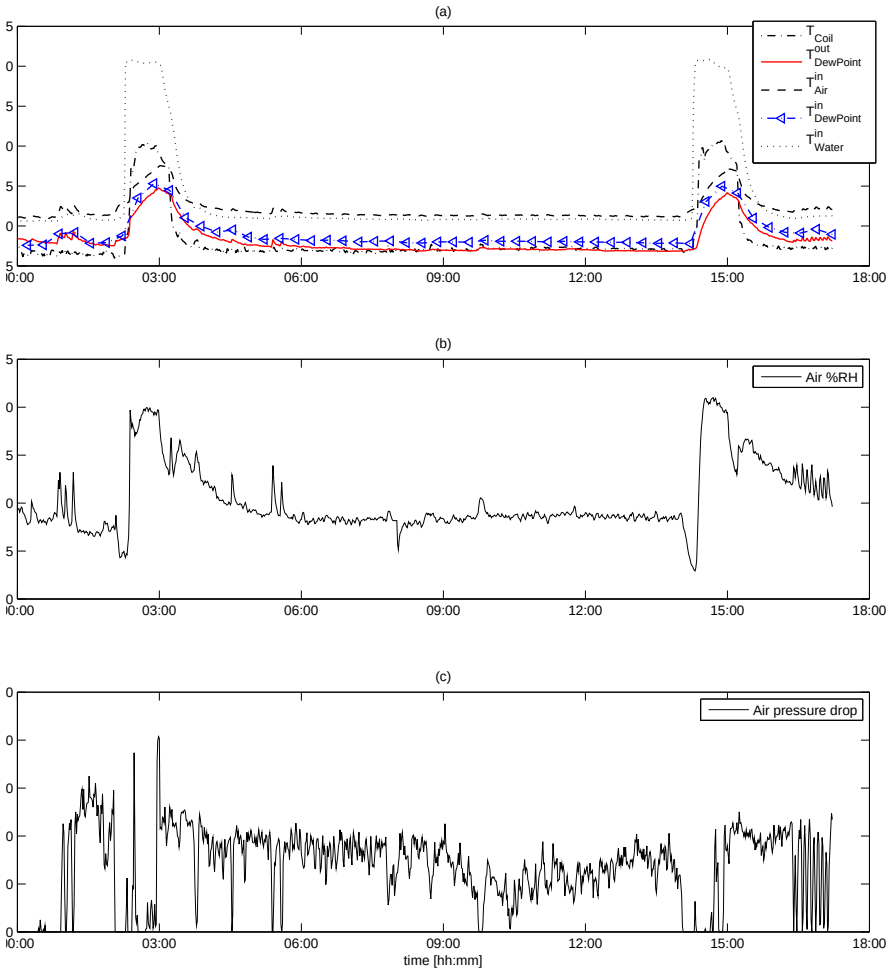

Figure 2.4: Operating conditions of the refrigerated warehouse under low air speed across the evaporator. The dewpoint temperature of the air upstream and downstream of the absorber is also shown.

A very different pattern is obtained by analyzing data from summer. Figures 2.5(a) to 2.5(c) display the same variables shown in Figs. 2.4(a-c) but for a much higher air flow rate across the evaporator and for ambient conditions that vary between 39°C with 15% relative humidity during the day and 18°C with 73%RH during the night. Four defrosting cycles are observed with a much more variable overall behavior. Ice formation can be inferred from the increase in air pressure drop across the cooling coil that reached a maximum of 800 Pa, as observed in Fig. 2.5(c). It is seen that once a significant amount of ice has been formed, the evaporator does not condition the air effectively and the temperature inside the room

Table 2.4: Representative summer and fall operation of prototype absorber.

	Summer	Fall	Units
T_{ld}^{in}	4.5	4.4	°C
Concentration (by weight)	35	35	%
Volumetric flow rate (liq. des.)	2.15×10^{-5}	2.1×10^{-5}	$m^3\ s^{-1}$
T_{air}^{in}	1.9	2	°C
Inlet air RH	91	80	%
T_{air}^{out}	2.95	3.34	°C
Outlet air RH	62	63	%
T_{ld}^{out}	2.8	3.24	°C

Table 2.5: Representative summer and fall operation of prototype regenerator.

	Summer	Fall	Units
T_{ld}^{in}	25	18	°C
Concentration (by weight)	33	32	%
Volumetric flow rate (liq. des.)	2.15×10^{-5}	2.1×10^{-5}	$m^3\ s^{-1}$
T_{air}^{in}	30	8	°C
Inlet air RH	30	50	%
T_{air}^{out}	26	17	°C
Outlet air RH	50	53	%
T_{ld}^{out}	25	17.9	°C

starts to rise. Therefore the calculated inlet and outlet dew point temperatures become higher than the temperature measured at the surface of the coil. The absorber produces a downstream dew point temperature that is approximately 3.5°C below the inlet air dew point temperature. This implies that under these conditions a layer of ice separates the temperature sensor attached to the coil from the air passing across the evaporator. It is noted that the absorber maintains the downstream air dew point temperature close to the evaporator surface temperature for air pressure drops below 600 Pa, as seen in Fig. 2.5(a). Figure 2.5(b) shows that the relative humidity of the inlet air varies from 70 to 100% inside the room. A schematic of the dehumidification process, A, across the liquid desiccant absorber is presented on a psychrometric chart in Fig. 2.6. The process across an evaporator receiving the outlet air from the absorber is labeled with a letter "B". The regeneration process is shown with a letter "C". Typical summer and fall conditions inside the cold storage are shown. Tables 2.4 and 2.5 list the parameters of the prototype absorber and regenerator, respectively. Summer and fall operating conditions are included.

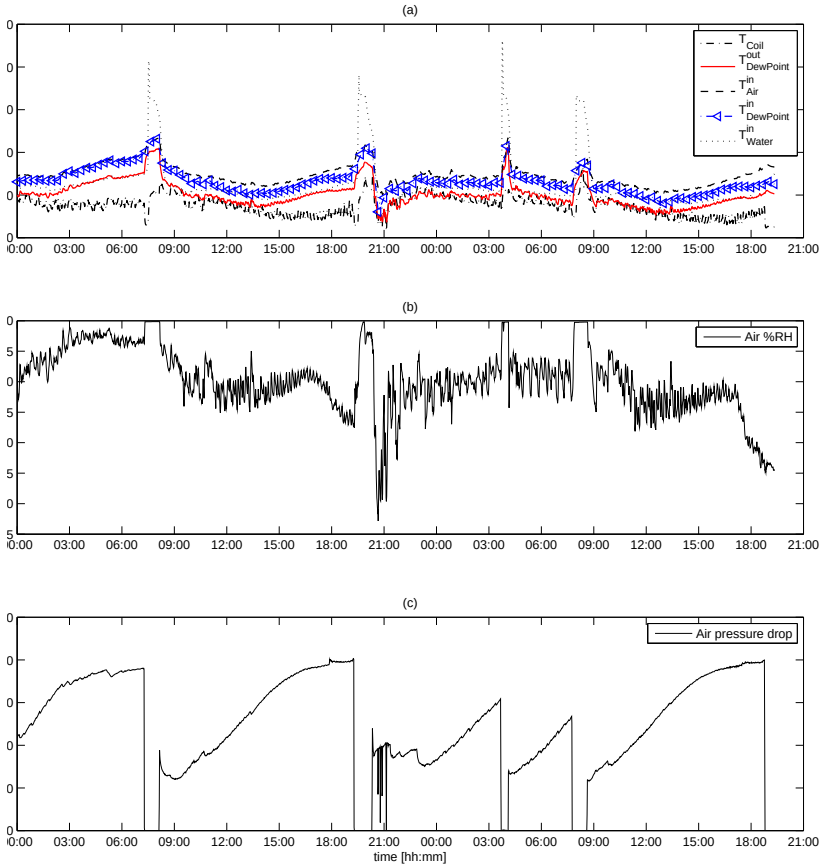

Figure 2.5: Operating conditions of the refrigerated warehouse under high air speed across the evaporator. The dewpoint temperature of the air upstream and downstream of the absorber is also shown.

2.3.2 Control logic for the liquid desiccant system

The operation of the prototype liquid desiccant system required a controller to choose the optimal operating parameters based on measurements of the status of the system. A SBC65EC single-board programmable computer from Modtronix Engineering was utilized for controlling purposes. Inputs included ambient relative humidity and gage pressure from the liquid desiccant level inside the storage tank. The value of the pressure was translated to the level of liquid inside the tank. The level of liquid was allowed to vary between 0.96 m and 1.16 m. Liquid levels consistently outside of this range would indicate either a leak or a malfunctioning of the regenerators and the system would be shut down. For liquid levels within

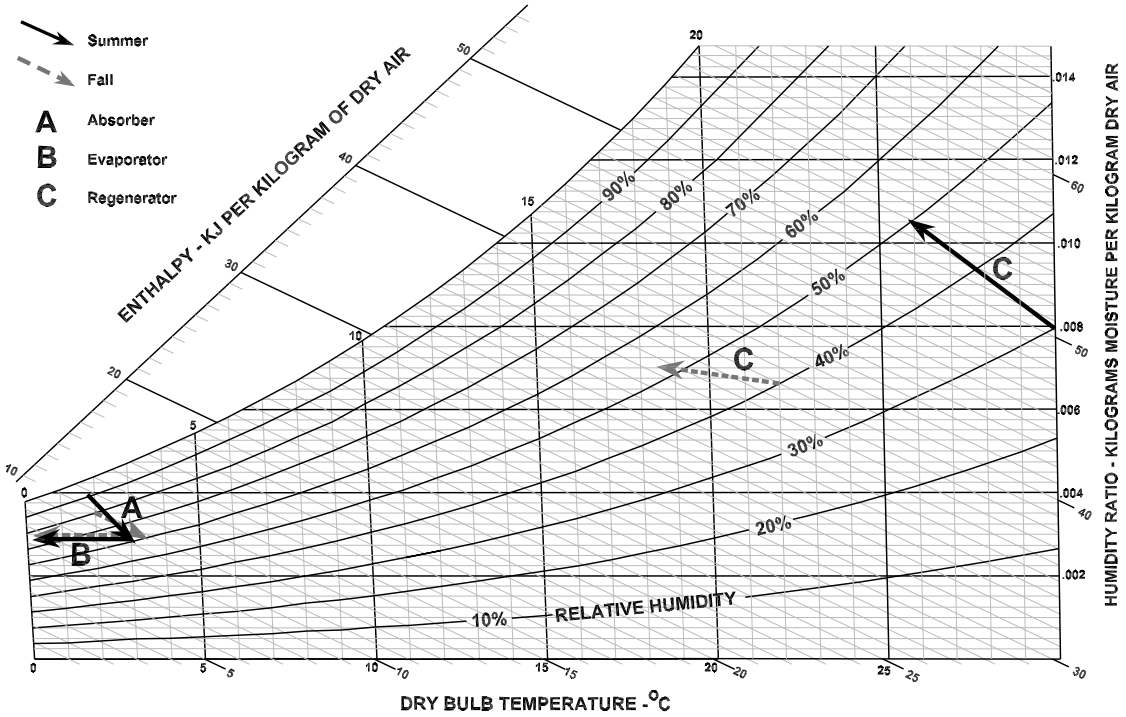

Figure 2.6: Dehumidification process across the absorber. Calcium chloride enters the absorber with a concentration of 35%, approximately.

the operating range, the controller would turn off the liquid desiccant flow to the regenerators when the liquid level reached the lower limit of the band. On the other hand, if the tank level reached the upper limit then the flow of liquid desiccant to the absorber would be turned off. The normal operation of the absorber and regenerators was not resumed until the level in the tank had reached the middle of the operating range. Since the regeneration of the liquid desiccant was done using ambient air without any source of external heat, the controller turned the flow to the regenerators on when the ambient relative humidity was below 50%. For higher values of ambient relative humidity, the regenerators were kept off. This limit was set considering the vapor pressure of calcium chloride at the inlet temperature and concentration of the liquid desiccant to the regenerators.

It is noted that high-humidity weather conditions would not regenerate the liquid desiccant to the required levels of concentration. Therefore, external heat sources in the form of propane or natural gas heaters, double-effect boilers, or solar collectors would need to be implemented.

2.3.3 Rate of water absorption

Space and operational constraints at the industrial facility prevent an accurate measurement of the air flow rate across the absorber. Thus, to measure the rate of water absorption at the dehumidifier the level of liquid desiccant at the storage tank was measured. The change in the level of the tank was obtained using a Setra pressure transducer model 264 with a range of ± 6.23 kPa and an accuracy of ± 1% on the full scale. The regenerators use ambient air to reject water from the liquid desiccant. However, during the night, the ambient air can reach high levels of relative humidity that impede the regeneration process. The control unit turned the regenerators on when the ambient relative humidity was below 50%. Figure 2.7 shows the number of hours per day that the regenerators could operate during the season. The figure shows that during the summer, the regenerators can operate close to 20 hours in a day. During fall ambient conditions, the number of hours of regeneration is significantly reduced. When absorber and regenerators are operating, the level of liquid desiccant at the tank varies depending on the rate of water absorbed at the dehumidifier and rejected at the regenerator. Thus, the absolute rate of moisture absorption at the absorber was measured at a time when the regenerators were not running. Figure 2.8 shows with a dashed line the status of the regenerators, i.e. on or off, together with the liquid desiccant level at the storage tank. It is observed that as soon as the regenerators are turned off the level of the liquid desiccant shows a sharp increase due to the fact that the suction of the pump for the regenerators is no longer present. Then the level of the tank increases almost linearly with time. Based on the slope of the curve, it is estimated that the dehumidifier can absorb 0.008 kg/min of water, approximately for a liquid desiccant concentration at the inlet of the absorber of 35% with a flow rate of 0.8 liters per minute. At indoor relative humidities near 100% and colder liquid desiccant inlet temperatures the rate of water absorption has been observed to reach 0.017 kg/min. Therefore, the small-scale absorber processes an air-flow rate of 0.2381 m^3/s and removes an average of 0.013 kg/min of water, approximately. Assuming a linear scale for a cold storage processing 40 m^3/s, the absorber would remove 3182 kg of water per day.

2.3.4 Internal heat exchanger operation

The absorption properties of the liquid desiccant improve as its temperature is lowered. The vapor pressure of the liquid desiccant tends to zero at low temperatures which provides a benefit in terms of increased water absorption rate and reduction in the potential for droplet carry over. Since the regeneration process is performed with ambient air, the inlet temperature of the liquid desiccant to

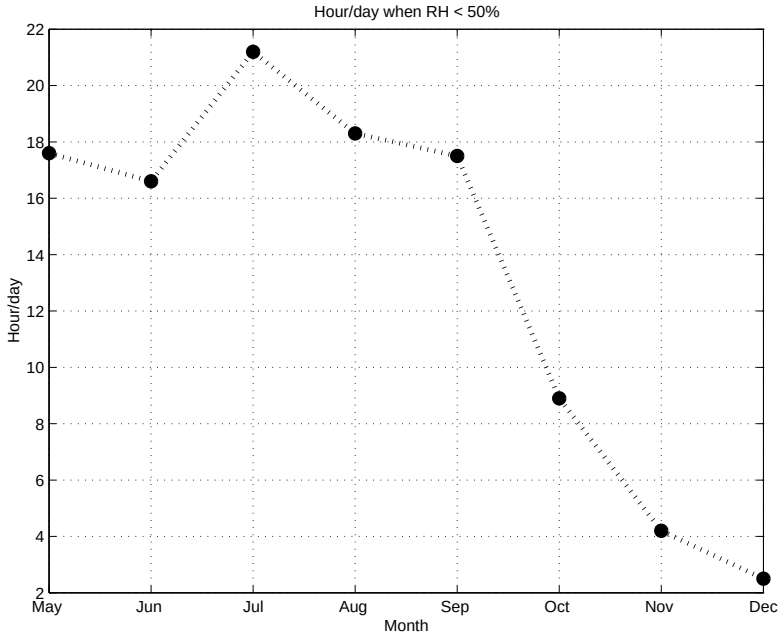

Figure 2.7: Hours per day suitable for liquid-desiccant regeneration with ambient air at California's Central Valley. Regenerators are turned on when ambient RH < 50 %.

the IHX remains between 18 to 25°C for typical summer operating conditions, as seen in Fig.2.9. Therefore, the temperature of the concentrated liquid desiccant, T^{in}_{IHX}, was lowered using the outlet stream of diluted liquid desiccant exiting the absorber at T^{out}_{Abs}. Figure 2.9 shows that for ambient ranging between 20 to 38°C, the conditions inside the cold storage generate an inlet air temperature to the absorber below 5°C except during the defrosting cycles. Under these operating conditions, the IHX lowers the temperature of the concentrated liquid desiccant solution by 16°C, approximately. Even though the liquid desiccant absorbs energy from the condensation of water vapor from the humid air, the low temperature conditions inside the cold storage imply that the outlet liquid desiccant temperature from the absorber, T^{out}_{Abs}, is below T^{in}_{Abs} and therefore this stream can be used to lower T^{in}_{IHX}. An energy balance performed at the core shows that

$$Q = \dot{m}_{ld} Cp_{ld} \Delta T_{ld} = \dot{m}_a (Cp_a \Delta T_a + h_{gf} \Delta\omega). \tag{2.1}$$

In general, the results show that ΔT_{ld} and $\Delta\omega$ are negative and ΔT_a is positive. The experimental uncertainty in the energy balance between the liquid desiccant and the humid-air sides under steady conditions is computed. The liquid desiccant

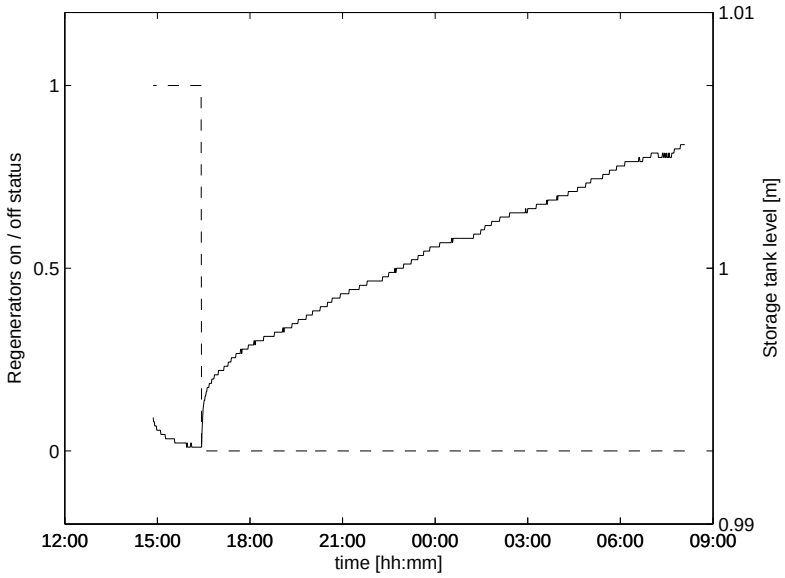

Figure 2.8: Moisture absorption rate.

uncertainty is larger mainly due to the ± 0.3 °C of accuracy from the RTDs. This situation changes during transients where the thermal inertia of the absorber walls affects the energy balance such as during the start and end of defrosting cycles.

2.4 Potential water and energy savings

As seen in Fig.2.2, each defrosting cycle uses 2.3 m^3 of water in this facility. The amount of water used is higher in cold storage rooms with larger evaporator coils. During the season of operation of a cold storage, that lasts between late May to early December, the number of defrosting cycles per day varies between 1 to 3. Taking an assumption of two defrosting cycles a day for six months of operation results in 828 m^3 of water used for one pre-cooling room. It is noted that according to California Energy Commission data, there are 246 refrigerated warehouses in the state many of which have more than one cold storage room in their facilities. Thus, the potential of reduction in water consumption is significant. However, it was mentioned that the conditions inside the refrigerated warehouse require high levels of air humidity so that if the defrosting cycles are significantly reduced then a water spray system would need to be added to the facility to conserve the quality of the produce.

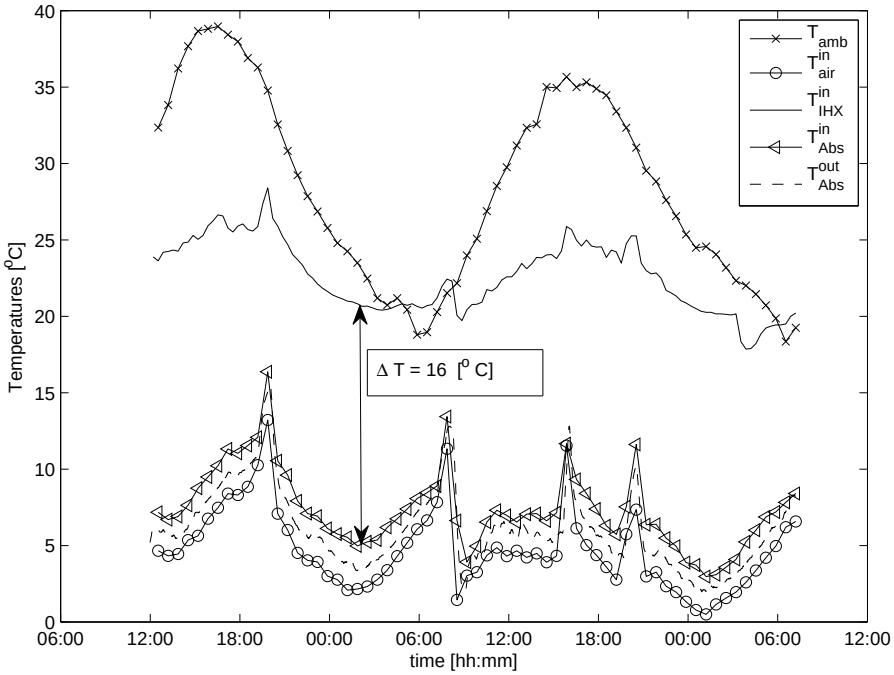

Figure 2.9: Internal heat exchanger performance.

The energy savings for a scaled-up system can be mainly associated with two effects related to eliminating or significantly delaying the formation of ice. After the defrosting cycle, the cooling coil surface temperature is higher than the design operating conditions of the evaporator so compressor power is required to lower its temperature after each defrosting cycle. Also, during periods where there is significant ice formation on the surface of the coil, the temperature inside the cold storage starts to rise, as seen in Fig. 2.5. The compressors tend to run more frequently as a reaction to the increasing value of the indoor temperature. The evaporating temperature decreases raising the power used by the compressor. Figure 2.10 shows the coil temperature, T_{Coil}, the air inlet temperature, T_{Air}^{in}, and measurement of the temperature at the inlet manifold of the evaporator, $T_{Manifold}$. This temperature is not subject to the flow of air so it is closer to the refrigerant temperature at that location. The oscillations are due to the opening and closing of the valve that controls the refrigerant flow to the evaporator.

The commercial cold storage room has a total air-flow rate through the evaporator of 40 m^3/s with inlet air conditions of 1 °C and 85% relative humidity, and a

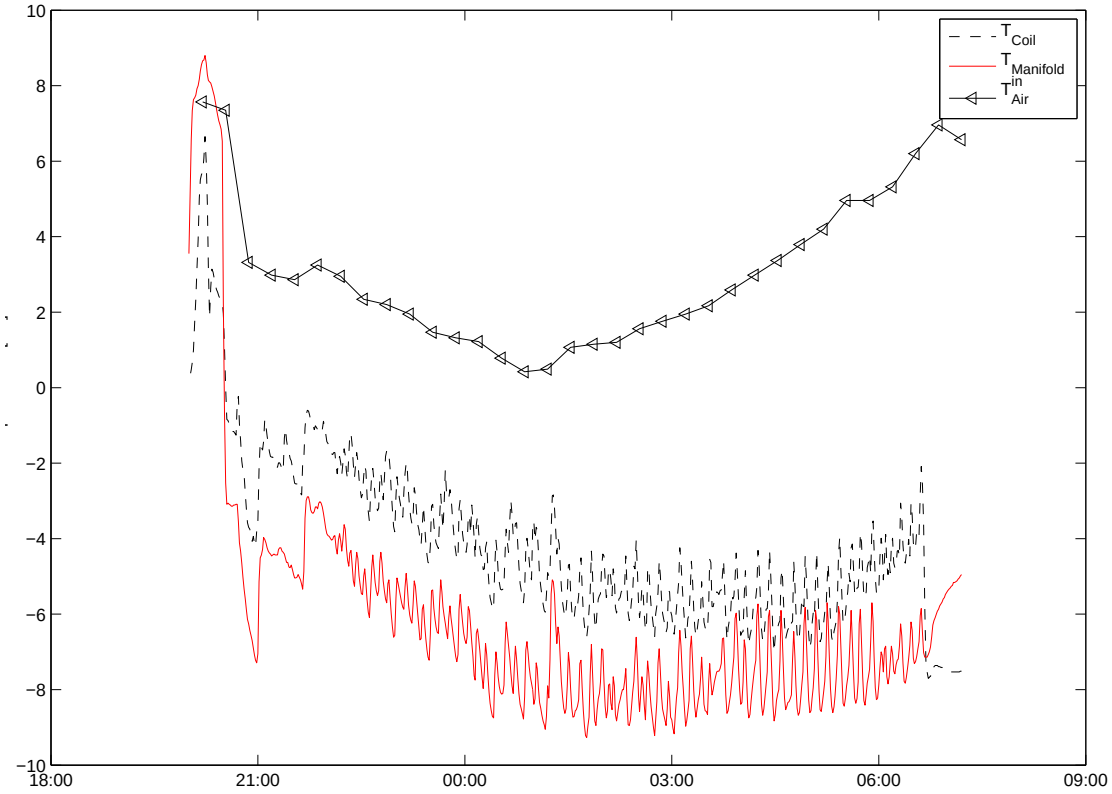

Figure 2.10: Inlet manifold, cooling coil, and inlet air temperatures inside the cold storage.

design evaporating temperature of -4 °C. It is rated at 351kW of cooling capacity operating with a COP of 2.2, approximately. Therefore, it utilizes 160kW of compressor power and 21.9kW of fan power under no-frost conditions. An absorber operating for 24 hours a day can absorb 3182 kg of water. The extra air pressure drop due to the absorber is compensated by the lower pressure drop across the frost-free cooling coils. Ambient air would be used to regenerate the liquid desiccant. Considering ambient conditions of 35°C and 20 %RH, the regenerators are assumed to work for six hours per day. In order to remove the amount of water required, a 0.15m-deep regenerator with a face velocity of 2.1 m/s would require an air-flow rate of 72 m^3/s. The fan power required to move the air would be 10.8 kW where the pumping power has been neglected. Figure 2.10 shows that under frost conditions, the evaporating temperature of the refrigerant decreases and oscillates between -8°C and -9°C. Considering a constant condensing pressure of 1238 kPa and an isentropic compression efficiency of 75%, the reduction in

evaporating temperature increases the compressor power by 16%. This increase in compressor power does not translate into a higher cooling capacity since the layer of ice acts as an insulator and the temperature inside the cold storage begins to rise, as observed in Fig. 2.10. The energy for lowering the coil temperature after each defrosting cycle based on the mass of the evaporator is estimated at 4.6 kWh. Thus, the net energy savings by not having frost formation on the surface evaporator are estimated at 16.3%. A more conservative 15% reduction in energy consumption and a rate of 13.54 cents/kWh imply that the cost savings during the year reach 11% of the installation cost for the liquid desiccant system. Therefore, retrofitting of an existing cold storage would probably be not economically attractive, although more analysis is needed under real-time power pricing or at locations with higher power-generation costs. However, the application of this system to a new facility would significantly reduce the size of the evaporator by being able to reduce its fin spacing. The lower cost of the evaporator would offset the cost of the liquid desiccant system.

2.5 Conclusions

The performance of a small-scale liquid desiccant absorber subject to realistic operating conditions inside a commercial refrigerated warehouse has been studied. It is observed that the dew point temperature of the air downstream of the absorber was near or even below the measured surface temperature of the evaporator. This implies that a significant reduction in ice formation could be achieved with such a system. However, during operating conditions where a thick layer of ice was already formed on the cooling coil, the temperature of the evaporator surface was below the dew point temperature of the dehumidified air. The performance of an internal heat exchanger to lower the liquid desiccant temperature has also been examined and it is noted that the regeneration process can be achieved only with ambient air. Analysis of the system indicates that a significant reduction on water consumption can be accomplished but the energy savings suggest that the system would be feasible for new installations instead of retro fitted ones.

Acknowledgments

This work has been supported by the California Energy Commission and the California Institute for Energy and Environment contract number MR-07-04. The authors would like to thank Aslan Cold Storage, LLC and Del Monte Foods for

allowing access to their facilities to obtain measurements of realistic refrigerated warehouse conditions.

Chapter 3

Analysis of heat and mass transfer of an adiabatic cross-flow liquid desiccant absorber operating at low temperatures

With the rising costs of electricity due to increasing demand of electric power, liquid desiccant systems have received significant attention as a way to reduce latent loads on air conditioning systems. In particular, the performance of liquid desiccant systems in humid climates has shown significant reductions in energy consumption. In general, these liquid desiccant systems are composed by an absorber or dehumidifier and a regenerator that utilizes a heat source to reject the water from the diluted liquid desiccant. As the humidity of the air is absorbed at the dehumidifier, the temperature of the liquid desiccant increases due to the addition of heat from the enthalpy of condensation of the water vapor. Thus, many designs of liquid desiccant absorbers include the flow of a cooling fluid that removes heat from the liquid desiccant. A novel application of liquid desiccant systems corresponds to the localized removal of moisture from the air inside low temperature rooms that contain relatively high levels of humidity such as refrigerated warehouses for the food industry. The purpose is to reduce the formation of ice at the surface of the evaporator. Due to the low temperature of the air inside these rooms, no cooling fluid is necessary for the removal of heat from the liquid desiccant. Thus, the designs of the absorbers differ from the designs used for ambient air temperatures. In this chapter, a mathematical model of the heat and mass transfer for an adiabatic parallel-plate absorber for which a thin

film of liquid desiccant flows down its walls and dehumidifies the air in cross-flow configuration is developed.

3.1 Introduction

The projection of the world's market energy consumption published by the Energy Information Administration (EIA), predicts an increase in the demand of energy of approximately 50 percent from 2005 to 2030, equivalent to an increase from 462 quadrillion British thermal units (Btu) (487.4 quadrillion kJ) to 695 quadrillion Btu (733.3 quadrillion kJ) [16]. In this context, the demand of energy consumption in countries that are members of the Organization for Economic Co-operation and Development (OECD) is projected to increase by 19 percent during this period, and by 85 percent in the non-OECD countries. Therefore, the efficient use of electric power together with innovative technologies are fundamental tools for reaching reduced levels of energy consumption. One example is refrigerated warehouses where the energy consumption is clearly intensive and where a large potential for additional energy saving exists [17, 39].
Energy savings of up to 80 % when the latent load constitutes 90 % of the total cooling load, have been suggested for hybrid desiccant cooling systems comprised by the traditional vapor compression air conditioning system coupled with a liquid desiccant dehumidifier regenerated by solar energy [40].
Comparisons between a traditional vapor- compression cycle and a liquid desiccant refrigeration cycle have been performed in [18], where an improved design showed 18 to 23 percent higher coefficient of performance depending on the behavior of (a) the dehumidifier or regenerator, (b) the desiccant used for the specific ambient conditions [21, 41], and (c) the effectiveness of the heat exchanger [34].
Desiccants are natural or synthetic substances capable of absorbing or desorbing water vapor due to the difference of water vapor pressure between the surrounding air and the desiccant surface. They are hygroscopic at low temperatures (absorb water), but hydrophobic at higher temperatures (reject water). Also, they are encountered in both liquid and solid states. Each liquid and solid desiccant system has its own advantages and shortcomings. In addition to having lower regeneration temperature and flexibility in utilization, liquid desiccants have lower pressure drop on the air side. Commonly used desiccant materials and substances include: lithium chloride, calcium chloride, triethylene glycol, silica gels, aluminum silicates (zeolites or molecular sieves), aluminum oxides, and lithium bromide and lithium chloride in solution with water [34].
Liquid desiccants are often sprayed into air streams or wetted onto contact surfaces to absorb water vapor from the incoming air (absorption process). The water

vapor sorption must be driven out of the desiccant material (regeneration process) so that it can be concentrated enough to absorb water vapor in the next cycle [34, 41–43].
Jain and Bansal [19] evaluated packed-bed dehumidifiers for three commonly used desiccant materials: triethylene glycol (also presented in [44]), lithium chloride, and calcium chloride. The analysis shows wide variations in effectiveness values ranging from 10 percent to 50 percent or more, with higher deviations occurring for lower ratios of liquid to gas flow rates. Kinsara, et. al [45] conducted a simulation study on a desiccant cooling system using an aqueous solution of calcium chloride ($CaCl_2$) as the liquid desiccant. The impact of certain parameters on the system's performance was studied. Those parameters included the desiccant solution inlet temperature, the space sensible heat ratio (SHR), the heat exchanger effectiveness, and the ratio of liquid desiccant flow rate to the air flow rate ($\dot{m}_l/\dot{m}_a$).
In the air conditioning systems field, the use of liquid desiccant systems has become more popular in the past decades [32–36] due to the necessity of reduction in the consumption of energy and water [18, 19]. The capability of these systems of handling latent heat in the space that will be conditioned by a dehumidifying process, also allows control of the humidity without the overcool/reheat scheme as is done in a regular Ventilating and Air Conditioning system (VAC) [31].
When a liquid desiccant is employed, the dehumidifier (absorber) is located upstream of the evaporators to perform a localized removal of the moisture content of air, with possible configurations including: finned−tube surface, coil−type absorber, spray towers, and packed towers [34, 46].
Most of the studies of the performance of these systems use empirical correlations for dehumidification effectiveness [19, 47]. However, performance also depends on the configuration of the flow between the humid air and the liquid desiccant, and can be classified into parallel flow, counter flow and cross flow [21, 48]. Also, the geometry of the ducts and walls where the liquid desiccant flows has an important effect. A variety of geometrical configurations have been studied in the past. For instance, a parallel plate liquid desiccant system is introduced in Mesquita [22] and a falling film tubular absorber with a falling film regenerator is presented by Jain [46]. Khan and Martinez [49] undertook the study of a mathematical model of a liquid desiccant absorber (dehumidifier) which showed increased performance in terms of the number of transfer units (NTU) of heat transfer between the air flow and the desiccant solution.
A few analytical models are presented in [21, 41] and numerical models in [18, 22, 50], where some works include experimental data [18, 21] from regular prismatic geometries [51] or for several geometric configurations [50, 52].

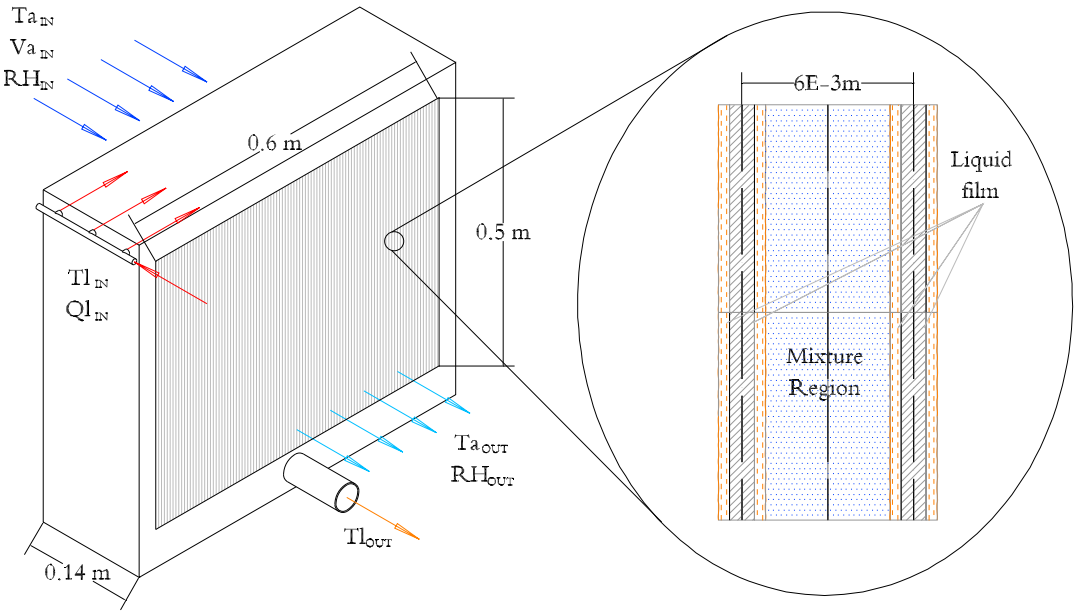

Figure 3.1: Schematic of the absorber device

In the present study, the behavior of an adiabatic absorber device is analyzed under operating conditions representative of a cold storage.

3.2 Description of the problem

High levels of humidity at a warehouse generate water condensation on the evaporator coil, thus forming ice at the coil surface. Consequently, a defrosting cycle needs to be performed once or twice a day. An alternative to this cycle is to use liquid desiccant systems to absorb the air moisture before it reaches the surface of the evaporator. Humidity levels inside the cold storage need to be kept high in order to preserve the quality of the produce inside the warehouse so the moisture removal needs to be performed in a localized way.
Moisture from the air is absorbed by the dehumidifier where liquid desiccant falls as a film down the walls. The film interacts with the air flow in a cross-flow configuration. Heat and mass are exchanged at the interface between the air and the liquid desiccant film. The dehumidified air goes towards the evaporator and the diluted desiccant is pumped to the regenerators. A schematic of the absorber device is presented in Fig. 3.1.

3.3 Mathematical formulation

A cross flow model between a falling liquid desiccant film and a horizontal air stream is studied in three dimensions, as shown in Fig. 3.2. The model is adapted from the works by Park [53, 54] and Ali [55].
Considering a laminar, fully developed flow for the liquid desiccant film and the air, the falling liquid falls down in the positive y_l direction and the air moves in the positive x direction. The rate of water vapor absorption is small and the solubility of air in the desiccant is negligible so the film thickness is considered constant. The velocity of the liquid desiccant in the z_l direction is zero. The flow is assumed to be smooth, implying no wavy motion exists. The physical properties are considered constant and thermodynamic equilibrium is assumed at the interface. The liquid desiccant velocity inlet condition is considered as a parabolic profile with the no−slip condition at the wall and zero gradient at the interface with the air. This is a first order approximation. Shear stress between liquid desiccant and humid air will be consider in chapters 5 and 6. For the air, a no−slip condition was assumed at the interface and a maximum velocity was considered at the symmetry plane. Air is considered as an ideal gas, body force was only considered for the liquid desiccant and no shear forces are exerted by the air on the film.

3.3.1 Liquid desiccant

We consider the velocity of the liquid desiccant in the z_l and x directions to be zero. From continuity, the variation of the velocity of the film in the y_l direction is also zero.

$$\frac{\partial v_l}{\partial y_l} = 0. \tag{3.1}$$

The equation of motion simplifies to

$$\mu_l \frac{\partial^2 v_l}{\partial z_l^2} + \rho_l g = 0, \tag{3.2}$$

with boundary conditions

$$z_l = 0;\ 0 \leqslant y_l \leqslant H;\ 0 \leqslant x \leqslant L;\ v_l = 0, \tag{3.3}$$

$$z_l = \delta_l;\ 0 \leqslant y_l \leqslant H;\ 0 \leqslant x \leqslant L;\ \frac{\partial v_l}{\partial z_l} = 0. \tag{3.4}$$

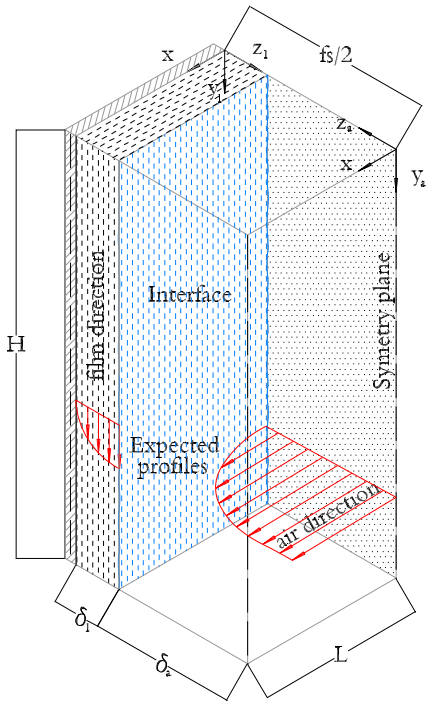

Figure 3.2: Schematic of cross flow falling film absorber operation

Integrating twice with respect to z_l, we obtain an analytical expression for velocity

$$v_l(z_l) = \frac{g}{\nu_l}\left(\delta_l z_l - \frac{z_l^2}{2}\right). \tag{3.5}$$

From continuity across the film and considering constant properties in x direction, it is possible to obtain an expression for the film thickness as function of the mass flow rate as follows

$$\delta_l = \left(\frac{3\dot{m}_l\nu_l}{\rho_l g}\right)^{\frac{1}{3}}. \tag{3.6}$$

Similar expressions are presented by Mills and Incropera [56, 57].

The energy balance is simplified to

$$v_l\frac{\partial T_l}{\partial y_l} = \alpha_l\frac{\partial^2 T_l}{\partial z_l^2}, \tag{3.7}$$

with boundary conditions

$$y_l = 0;\ 0 \leqslant z_l \leqslant \delta_l;\ 0 \leqslant x \leqslant L;\ T_l = T_{l,i}, \tag{3.8}$$

$$z_l = 0;\ 0 \leqslant y_l \leqslant H;\ 0 \leqslant x \leqslant L;\ \frac{\partial T_l}{\partial z_l} = 0, \tag{3.9}$$

$$z_l = \delta_l;\ 0 < y_l \leqslant H;\ 0 \leqslant x \leqslant L;\ T_l = T_a. \tag{3.10}$$

The mass balance equation takes the form

$$v_l \frac{\partial C}{\partial y_l} = \mathcal{D}_l \frac{\partial^2 C}{\partial z_l^2}. \tag{3.11}$$

with boundary conditions

$$y_l = 0;\ 0 \leqslant z_l \leqslant \delta_l;\ 0 \leqslant x \leqslant L;\ C = C_i, \tag{3.12}$$

$$z_l = 0;\ 0 \leqslant y_l \leqslant H;\ 0 \leqslant x \leqslant L;\ \frac{\partial C}{\partial z_l} = 0. \tag{3.13}$$

3.3.2 Moist air

Similar to the liquid part, the velocity of the air in the x_a and y_a directions are considered negligible, and the continuity equation is simplified to

$$\frac{\partial u_a}{\partial x} = 0. \tag{3.14}$$

In this case, the $x-$momentum equation is required

$$\frac{\partial p_a}{\partial x} = \mu_a \frac{\partial^2 u_a}{\partial z_a^2}, \tag{3.15}$$

with boundary conditions

$$z_a = 0;\ 0 \leqslant y_a \leqslant H;\ 0 \leqslant x \leqslant L;\ \frac{\partial u_a}{\partial z_a} = 0, \tag{3.16}$$

$$z_a = \delta_a;\ 0 \leqslant y_a \leqslant H;\ 0 \leqslant x \leqslant L;\ u_a = 0. \tag{3.17}$$

Using momentum and continuity equations it is possible to solve for an analytical expression for the u_a velocity profile

$$u_a = \frac{1}{2\mu_a} \frac{\partial p}{\partial x} \left(z_a^2 - \delta_a^2 \right), \tag{3.18}$$

where

$$\frac{\partial p_a}{\partial x} = -\frac{3\mu_a \dot{m}_a}{\rho_a \delta_a^3 H}, \tag{3.19}$$

as presented by Mills and Incropera [56, 57].

The energy and mass balance are represented by the following expressions

$$u_a \frac{\partial T_a}{\partial x} = \alpha_a \frac{\partial^2 T_a}{\partial z_a^2}, \tag{3.20}$$

$$u_a \frac{\partial W}{\partial x} = \mathcal{D}_a \frac{\partial^2 W}{\partial z_a^2}, \tag{3.21}$$

with boundary conditions

$$x = 0;\ 0 \leqslant y_a \leqslant H;\ 0 \leqslant z_a \leqslant \delta_a;\ T_a = T_{a,i};\ W = W_i, \tag{3.22}$$

$$z_a = \delta_a;\ 0 \leqslant y_a \leqslant H;\ 0 \leqslant x \leqslant L;\ T_l = T_a;\ W = W_{int}, \tag{3.23}$$

$$z_a = 0;\ 0 \leqslant y_a \leqslant H;\ 0 \leqslant x \leqslant L;\ \frac{\partial T_a}{\partial z_a} = 0;\ \frac{\partial W}{\partial z_a} = 0, \tag{3.24}$$

where W_{int} and p_v are

$$W_{int} = 0.62185 \frac{p_v}{(p_t - p_v)}, \tag{3.25}$$

$$p_v = p_{v,H_2O}(1 - 0.828Cc - 1.496Cc^2 + Cc\frac{(T_{int} - 40)}{350}). \tag{3.26}$$

Vapor pressure (p_v) is formulated in terms of vapor pressure of water at the same temperature (p_{v,H_2O}), calcium chloride concentration (Cc) and temperature at the interface (T_{int}).

3.3.3 Interface energy and mass balances

At $z_l = \delta_l$, $0 \leqslant x \leqslant L$ and $0 \leqslant y \leqslant H$ the liquid−air interface balance is shown in Fig. 3.3.

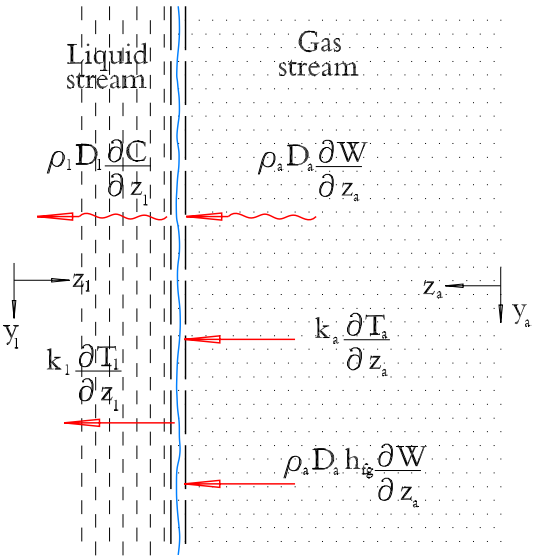

Figure 3.3: Interface energy and species balances

$$-k_l \frac{\partial T_l}{\partial z_l} = k_a \frac{\partial T_a}{\partial z_a} + \rho_a \mathcal{D}_a h_{gf} \frac{\partial W}{\partial z_a}, \tag{3.27}$$

$$-\rho_l \mathcal{D}_l \frac{\partial C}{\partial z_l} = \rho_a \mathcal{D}_a \frac{\partial W}{\partial z_a}. \tag{3.28}$$

Continuity of temperature at the interface is applied but the concentration may be discontinuous. Also, the interface concentration is obtained from Eq. 3.25, once the interface temperature is known. Assuming thermodynamic equilibrium at the interface and the air mixture to be an ideal gas, the vapor pressure of the liquid desiccant ($p_{v,l}$) at the interface is equal to the partial pressure of the water vapor ($p_{v,a}$) in the air-vapor mixture.

$$z_l = \delta_l;\ z_a = \delta_a;\ 0 \leqslant y_{l,a} \leqslant H;\ 0 \leqslant x \leqslant L;$$

$$T_l = T_a, \tag{3.29}$$

$$p_{v,l} = p_{v,a}. \tag{3.30}$$

3.4 Numerical approximation

Governing equations of energy and mass transfer for both air and liquid falling film are solved using finite difference approximation. The axial convection terms are approximated by upstream differences and the diffusion terms are expressed by central differences. Several grid points in inlet regions are used to handle large changes. Grid independence of the numerical predictions in all three dimensions was checked. The following procedure was adapted from Ali and Vafai [55] and will be employed in the analysis:

(a) Input inlet conditions for mass flow rate, temperature, humidity ratio, and concentration for both air and desiccant film as well as and the dimension of the device.

(b) Calculate the film thickness and pressure gradient from the custom formulas and then compute the velocity profiles for the air and liquid desiccant film.

(c) Assume interfacial humidity ratio and temperature for the whole domain ($z_l = \delta_l$ or $z_a = \delta_a$, $0 \leq x \leq L$ and $0 \leq y_{a,l} \leq H$).

(d) Solve the humidity ratio for the air and desiccant concentration by marching through the whole domain.

(e) Solve the temperature distribution for the desiccant film and air by marching through the whole domain.

(f) Compute the interfacial air concentration from Eq. (4.15). for the whole domain. Now it is possible to find a new interfacial temperature and concentration at the liquid side.

(g) If the maximum error between the calculated values and assumed ones are greater than the convergence criterion, update the assumed interface values by the calculated values and repeat (d)−(g) until the values of the interfacial humidity ratio converges.

3.5 Results and discussion

A comparative numerical approximation of a heat and mass transfer for an adiabatic parallel-plate absorber for which a thin film of liquid desiccant flows down its walls and dehumidifies the air in cross-flow configuration is developed. The performance of the absorber is analyzed as a function of inlet air temperature

Table 3.1: Comparison between outlet air temperature and humidity ratio for the actual investigation and Park

				Park		Current		
Cc_{in} (%)	$T_{l,in}$ (°C)	W_{in} (−)	$T_{a,i}$ (°C)	W_{out} (−)	$T_{a,out}$ (°C)	W_{out} (−)	$T_{a,out}$ (°C)	error (%)
75	23.28	20.89	29.44	11	22.1	10.9	23.6	6.9
76	23.67	21.03	29.56	11	22.5	10.9	24	6.7
78	24.00	20.95	29.51	12	23.4	11.8	24.3	4
80	24.00	20.82	29.61	11	23.5	10	24.3	3.5
82	24.72	21.09	29.61	10	23.6	9.8	25	6

Table 3.2: Operating parameters and properties used

Parameter	Units	Desiccant region	Air region
$T_{a,i}$	°C		$0-5$
$T_{l,i}$	°C	$5-8$	
W_i	$\text{kg}_w\ \text{kg}_{da}^{-1}$		$0.006-0.002$
C_i	$\text{kg}_w\ \text{kg}_{sol}^{-1}$	0.65	
$\dot{m}_a$	kg s^{-1}		0.00328
$\dot{m}_l$	kg m^{-1} s^{-1}	0.001786	
k	W m^{-1} K^{-1}	0.525	0.02635
Cp	J kg^{-1} K^{-1}	2330	1028
ρ	kg m^{-3}	1394	1.172
μ	kg m^{-1} s^{-1}	1.19×10^{-2}	1.83×10^{-5}
$\mathcal{D}$	m^2 s^{-1}	4.2^{-10}	2.5×10^{-5}
h_{fg}	J kg^{-1} K^{-1}		2.448×10^{6}

and relative humidity, inlet liquid desiccant temperature, mass flow rates of air and liquid desiccant, and liquid desiccant concentration. The model was validated against the results obtained by Park [54] for ambient temperature conditions. Table 3.1 shows the results of the comparison where the percentage errors were computed using the outlet temperatures. Uncertainty in the values of the fluid properties and the grid size account for most of the percentage error.

Table 3.2 shows the properties used to run the simulation for the cold storage conditions. Contours of interfacial and average film and air properties (temperature and concentration) are shown for specific operating conditions. Figure 3.4 shows the distribution of water concentration in the liquid desiccant at the interface. The portion of the liquid desiccant flowing near the entrance of the air side shows larger levels of water content compared to section near the end of the absorber's depth. This driving potential for mass transfer also affect the temper-

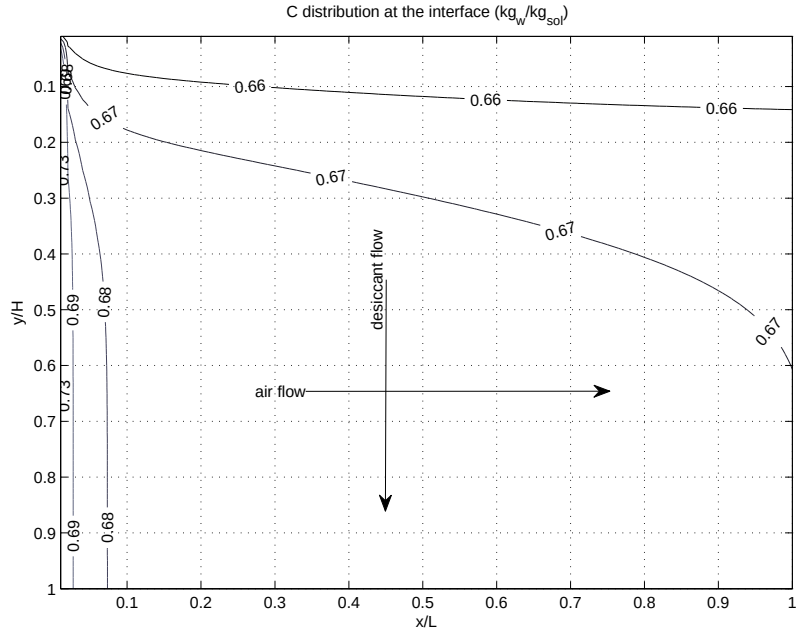

Figure 3.4: Distribution of water concentration at the interface in the liquid domain.

ature distribution at the interface, as shown in Fig. 3.5. Since the air enters the absorber at a low temperature, the rise in liquid desiccant temperature is not significant. Figure 3.6 shows the moisture distribution on the air side at the interface between air and liquid desiccant.

Average distributions of water concentration in the full air and liquid domains are presented in Figs. 3.7 and 3.8. The concentration is seen to decrease in its flow direction but to increase in the air flow direction, for the liquid and air-side, respectively.

The purpose of the liquid desiccant system is to remove the moisture of the air before it reaches the surface of the evaporator where it will condensate and then form a layer of ice. If the absorber lowers the dew point temperature of the air to a value below the surface temperature of the evaporator then condensation will not occur. Test data of realistic operating conditions inside a cold storage were obtained in chapter 2 [13]. Temperature and relative humidity measurements were obtained for air upstream of the evaporator. Evaporator surface temperature measurements were also taken at the cold storage facility. Relative humidity and temperature measurements were taken with Veris sensors which have accuracy of

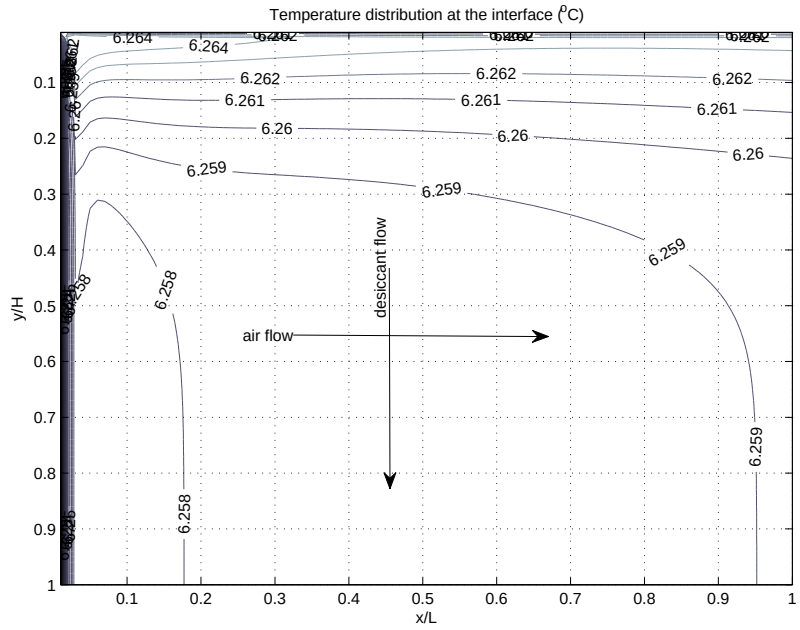

Figure 3.5: Distribution of Temperature at the interface for both air and liquid domain.

$\pm$ 0.3°C in temperature and $\pm$ 3% RH. The dew point temperatures were obtained from this data [58]. From a selected set of data where the operative conditions of the warehouse were stable, the confidence intervals from 90% to 75% were obtained. The model of the absorber developed in this work was used to design a dehumidifier core that would remove moisture of the air avoiding the formation of frost on the evaporator surface.

Figure 3.9 shows the values of the dew point temperature of the air upstream of the evaporator during a complete defrosting cycle. The figure also shows the predicted dew point temperature of the air exiting the absorber calculated using the numerical model. It is shown that the outlet dew point temperature of the air leaving the absorber is below the evaporator surface temperature preventing the formation of ice on the surface of the evaporator.

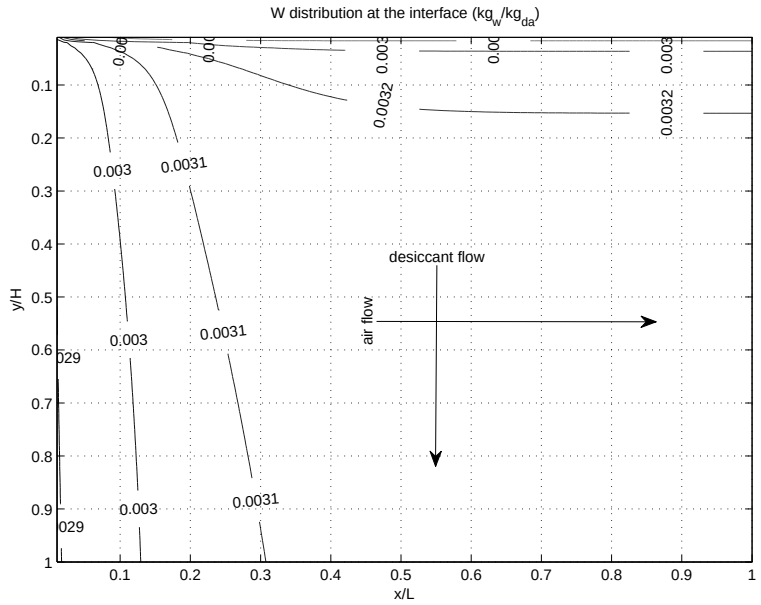

Figure 3.6: Distribution of water concentration at the interface in the air domain.

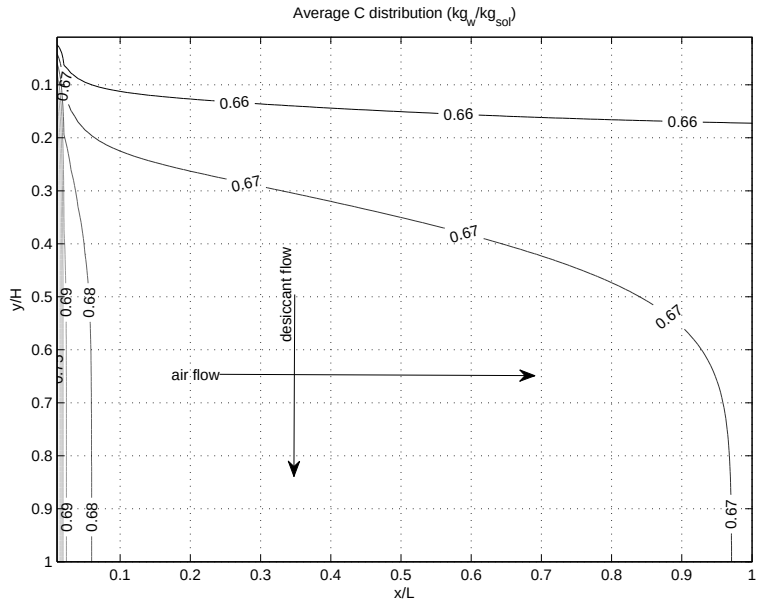

Figure 3.7: Average distribution of water concentration in the liquid domain.

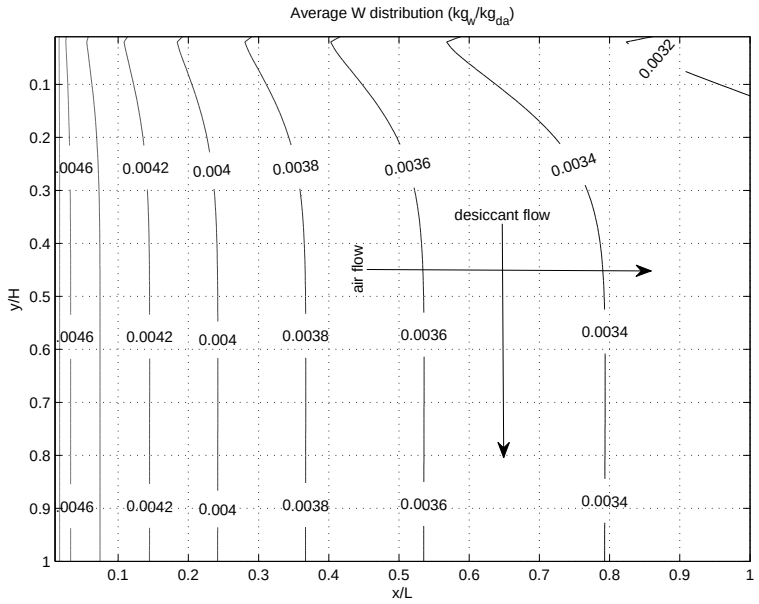

Figure 3.8: Average distribution of water concentration in the air domain.

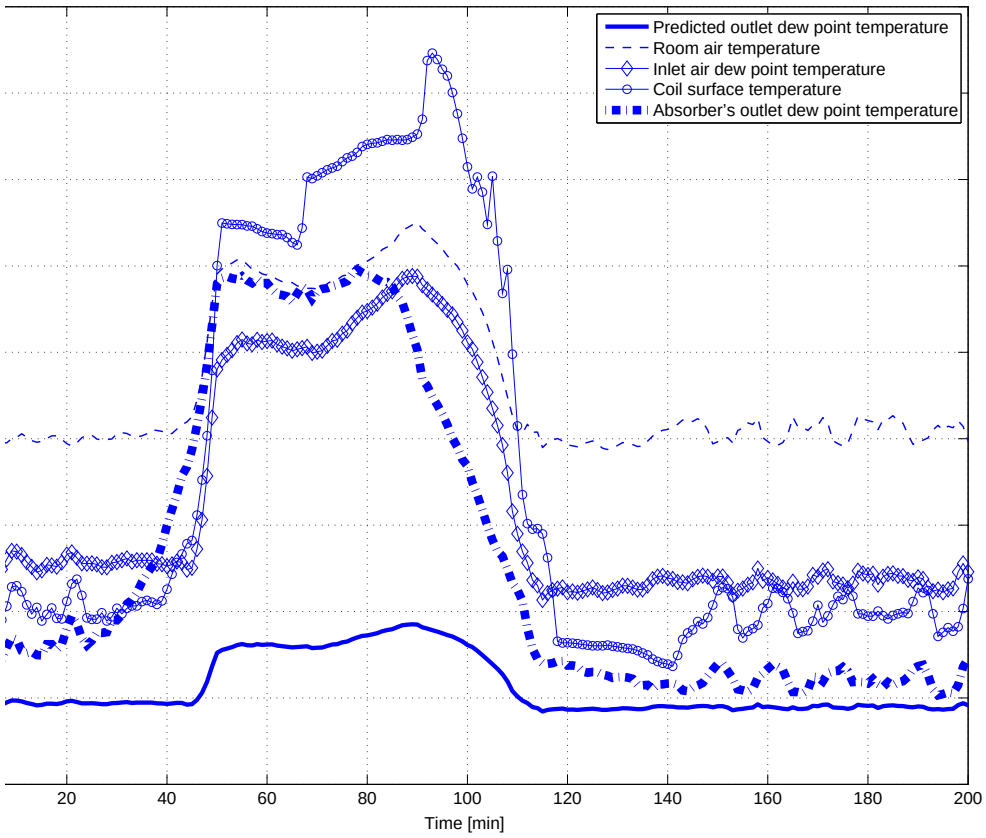

Figure 3.9: Comparison between inlet air dew point, a predicted outlet dew point from the numerical model and experimental absorbers outlet dew point temperatures. The accuracy of the sensors is ± 0.3°C in temperature and ± 3% RH.

3.6 Conclusions

The coupled heat and mass transfer between a calcium chloride solution liquid desiccant falling film and moist air in cross flow was studied. Due to the low temperature of the air, an adiabatic absorber is utilized. Realistic operating conditions were obtained from a cold storage facility. The results show that an absorber can be designed to effectively eliminate the formation of ice on the surface of the evaporator.

Acknowledgment

This work has been supported by the California Energy Commission and the California Institute for Energy and Environment contract number MR-07-04. The authors would like to thanks Aslan Cold Storage, LLC for allowing access to their facilities to obtain measurements of realistic refrigerated warehouse conditions.

Chapter 4

Contribution of an internal heat exchanger to the performance of a liquid desiccant dehumidier operating near freezing conditions

The aim of the present study is to analyze numerically the effect of an internal heat exchanger (IHX) in a liquid-desiccant based dehumidification system operating near freezing conditions that are typical of a refrigerated warehouse. The study is based on previous work done by the authors that showed reduced ice formation on the surface of a cooling coil by dehumidifying the air using liquid desiccants. The results of the present study show that IHX effectiveness has a direct impact on the inlet temperature of the liquid desiccant leaving the absorber. High IHX effectiveness results in high absorber effectiveness. However, IHX effectiveness less than 60% leads to a desorption process where the liquid desiccant concentration increases, augmenting the humidity ratio of the air going through the mass exchanger.

4.1 Introduction

The growth in the demand for energy has been projected to increase by about 50 percent from 2005 to 2030 [16]. The main source of energy to match this demand will come from fossil fuels that are currently facing increasing uncertainty with respect to their long-term availability. They also play an important role in augmenting the emission of greenhouse gases to the atmosphere [17, 39]. A feasible option for matching rising demand without increasing power gener-

ation is to improve energy efficiency in residential, commercial, and industrial applications. One example of an energy intensive industrial application is the refrigerated warehouse sector. A refrigerated warehouse operates as a traditional vapor-compression refrigeration cycle. The evaporator is installed inside the cold storage and the compressor and cooling towers are located outside. Agricultural produce is brought in and out of the pre-cooling rooms allowing hot and humid air to enter the cold storage. The quality of the produce is maintained by keeping a high relative humidity inside the room and the temperature remains near freezing conditions. These operating conditions translate into a continuous formation of ice on the surface of the evaporator. Therefore, defrosting cycles are run between one to three times a day to remove the ice from the evaporator. Defrosting cycles are inherently inefficient since they raise the surface temperature of the evaporator and involve the use of natural gas, propane, or water sprays to melt the ice.

Hybrid vapor-compression/liquid-desiccant cooling systems have been analyzed in the past as an alternative that reduces energy consumption in air conditioning and refrigeration applications. Yadav [40] suggested energy savings of up to 80% when the latent load constitutes 90% of the total cooling load with a liquid-desiccant dehumidifier regenerated by solar energy. Pineda and Diaz showed reduced energy and defrosting-water consumption in cold storages where a liquid desiccant absorber was used to remove moisture from the air upstream of the evaporator [13, 14, 59].

Although a number of researchers have analyzed dehumidification and cooling systems that utilize liquid desiccants [19,34,54,55,60,61] the study of liquid desiccant systems operating near freezing conditions has received little attention. A literature review of the theoretical and physical models of a refrigerated warehouse, as well as, the comparisons between a traditional vapor-compression cycle and a liquid desiccant refrigeration cycle are found in [34]. Elsayed et al. [37] analyzed the performance of an air cycle refrigerator combined with a desiccant rotor for an air conditioning application. More recently, the same authors numerically analyzed the performance of an air cycle refrigerator integrated with a desiccant system for cooling and dehumidifying a warehouse [38]. They found that the coefficient of performance (COP) can increase more than one hundred percent with respect to a conventional system. In general, COP improvement in vapor-compression systems using liquid desiccants is shown to depend on three main factors: the type of liquid desiccant used [21, 41], the effectiveness of the dehumidifier and regenerator [18, 34], and the effectiveness of the internal heat exchanger [14]. However, the effect of the IHX on the performance of a liquid-desiccant system (LDS) has not been analyzed in depth.

Internal heat exchangers are used in refrigeration and air conditioning systems to assure proper system operation and to improve performance [62, 63]. Positive benefits in terms of increased COP have been shown by a number of researchers [64–66]. For instance, Vijayan and Srinivasan [66] found that inclusion of an IHX in a window air conditioning unit increased COP by 5.86% for refrigerant R22 and by 6.30% for R407C. However, an IHX can also have a negative influence on the overall performance of the refrigeration cycle. Navarro et. al. [62] analyzed a refrigeration cycle with and without an IHX for several working fluids detecting that the pressure drop introduced by this device is of significant importance. In general, the adoption of an IHX depends on thermophysical properties of the working fluid and the inlet temperatures to the compressor and evaporator. Typical applications of IHXs are seen in CO_2 transcritical air conditioning systems and heat pumps [67, 68].
This work focusses on the effect of the IHX utilized for thermal preconditioning of the liquid desiccant in order to enhance its absorption capabilities before it enters the absorber. Reduction in liquid-desiccant vapor pressure is obtained by reducing its temperature before entering the absorber and thus, better air dehumidification performance is obtained. The thermophysical properties used in the development of the models have been obtained from current published data on liquid desiccants [69, 70].

4.2 System description

The operation of a liquid desiccant system at a refrigerated warehouse is depicted in Fig. 4.1, that shows how the processes of absorption and regeneration take place at different locations. A concentrated solution of liquid desiccant is pumped at ambient temperature from the bottom of the reservoir tank to the high-pressure side of the IHX and then to the absorber device. At the absorber, the desiccant falls down the walls as a liquid film that is in contact with cold and humid air flowing across the absorber. The indoor air conditions range between 0 and 4 °C and 80 to 100% RH [59]. The dehumidified air is sent directly to the cold storage evaporator, reducing the formation of ice at its surface. The cold and diluted liquid desiccant exits the absorber and is driven by gravity through the low-pressure side of the IHX where it exchanges energy with the liquid desiccant stream on the high-pressure side, lowering its temperature and thus, enhancing its absorption capabilities. The liquid desiccant leaving the low-pressure side of the IHX drains to the top of the storage tank. Liquid desiccant is pumped from the top of the storage tank to the regenerator where low-relative-humidity ambient air regenerates the liquid desiccant increasing its concentration [13].

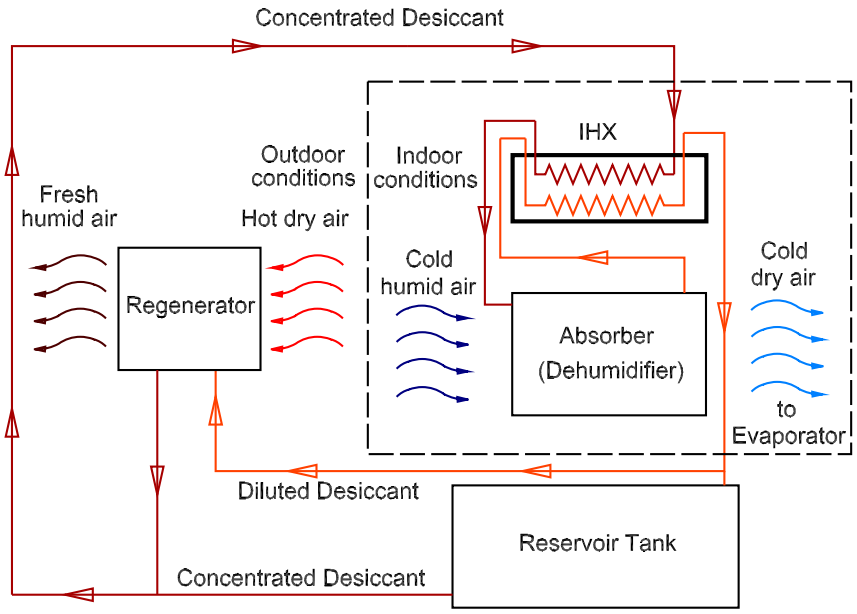

Figure 4.1: Absorption-regeneration cycle for the liquid desiccant system operating at a refrigerated warehouse.

In the system being analyzed, the IHX is used with the objective of lowering the temperature of the liquid desiccant and thus, augmenting its absorption properties before it enters the dehumidification device. Figure 4.2 shows the IHX device (A) connected to the input and output of the absorber core (B). The exchange of heat between the high and low-pressure sides of the IHX occurs in counter flow configuration.

4.3 Numerical model

In this study a liquid desiccant absorber model, already developed and validated by the authors [13, 14, 59, 71], is used in combination with a model of an internal heat exchanger to analyze the effect of the IHX on the dehumidifying performance of the absorber core. The setup being studied is shown in Fig. 4.2. The following assumptions are used in the analysis:

- Laminar flow and fully developed conditions are used.
- Heat losses to the surroundings from the internal heat exchanger are neglected.

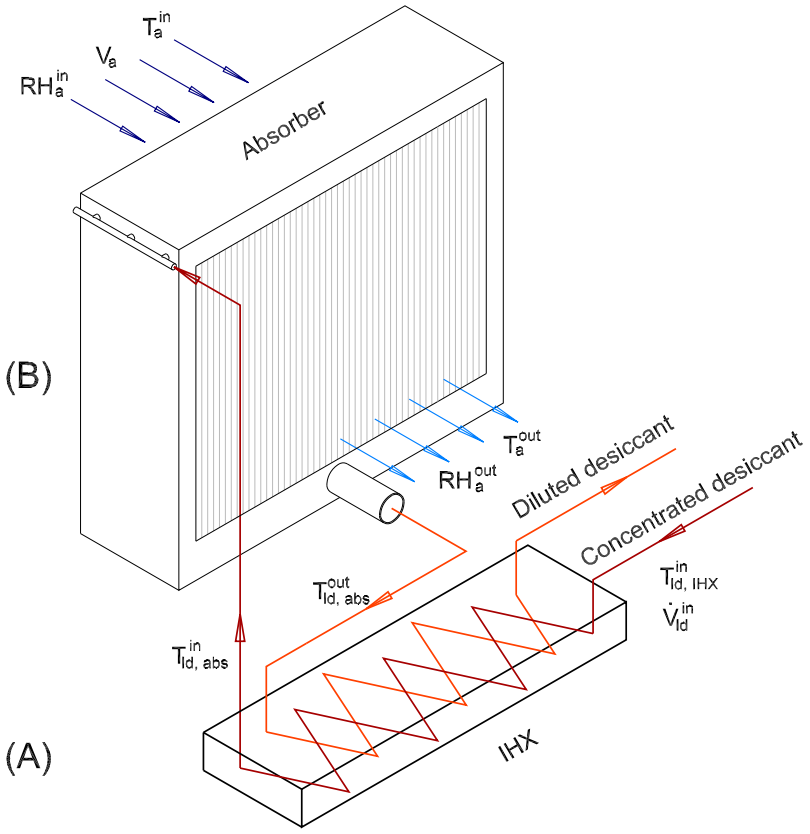

Figure 4.2: Schematic of the connections between internal heat exchanger and absorber.

- Based on the narrow temperature range studied, constant fluid properties are utilized.
- Steady state conditions are utilized.
- Counter-flow configuration in the internal heat exchanger is considered.
- Negligible thermal resistance at walls and fouling factors.
- The pressure drop in connecting pipelines, hoses, and bends are assumed negligible.

4.3.1 Absorber

For the dehumidification device, a three-dimensional cross-flow model between a liquid-desiccant film falling on parallel plates and a horizontal humid-air stream was utilized [14, 59], where the continuity equation, and equations of motion, energy, and mass transfer are considered in the liquid domain as follows:

$$\frac{\partial v_l}{\partial y_l} = 0, \tag{4.1}$$

$$\mu_l \frac{\partial^2 v_l}{\partial z_l^2} + \rho_l g = 0, \tag{4.2}$$

$$v_l \frac{\partial T_l}{\partial y_l} = \alpha_l \frac{\partial^2 T_l}{\partial z_l^2}, \tag{4.3}$$

$$v_l \frac{\partial C}{\partial y_l} = \mathcal{D}_l \frac{\partial^2 C}{\partial z_l^2}, \tag{4.4}$$

with boundary conditions

$$y_l = 0;\ 0 \leqslant z_l \leqslant \delta_l;\ 0 \leqslant x \leqslant L;\ T_l = T_{l,i};\ C = C_i, \tag{4.5}$$

$$z_l = 0;\ 0 \leqslant y_l \leqslant H;\ 0 \leqslant x \leqslant L;\ v_l = 0;\ \frac{\partial T_l}{\partial z_l} = 0;\ \frac{\partial C}{\partial z_l} = 0, \tag{4.6}$$

$$z_l = \delta_l;\ 0 < y_l \leqslant H;\ 0 \leqslant x \leqslant L;\ \frac{\partial v_l}{\partial z_l} = 0;\ T_l = T_a. \tag{4.7}$$

Similarly, continuity, momentum, energy, and mass transfer equations for the humid-air region are considered as follows:

$$\frac{\partial u_a}{\partial x} = 0, \tag{4.8}$$

$$\frac{\partial p_a}{\partial x} = \mu_a \frac{\partial^2 u_a}{\partial z_a^2}, \tag{4.9}$$

$$u_a \frac{\partial T_a}{\partial x} = \alpha_a \frac{\partial^2 T_a}{\partial z_a^2}, \tag{4.10}$$

$$u_a \frac{\partial \omega}{\partial x} = \mathcal{D}_a \frac{\partial^2 \omega}{\partial z_a^2}, \tag{4.11}$$

with boundary conditions

$$x = 0;\ 0 \leqslant y_a \leqslant H;\ 0 \leqslant z_a \leqslant \delta_a;\ T_a = T_{a,i};\ \omega = \omega_i, \tag{4.12}$$

$$z_a = 0;\ 0 \leqslant y_a \leqslant H;\ 0 \leqslant x \leqslant L;\ \frac{\partial u_a}{\partial z_a} = 0;\ \frac{\partial T_a}{\partial z_a} = 0;\ \frac{\partial \omega}{\partial z_a} = 0, \tag{4.13}$$

$$z_a = \delta_a;\ 0 \leqslant y_a \leqslant H;\ 0 \leqslant x \leqslant L;\ u_a = 0;\ T_l = T_a;\ \omega = \omega_{int}, \tag{4.14}$$

where ω_{int} and p_v are

$$\omega_{int} = 0.62185 \frac{p_v}{(p_t - p_v)}, \tag{4.15}$$

$$p_v = p_{v,H_2O}(1 - 0.828(1 - C) - 1.496(1 - C)^2 + (1 - C)\frac{(T_{int} - 40)}{350}). \tag{4.16}$$

Additionally, energy and mass balances at the liquid−air interface are also considered as follows:

$$-k_l \frac{\partial T_l}{\partial z_l} = k_a \frac{\partial T_a}{\partial z_a} + \rho_a \mathcal{D}_a h_{gf} \frac{\partial \omega}{\partial z_a}, \tag{4.17}$$

$$-\rho_l \mathcal{D}_l \frac{\partial C}{\partial z_l} = \rho_a \mathcal{D}_a \frac{\partial \omega}{\partial z_a}. \tag{4.18}$$

Finally, the effectiveness of the absorber is defined in Eq. 4.19,

$$\epsilon_{abs} = \frac{\omega^{in} - \omega^{out}}{\omega^{in} - \omega^{eq}}, \tag{4.19}$$

where ω^{eq} is the humidity ratio of the air, which is in equilibrium with the desiccant solution at the local solution temperature and concentration [72].

4.3.2 Internal heat exchanger

The thermal effectiveness of the IHX is calculated as follows:

$$\epsilon_{IHX} = \frac{\dot{Q}}{\dot{Q}_{max}} = \frac{U_H(T^{in}_{IHX} - T^{in}_{ld,abs})}{U_{min}(T^{in}_{IHX} - T^{out}_{ld,abs})}, \tag{4.20}$$

where $U = \dot{m}c_p$, and T^{in}_{IHX} is the inlet temperature to the high-pressure side of the IHX, $T^{in}_{ld,abs}$ is the outlet of the high-pressure side of the IHX which is the same as the inlet liquid-desiccant temperature to the absorber, and $T^{out}_{ld,abs}$ is the inlet temperature to the low-pressure side of the IHX which is the same as the outlet

Table 4.1: Operating conditions for the simulations

Inlet air temperature to absorber	2	°C
Inlet air relative humidity to absorber	90	%
Inlet air velocity to absorber	1.6	m s^{-1}
Inlet liquid desiccant temperature to IHX	20	°C
Mass flow rate of liquid desiccant per unit depth	0.0005	kg m^{-1} s^{-1}
Inlet liquid desiccant concentration	35	%

desiccant solution temperature of the absorber. As fluid properties are considered constant and the mass flow rate on the high and low-pressure side of the IHX are approximately the same, i.e. rate of moisture absorption is small compared to the liquid desiccant flow rate [54, 73], then the effectiveness of the internal heat exchanger depends on temperatures only.

4.3.3 Operating conditions for the simulations

The operating conditions used for the heat and mass exchangers have been obtained from measurements at an actual prototype liquid-desiccant system previously analyzed by the authors [13, 59]. A typical pre-cooling room that stores produce during a number of hours operates at a range of temperatures between 0 and 4°C and between 80 and 100% of relative humidity. The values utilized for the input parameters to the model are summarized in Table 4.1.
Due to availability of experimental test data obtained previously by the authors [13], Calcium Chloride solution was used as liquid desiccant during the simulations. Liquid desiccants absorb moisture from humid air mainly due to the difference in vapor pressure between the air and the desiccant solution. The vapor pressure of a liquid desiccant tends to zero at low temperatures. Thus, absorption capacity is increased by lowering the temperature of the desiccant solution or by increasing its concentration. It is important to operate the liquid desiccant system at conditions where crystallization is not reached. Figure 4.3 shows the properties of calcium chloride solution including the change in vapor pressure from 8 to 3.5 mm Hg for calcium chloride solution at 35% concentration for a change in temperature from an inlet value of 20°C to 4°C. This process could be obtained utilizing an internal heat exchanger.

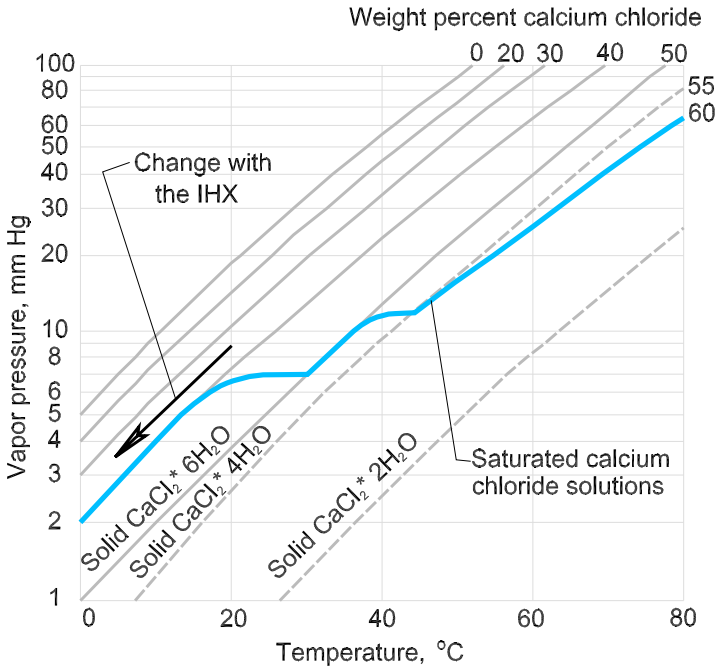

Figure 4.3: Vapor pressure change at constant liquid-desiccant concentration due to temperature change. This change in temperature can be obtained using an internal heat exchanger.

Table 4.2: Inlet simulation conditions: T_a^{in}= 2°C, RH_a^{in}= 90%, C_{ld}^{in}= 35%, and T_{IHX}^{in}= 20°C.

ϵ_{IHX} [%]	$T_{ld,abs}^{in}$ [°C]	ω_a^{out} [$\frac{kg_m}{kg_{da}}$]	T_a^{out} [°C]	$T_{ld,abs}^{out}$ [°C]	C_{ld}^{out}
90	5.8	0.0028	4.3	4.2	32.9
80	8.8	0.0032	6.1	6.0	33.5
70	11.1	0.0035	7.5	7.3	33.9
60	13.1	0.0038	8.7	8.5	34.4
50	14.7	0.0041	9.6	9.4	34.7
40	16.1	0.0043	10.5	10.2	35.1
30	17.3	0.0045	11.2	10.9	35.3
20	18.3	0.0047	11.8	11.5	35.6
10	19.2	0.0049	12.3	12.0	35.8
0	20	0.0051	12.8	12.5	36.0

4.4 Results and discussion

The effect of the IHX effectiveness on the absorber outlet air temperature and humidity ratio, and liquid-desiccant temperature and concentration is studied first. Considering fixed inlet conditions given by T_a^{in}= 2°C, RH_a^{in}= 90%, C_{ld}^{in}= 35%, and T_{IHX}^{in}= 20°C, the combined models of the absorber and IHX are utilized to obtain the values of ω_a^{out}, T_a^{out}, $T_{ld,abs}^{out}$, and C_{ld}^{out} based on prescribed values of IHX effectiveness. The results of the simulations are presented in Table 4.2. The table shows that for a high IHX effectiveness such as ϵ_{IHX}= 90% the liquid desiccant temperature entering the absorber, $T_{ld,abs}^{in}$, is reduced from 20°C to 5.8°C by the IHX. Thus, at these conditions the humidity ratio of the air is reduced from approximately 0.00392kg$_m$/kg$_{da}$ (for T_a^{in}= 2°C, RH_a^{in}= 90%) to 0.0028kg$_m$/kg$_{da}$. Moisture from the air is absorbed by the liquid desiccant which lowers its concentration from the initial 35% to 32.9%. The outlet temperatures of air and liquid desiccant at the absorber are 4.3°C and 4.2°C, respectively. As the effectiveness of the IHX decreases, $T_{ld,abs}^{in}$ increases and the absorber becomes less effective in dehumidifying the air. The relationship between IHX effectiveness and the inlet liquid desiccant temperature to the absorber is shown in Fig 4.4.

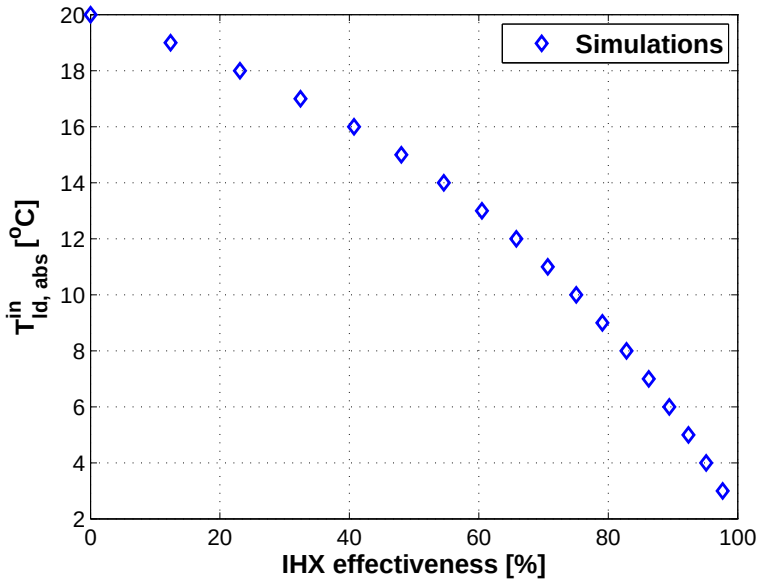

Figure 4.4: Inlet liquid desiccant temperature at the absorber as a function of IHX effectiveness. Absorber inlet conditions are: T_a^{in}= 2°C, RH_a^{in}= 90% and C_{ld}^{in}= 35%.

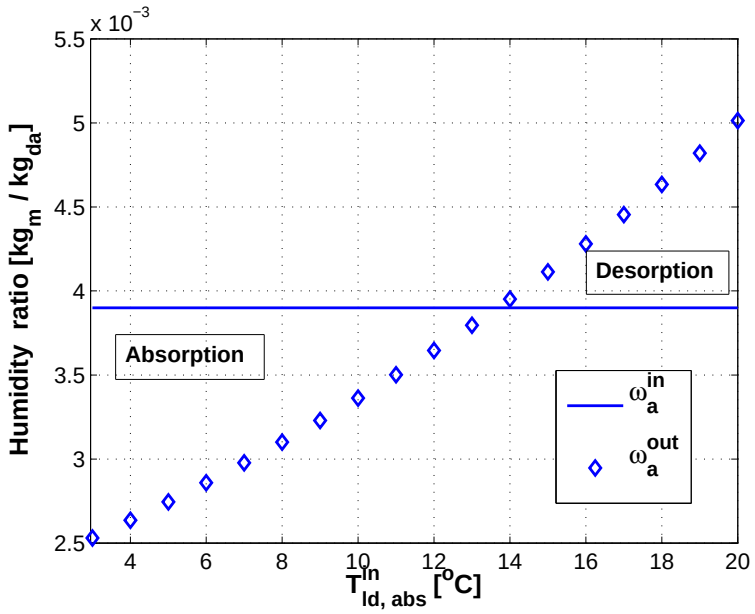

Figure 4.5: Outlet air humidity ratio as a function of absorber inlet temperature of the liquid desiccant. The continuous horizontal line represent the inlet humidity ratio and diamonds represent outlet humidity ratio.

When ϵ_{IHX} is very low, the liquid desiccant enters the absorber near the inlet temperature to the IHX (T^{in}_{IHX}= 20°C) and for conditions where $\epsilon_{IHX} \leq 50\%$, the absorber starts acting as a regenerator by increasing the air humidity ratio. This effect is observed in Fig. 4.5 where the horizontal line denotes the inlet air humidity ratio to the absorber, ω^{in}_a, and the outlet humidity ratio, ω^{out}_a, is represented with diamonds. As the inlet liquid desiccant temperature to the absorber increases, the process changes from air dehumidification to liquid-desiccant regeneration. Outlet humidity ratio versus IHX effectiveness is seen in Fig. 4.6 where at the simulated operating conditions, the dehumidification process stops near IHX effectiveness of 50% or lower.

As $T^{in}_{ld,abs}$ increases, the absorber becomes less effective in dehumidifying the air and eventually, it starts adding moisture to the air. The outlet liquid desiccant becomes less diluted and the concentration becomes higher than the initial value. Figure 4.7 shows this effect, where the inlet liquid concentration, C^{in}_{ld}, is shown as a continuous horizontal line and the outlet liquid-desiccant concentration as circles. It is observed that diluted desiccant with concentration near 32% is obtained at low $T^{in}_{ld,abs}$ which occurs at high IHX effectiveness, but for $T^{in}_{ld,abs} \geq 16$°C the mass

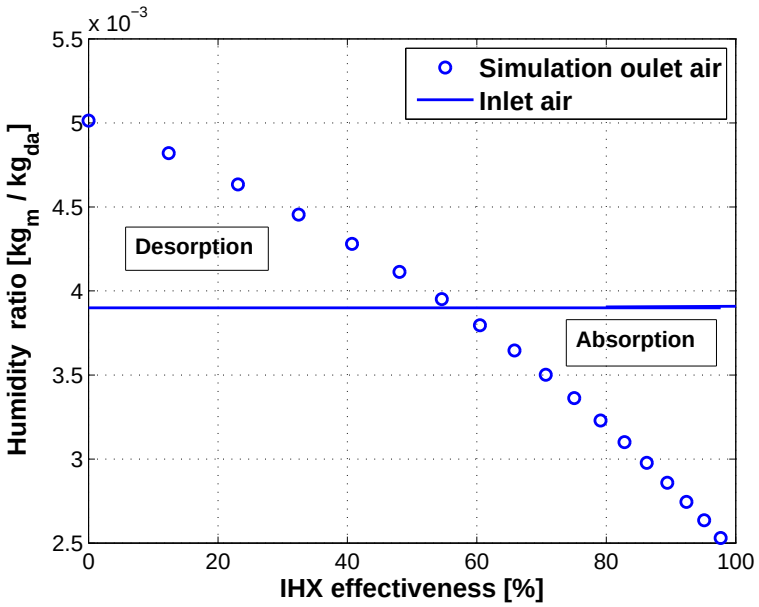

Figure 4.6: Outlet humidity ratio versus IHX effectiveness. The continuous horizontal line represent the inlet humidity ratio and circles represent outlet humidity ratio.

exchanger acts as a regenerator increasing the solution concentration with respect to inlet conditions.
Outlet temperatures of air and liquid desiccant are depicted in Fig. 4.8. As opposed to the slightly nonlinear behavior seen for ω_a^{out} and C_{ld}^{out} with respect to $T_{ld,abs}^{in}$, the outlet air and liquid desiccant temperatures, T_a^{out} and $T_{ld,abs}^{out}$, show a linear behavior with a slight divergence as $T_{ld,abs}^{in}$ increases.

The effect of the IHX effectiveness on the outlet conditions of the air going through the absorber are now shown by means of a Psychometric chart in Fig. 4.9. The arrows in the figure show the dehumidification (or humidification) of the air inside the refrigerated warehouse as a function of IHX effectiveness. It is seen how all the processes end-up at approximately the same outlet relative humidity, i.e. 55%, but with increasing dry-bulb temperatures. However, as the outlet air dry-bulb temperature increases, the initial negative slopes of the process change to positive indicating that the air humidity ratio increases for low ϵ_{IHX}. Therefore, it is clear from the figure that a liquid-desiccant based dehumidification system operating inside a refrigerated warehouse with outdoors regeneration, requires an internal heat exchanger in order to remove moisture from the air. If no IHX is

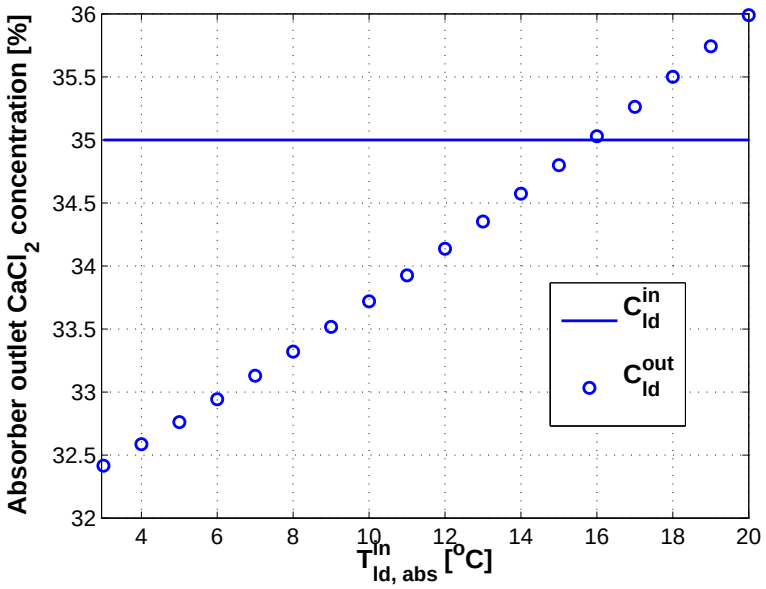

Figure 4.7: Outlet calcium chloride concentration versus inlet liquid desiccant temperature at the absorber. The continuous horizontal line represents the inlet solution concentration, circles represent outlet liquid-desiccant concentration.

used to lower the temperature of the concentrated liquid desiccant solution then the air going through the mass exchanger absorbs moisture instead of rejecting it.

Finally, the absorber effectiveness, given by Eq. 4.19, is plotted as a function of ϵ_{IHX}, as seen in Fig. 4.10. The reference horizontal line at zero absorber effectiveness, ϵ_{abs}, is added to indicate the separation between absorption and desorption behavior of the mass exchanger. It is observed that for the absorption process, a higher IHX effectiveness implies a higher absorber effectiveness. In order to have high absorber effectiveness, i.e. $\epsilon_{abs} > 50\%$, ϵ_{IHX} needs to be higher than 85%, approximately. The curve is extended to negative values of ϵ_{abs} only to show the desorption process when ϵ_{IHX} is low. The dehumidification system is not intended to operate under such conditions.

The findings obtained in this study indicate that under the operating conditions simulated, an internal heat exchanger is indeed required to dehumidify the air inside a refrigerated warehouse with a liquid desiccant solution. Moreover, the effectiveness of the IHX needs to be higher than 60%, otherwise desorption occurs.

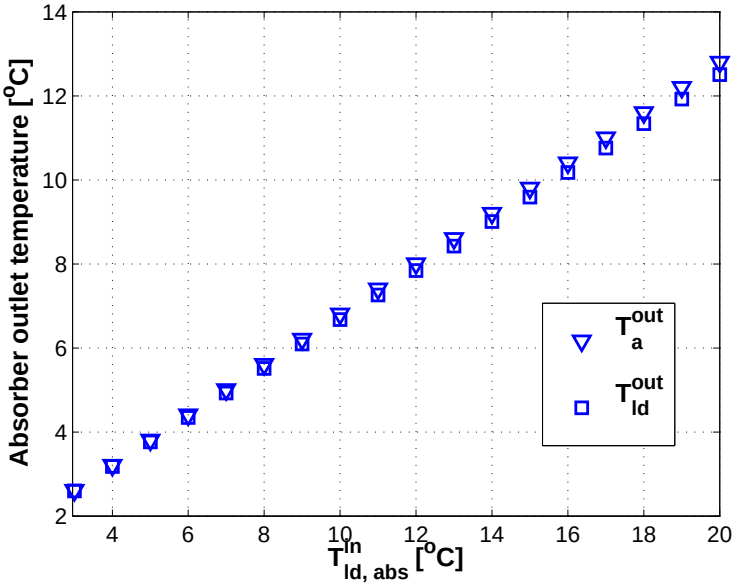

Figure 4.8: Outlet temperature for air and liquid desiccant solution versus inlet liquid desiccant temperature at the absorber.

4.5 Conclusions

The effect on liquid-desiccant absorber performance operating near freezing conditions as a function of internal heat exchanger effectiveness is studied numerically. An internal heat exchanger effectiveness model in combination with a previously validated model of a cross-flow absorber with liquid desiccant falling as a film through parallel plates in contact with humid air are used for the simulations. The operating conditions utilized to run the simulations are typical of a cold storage. The results show a strong dependency of the absorber performance with respect to IHX effectiveness. Values of ϵ_{IHX} greater than 60% are required to dehumidify the air. Low IHX effectiveness results in increased humidity ratio of the air going through the mass exchanger. The results also show a significant effect of ϵ_{IHX} in the liquid desiccant temperature at the outlet of the absorber.

4.6 Acknowledgment

This work was supported by the California Energy Commission and the California Institute for Energy and Environment contract # MR-07-04.

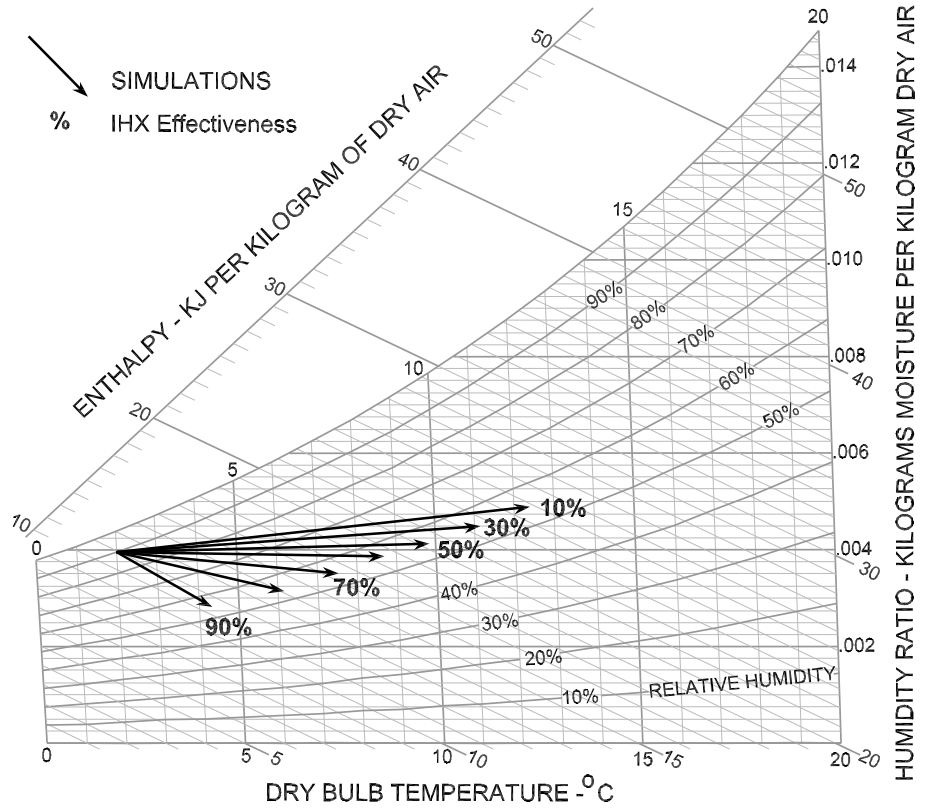

Figure 4.9: Absorption-desorption simulations for several IHX effectiveness. Typical absorber inlet conditions are: $T_a^{in} = 2°C, RH_a^{in} = 90\%$ and $C_{ld}^{in} = 35\%$.

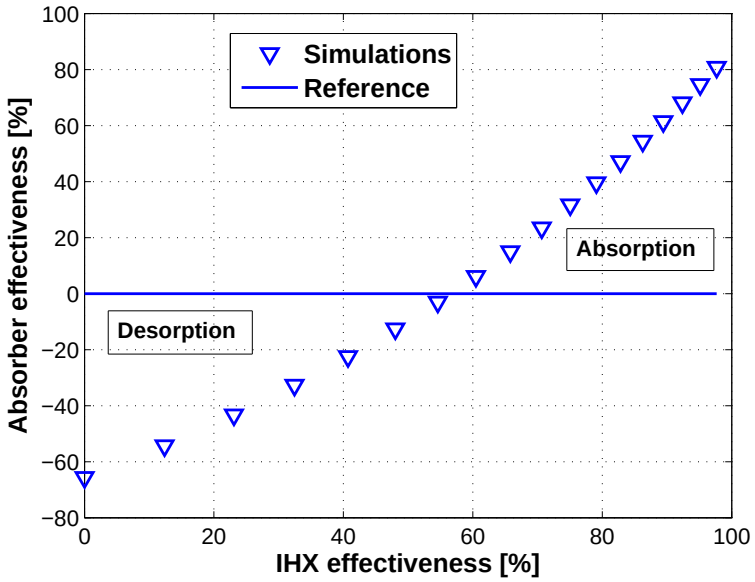

Figure 4.10: Absorber effectiveness versus IHX effectiveness. Absorption and desorption regions are depicted as a function of several IHX effectiveness and for the following absorber inlet conditions: $T_a^{in} = 2°C, RH_a^{in} = 90\%$ and $C_{ld}^{in} = 35\%$.

Chapter 5

Hydrodynamic analysis of a liquid desiccant film subjected to heat and mass transfer using the finite volume method.

The simultaneous phenomena of momentum, heat and mass transfer occurring between a liquid desiccant film and a flow of moist air in parallel-flow configuration, is studied numerically. The particular geometrical configuration of the narrow channels within an absorber and the difference of two orders of magnitude between the thickness of the liquid film and the air flow is treated by a hybrid discretization scheme with a staggered grid, using the finite volume method within a semi-implicit pressure-linked algorithm where temperature dependent properties are computed. The codes are validated against the well known Couette and Poiseuille flow solutions, and relevant literature heat and mass exchange problems showing good agreement. The influence of the heat and mass exchange is reflected in the calculation of the temperature profiles until thermal equilibrium is reached. The non-dimensional parameters Reynolds and Peclet numbers are computed using temperature dependent properties to characterize the flow. A reduction of approximately 25% in Reynolds number in the liquid film is observed, along the length of the channel. Peclet numbers greater than two are observed in the calculations, showing the necessity to use a hybrid scheme in the finite volume method to calculate the convective terms.

5.1 Introduction

The heat, mass, and momentum transfer equations are solved numerically for an incompressible, two dimensional, parallel flow of a humid air stream and a liquid desiccant film with temperature-dependent properties, by using the finite volume method. Heat and mass exchange analysis in liquid films considering prescribed velocity profiles or computing hydrodynamics for an isothermal fluid flow are common in literature [18, 20–23]. However, the combining effects of momentum, heat and mass transport are rarely treated [24, 25], even less for systems with temperature dependent properties [26, 27].
Comprehensive reviews about desiccants in cooling air conditioning systems and heat and mass transfer in falling-film absorption cases are presented by Daou et al. [34], and Killion and Garimella, respectively [74].

Also, nonvolatile and volatile absorbents are considered the main classification of the desiccants, within the laminar, wave and turbulent flow examples [75–78].

Additionally, examples neglecting or considering the influence of the mass transfer can be found in [79–81]. However, there are no direct examples of solving simultaneous heat, mass, and momentum transfer equations.
Modeling turbulent recirculating flows by finite-volume methods is reviewed by Leschziner in 1989 [82], where recirculation zones in common examples characterize advantages and disadvantages of the CFD codes at the time. Comparisons about the most common finite-volume-algorithms can be found in works from Zeng and Tao [83], and more recently in Walter [84]. The first work is a study of the convergence characteristics and robustness for four variants of the well known semi-implicit method for pressure-linked equations (SIMPLE) at fine grid (100×100 divisions approximately). Four examples are used as benchmark in the simulations, where the SIMPLEC algorithm is recommended for fine grid systems because of its robustness and computational time. The second work shows also four variations of the SIMPLE-algorithm, but instead of solving for the so called SIMPLEX (extrapolation), the PISO-algorithm is utilized. The simulations report that the SIMPLER-algorithm should be preferred for dynamic problems like the ones based on the tube-header-model.
The finite volume equations that solve the heat, mass and momentum transfer problem were obtained from the governing equations, and used in the iterative pressure correction method introduced during the 70's [24, 25, 85–87]. Improvements were introduced during the 80's [88–90]. Although the formulation can handle isothermal and non-isothermal systems, for simplicity isothermal systems are more common in the literature.

The aim of this chapter is to numerically model the couple momentum, mass, and energy conservation equations for a temperature dependent property two-fluid flow interaction between a liquid desiccant film and humid air by using the finite volume discretization method with a hybrid configuration, and the SIMPLE algorithm.

5.2 Description of the problem

Consider a liquid desiccant (LD) film flowing at a constant volumetric flow rate and with known inlet temperature and concentration and simultaneously, an inflow humid air with prescribed inlet velocity, temperature and concentration profiles, in a parallel configuration as it is shown in Figure 5.1. Both fluids are flowing in the positive x direction with horizontal velocities varying only along the $y-$axis. The rate of water vapor absorption is small and the solubility of air in the desiccant is negligible so the film thickness is considered constant at steady state. The flow is assumed to be smooth, implying that no wavy motion exists. The physical properties are considered as temperature dependent and a thermodynamic equilibrium is assumed at the interface.

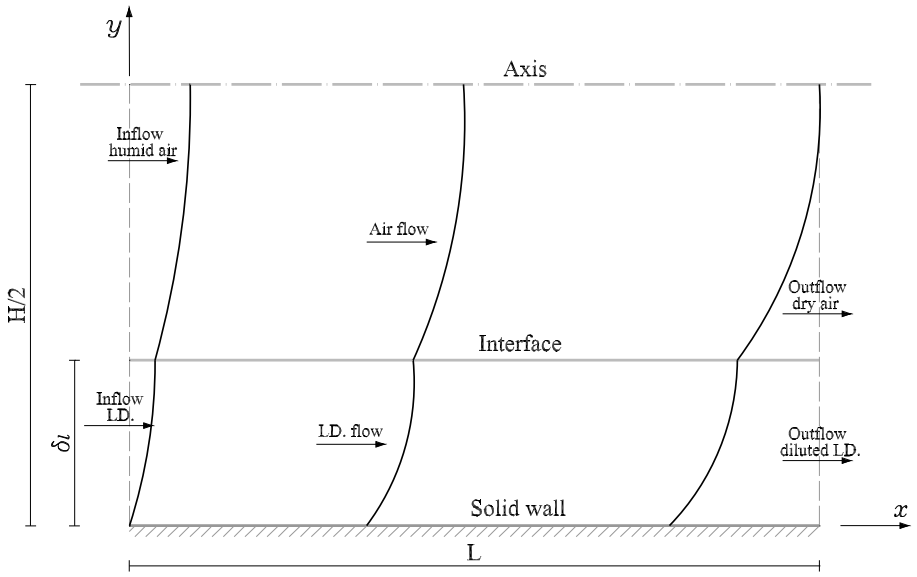

Figure 5.1: Schematic of the two fluid flow domain.

The general governing equations for both gas and liquid domains are conveniently formulated for the integration step in the finite volume method. Thus, the

steady-state conservation of mass and two dimensional momentum equations are described as follows:

$$\frac{\partial}{\partial x}(\rho u) + \frac{\partial}{\partial y}(\rho v) = 0, \tag{5.1}$$

$$\frac{\partial}{\partial x}(\rho u u) + \frac{\partial}{\partial y}(\rho v u) = \frac{\partial}{\partial x}\left(\mu \frac{\partial u}{\partial x}\right) + \frac{\partial}{\partial y}\left(\mu \frac{\partial u}{\partial y}\right) - \frac{\partial p}{\partial x}, \tag{5.2}$$

$$\frac{\partial}{\partial x}(\rho u v) + \frac{\partial}{\partial y}(\rho v v) = \frac{\partial}{\partial x}\left(\mu \frac{\partial v}{\partial x}\right) + \frac{\partial}{\partial y}\left(\mu \frac{\partial v}{\partial y}\right) - \frac{\partial p}{\partial y}, \tag{5.3}$$

with boundary conditions

$$y = 0;\ 0 \leqslant x \leqslant L;\ u = v = 0, \tag{5.4}$$

$$y = \delta_l;\ 0 \leqslant x \leqslant L;\ u_l = u_a;\ \tau_l = \tau_a, \tag{5.5}$$

$$y = \frac{H}{2};\ 0 \leqslant x \leqslant L;\ \frac{\partial u}{\partial y} = 0, \tag{5.6}$$

$$x = 0;\ 0 \leqslant y \leqslant \delta_l;\ u_l = U_l(y), \tag{5.7}$$

$$x = 0;\ \delta_l \leqslant y \leqslant \frac{H}{2};\ u_a = U_a(y), \tag{5.8}$$

$$x = L;\ 0 \leqslant y \leqslant \frac{H}{2};\ \frac{\partial u}{\partial x} = 0. \tag{5.9}$$

The governing energy and concentration equations are utilized in the following form:

$$\frac{\partial}{\partial x}(\rho u T) + \frac{\partial}{\partial y}(\rho v T) = \frac{\partial}{\partial x}\left(\frac{K}{Cp}\frac{\partial T}{\partial x}\right) + \frac{\partial}{\partial y}\left(\frac{K}{Cp}\frac{\partial T}{\partial y}\right), \tag{5.10}$$

$$\frac{\partial}{\partial x}(u(W,C)) + \frac{\partial}{\partial y}(v(W,C)) = \frac{\partial}{\partial x}\left(\mathcal{D}\frac{\partial (W,C)}{\partial x}\right) + \frac{\partial}{\partial y}\left(\mathcal{D}\frac{\partial (W,C)}{\partial y}\right), \tag{5.11}$$

with boundary conditions

$$x = 0;\ 0 \leqslant y \leqslant \delta_l;\ T = T_{l,i};\ W = W_i, \tag{5.12}$$

$$x = 0;\ \delta_l \leqslant y \leqslant \frac{H}{2};\ T = T_{a,i};\ C = C_i, \tag{5.13}$$

$$x = L;\ 0 \leqslant y \leqslant \frac{H}{2};\ \frac{\partial T}{\partial x} = 0;\ \frac{\partial (W, C)}{\partial x} = 0, \tag{5.14}$$

$$y = 0;\ 0 \leqslant x \leqslant L;\ \frac{\partial T}{\partial y} = 0;\ \frac{\partial W}{\partial y} = 0, \tag{5.15}$$

$$y = \delta_l;\ 0 \leqslant x \leqslant L; T_l = T_a;\ W = W_{int}, \tag{5.16}$$

$$y = \frac{H}{2};\ 0 \leqslant x \leqslant L;\ \frac{\partial T}{\partial y} = 0;\ \frac{\partial C}{\partial y} = 0, \tag{5.17}$$

where the interface concentration W_{int} is treated in the same way as in chapters 3 and 4, with Eq. (3.25) and Eq. (4.15) respectively:

$$W_{int} = 0.62185 \frac{p_v}{(p_t - p_v)}, \tag{5.18}$$

$$p_v = p_{v,H_2O}(1 - 0.828(1 - C) - 1.496(1 - C)^2 + (1 - C)\frac{(T_{int} - 40)}{350}). \tag{5.19}$$

The momentum, energy and mass balances at the liquid−air interface are considered as follows:

$$\mu_l \frac{\partial u_l}{\partial y_l} = \mu_a \frac{\partial u_a}{\partial y_a}. \tag{5.20}$$

$$-k_l \frac{\partial T_l}{\partial y_l} = k_a \frac{\partial T_a}{\partial y_a} + \rho_a \mathcal{D}_a h_{gf} \frac{\partial W}{\partial y_a}, \tag{5.21}$$

$$-\rho_l \mathcal{D}_l \frac{\partial C}{\partial y_l} = \rho_a \mathcal{D}_a \frac{\partial W}{\partial y_a}. \tag{5.22}$$

Additional details related with this boundary condition are presented in section 5.6.

5.3 Discretization method

The discretized governing equations utilizing the finite volume method (FVM) which is well suited for the numerical simulation of various types of conservation laws [91]. FVM has been extensively used in engineering fields such as fluid mechanics [90, 92, 93], and heat and mass transfer [75, 76, 94]. This method is based on integrals rather than derivatives. That is in fact, the main reason to setup the governing equations in the way that was shown above, where the differential equations were written in conservative form that allows to integrate those equations locally in each one of the control volumes. Moreover, the integral conservation law is enforced for small control volumes defined by the computational mesh (See Figures 5.2 and 5.3).
In order to avoid the well known checkerboard velocity distribution during the calculations [95], a standard staggered grid distribution of the control volumes is used as described in the next subsection.

5.3.1 Definition of control volumes

For the two-dimensional problem described above, three control volumes are considered to model velocity, pressure, temperature and concentration distributions. Two control volumes are exclusive for the x and y velocities respectively, and the third one is used to evaluated pressure nodes, temperature and concentration distributions. Figure 5.2 shows a general schematic of the above mentioned control volumes, where the variables i and j indicate the location in x and y coordinates of the nodes within the domain. Note that the general node (i, j) corresponds to the control-volume's center of pressure, temperature or concentration. Similarly, the node $(i, j + 1)$ tallies the center of $v-$velocity's control volume, meanwhile node $(i-1, j)$ shows the corresponding location for the center of $u-$velocity. Also, the relationship between control volumes is well defined in the figure, showing how neighbors act within the limits of the control volume, influencing the calculation of conservation laws.
In order to perform a spatial finite volume discretization of the governing equations, a mesh of the domain, over which the conservation laws are to be studied, is introduced in Figure 5.3. Control volumes are used in the entire domain. However, the control volumes at the boundaries are not shown in the figure.

5.3.2 Local control volumes

Using the general nomenclature for the location nodes can generate confusion at local level. To link the equations with their respective control volumes, a

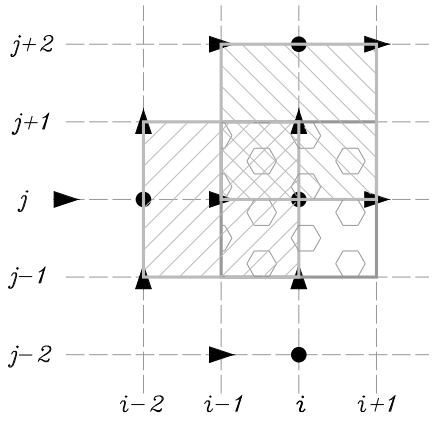

Figure 5.2: General scheme of control volume utilized in staggered discretization.

nomenclature for the location of nodes is used following the method proposed by Patankar and Spalding [24] and improved by Runchal [87]. Figures 5.4, 5.5 and 5.6 use capital letters to represent the location of: the control node P, and its north (N), south (S), east (E) and west (W) neighbors. Its own boundaries are denoted at north (n), south (s), east (e) and west (w).
For discretization of pressure, temperature and concentration, the scheme shown in Figure 5.4 was used, where the integration of the differential equations are performed using the boundaries of the control volume.

5.3.3 Discretization of the transport problem

A surface integration step of all the governing equations is required in the discretization process. For example, after the local integration of the governing equation Eq. (5.2) and using the nomenclature introduced in Fig. 5.5, we can define conservative fluxes $F_x = (\rho u)_x$ or $F_y = (\rho v)_y$, and the discretization of the $x-$momentum equation takes the form:

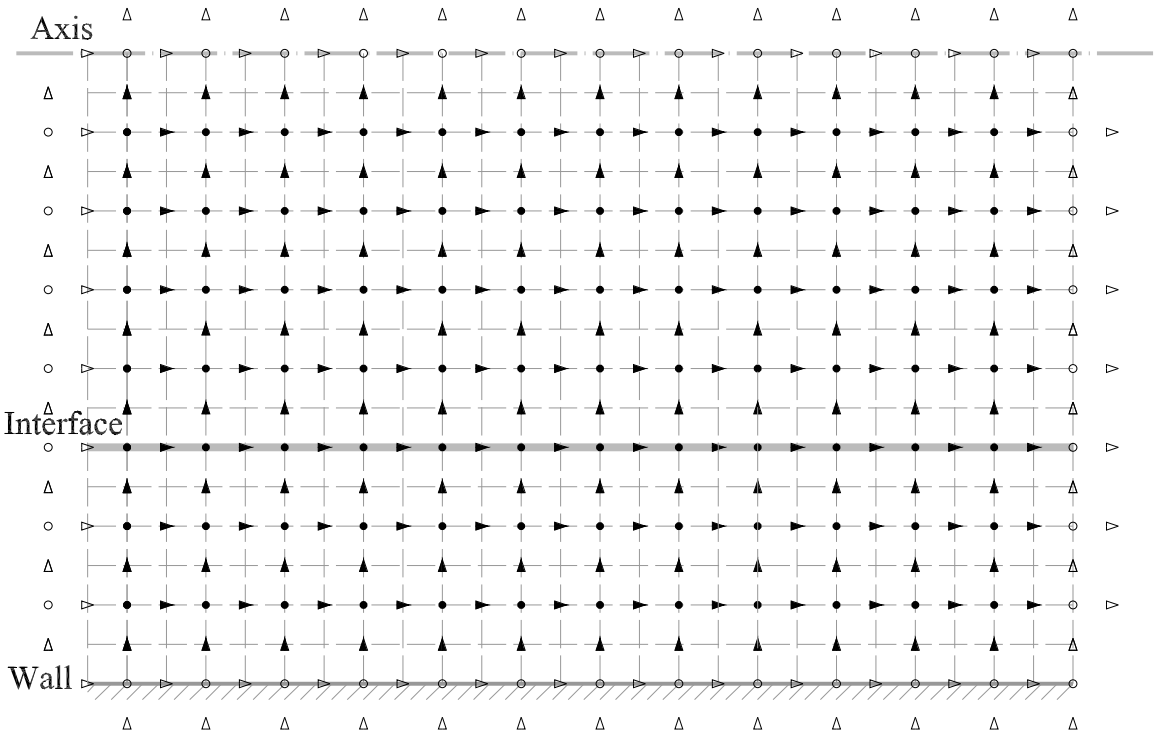

Figure 5.3: Schematic of the two fluids domain discretization.

$$(\rho u A u)_e - (\rho u A u)_w + (\rho v A u)_n - (\rho v A u)_s = \left(\mu A \frac{\partial u}{\partial x}\right)_e - \left(\mu A \frac{\partial u}{\partial x}\right)_w + \left(\mu A \frac{\partial u}{\partial y}\right)_n - \left(\mu A \frac{\partial u}{\partial y}\right)_s - (p_e - p_w) A_P, \quad (5.23)$$

$$(FA)_e u_e - (FA)_w u_w + (FA)_n u_n - (FA)_s u_s = \left(\frac{\mu A}{\Delta x}\right)_e (\Delta u)_e - \left(\frac{\mu A}{\Delta x}\right)_w (\Delta u)_w + \left(\frac{\mu A}{\Delta y}\right)_n (\Delta u)_n - \left(\frac{\mu A}{\Delta y}\right)_s (\Delta u)_s - (p_e - p_w) A_P, \quad (5.24)$$

$$(FAu)_e - (FAu)_w + (FAu)_n - (FAu)_s = (DA\Delta u)_e - (DA\Delta u)_w + (DA\Delta u)_n - (DA\Delta u)_s - (p_e - p_w) A_P, \quad (5.25)$$

where A is the cross sectional area at the considered control valume boundary, and the "D" coefficient takes care of the relationship between viscosity and the local geometry of the control volume.

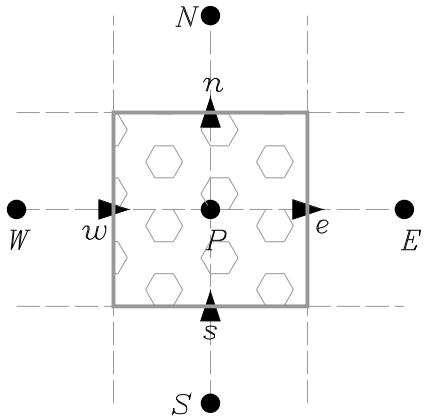

Figure 5.4: Schematic of the control volume utilized in the discretization of the pressure nodes.

For the $y-$momentum equation, Eq. (5.3), this step is similar. However, since nomenclature in Fig. 5.6 obeys to a staggered grid, the discretization pressure values are evaluated only at the north and south boundaries. Thus, $y-$momentum equation takes the form:

$$(\rho u A v)_e - (\rho u A v)_w + (\rho v A v)_n - (\rho v A v)_s = \left(\mu A \frac{\partial v}{\partial x}\right)_e - \left(\mu A \frac{\partial v}{\partial x}\right)_w + \left(\mu A \frac{\partial v}{\partial y}\right)_n - \left(\mu A \frac{\partial v}{\partial y}\right)_s - (p_n - p_s) A_P, \quad (5.26)$$

$$(FA)_e v_e - (FA)_w v_w + (FA)_n v_n - (FA)_s v_s = \left(\frac{\mu A}{\Delta x}\right)_e (\Delta v)_e - \left(\frac{\mu A}{\Delta x}\right)_w (\Delta v)_w + \left(\frac{\mu A}{\Delta y}\right)_n (\Delta v)_n - \left(\frac{\mu A}{\Delta y}\right)_s (\Delta v)_s - (p_n - p_s) A_P, \quad (5.27)$$

$$(FAv)_e - (FAv)_w + (FAv)_n - (FAv)_s = (DA\Delta v)_e - (DA\Delta v)_w + (DA\Delta v)_n - (DA\Delta v)_s - (p_n - p_s) A_P. \quad (5.28)$$

The energy and mass governing equations, Eq. (5.10) and Eq. (5.11) respectively, are integrated locally using the scheme shown in Figure 5.4. The energy governing equation takes the form:

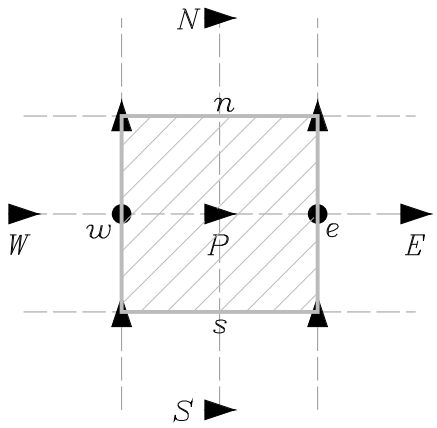

Figure 5.5: Scheme of the control volume of horizontal velocity utilized in the discretization.

$$(FAT)_e - (FAT)_w + (FAT)_n - (FAT)_s = \\ = (DA\Delta T)_e - (DA\Delta T)_w + (DA\Delta T)_n - (DA\Delta T)_s, \tag{5.29}$$

where the fluxes are defined also as $F_s = (\rho U)_s$, but the coefficient $D = \frac{K}{Cp\Delta s}$, and s represents the space in consideration. For the species conservation equation coefficients F and D change their definitions as $F = U$ and $D = \frac{\mathcal{D}}{\Delta s}$. The new governing species equation takes the form:

$$(FA(W,C))_e - (FA(W,C))_w + (FA(W,C))_n - (FA(W,C))_s = \\ (DA\Delta(W,C))_e - (DA\Delta(W,C))_w + (DA\Delta(W,C))_n - (DA\Delta(W,C))_s, \tag{5.30}$$

Within the integrated governing equations (5.25), (5.28), (5.29) and (5.30), the evaluation of the variables and coefficients at the borders of the control volume is critical. Sometimes there is not a direct value available and interpolation or special considerations are required. For instance, in the evaluation of the flux $F_w = (\rho u)_w$ within the control volume in Fig. 5.5, the density value has been stored at that specific location meanwhile the horizontal velocity is not. The value of the velocity is obtained from the average value $\frac{u_W + u_P}{2}$, where we consider that the influence of the two velocities is equal. The new governing equations can be represented by the general expression:

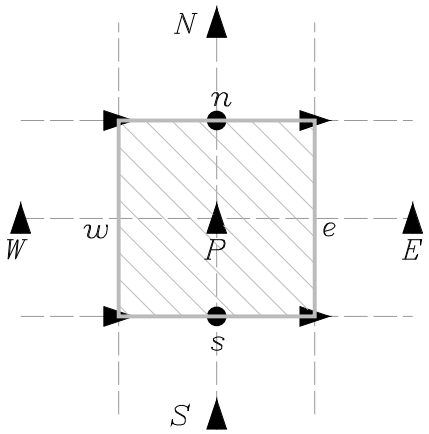

Figure 5.6: General scheme of the control volume utilized in the discretization of v_y.

$$(FA)_e\phi_e - (FA)_w\phi_w + (FA)_n\phi_n - (FA)_s\phi_s = (DA)_e(\phi_E - \phi_P)$$
$$-(DA)_w(\phi_P - \phi_W) + (DA)_n(\phi_N - \phi_P) - (DA)_s(\phi_P - \phi_S) + S_u, \qquad (5.31)$$

where ϕ represents the variable considered, which is well positioned on the diffusion terms but undefined for the convective boundaries, and S_u is the source term. The actual value can be evaluated depending on the influence of its neighbors which is represented by the differencing scheme.

5.3.4 Central, Upwind and Hybrid differencing schemes

In theory, numerical solutions of differential equations should match the analytical solution (if there is one) when an infinitely large mesh is used to discretize the domain. In a practical approach, a reasonable mesh is used, to ensure mesh-independence and convergence to a physical solution. In fact, choosing a convenient discretization scheme is crucial within problems that involve convection and diffusion forces. Discretization schemes like *Central* and *Upwind* are common in the solution of these problems, with pros and cons that are overcome by using a hybrid scheme. It is called *Hybrid* because it utilizes both central and upwind discretization schemes according to the particular need, as it will be shown below. If a second-order accurate *central* scheme is applied, the value of the velocity is obtained from the average value of the neighbors, meaning that the influence of the velocities is considered as equal. For instance: $\phi_w = \frac{1}{2}(\phi_W + \phi_P)$. The same

principle applies to all other boundaries and control volumes with the concern that we are no able to identify flow direction. Conversely, if an *upwind* scheme is utilized, which is first-order accurate: $\phi_w = \phi_W$ and $\phi_e = \phi_P$. This time the influence of one of the values is considered predominant and assumed to be the value at the boundary. In low Reynolds numbers problems or when the diffusion is important, the upwind or "donor cell" differencing scheme can lead to wrong solutions. Central and upwind differencing schemes respectively are applied to the Eq. 5.31 as presented below:

$$FA|_e \frac{\phi_E + \phi_P}{2} - FA|_w \frac{\phi_W + \phi_P}{2} + FA|_n \frac{\phi_N + \phi_P}{2} - FA|_s \frac{\phi_S + \phi_P}{2} = DA|_e (\phi_E - \phi_P) - DA|_w(\phi_P - \phi_W) + DA|_n(\phi_N - \phi_P) - DA|_s(\phi_P - \phi_S) + S_u, \quad (5.32)$$

$$FA|_e\phi_P - FA|_w\phi_W + FA|_n\phi_P - FA|_s\phi_S = DA|_e(\phi_E - \phi_P) - DA|_w(\phi_P - \phi_W) + DA|_n(\phi_N - \phi_P) - DA|_s(\phi_P - \phi_S) + S_u. \quad (5.33)$$

Rearranging terms for both equations above, we can obtain a more general expression:

$$a_p\phi_P = a_e\phi_E + a_w\phi_W + a_n\phi_N + a_s\phi_S + S_u, \quad (5.34)$$

$$or\ a_p\phi_P = \Sigma a_{nb}\phi_{nb} + S_u \quad (5.35)$$

where a coefficients will be defined depending on the scheme to be used. D.B. Spalding in 1972 [85] proposed a method to replace the upwind scheme however, it was Runchal [87] in the same year who settled it as *Hybrid* scheme, appearing to be the best solution for convection-diffusion problems like the one presented here. It combines the benefits of both options (central and upwind) and at the same time it solves the problems by using the analysis of the local Peclet number ($Pe = \frac{F}{D}$). In cases where $Pe < 2$, the viscous effects are more important than the convective ones, and in cases where $Pe \geq 2$, the convective part exerts a stronger influence. Thus, the coefficients for the hybrid-differencing scheme in a two-dimensional convection-diffusion problem can be written as follows:

$$a_e = A_e \times max\left[-F_e, \left(D_e - \frac{F_e}{2}\right), 0\right], \tag{5.36}$$

$$a_w = A_w \times max\left[F_w, \left(D_w + \frac{F_w}{2}\right), 0\right], \tag{5.37}$$

$$a_n = A_n \times max\left[-F_n, \left(D_n + \frac{F_n}{2}\right), 0\right], \tag{5.38}$$

$$a_s = A_s \times max\left[F_s, \left(D_s + \frac{F_s}{2}\right), 0\right], \tag{5.39}$$

$$a_p = a_e + a_w + a_n + a_s + \Delta F + S_p, \tag{5.40}$$

where the coefficient $\Delta F = F_e - F_w + F_n - F_s$, and the coefficient S_p appears to balance the boundary conditions.
Thus, the governing equations to be used at internal nodes of the discretization take the form:

$$x - m: \; a_p u_P = \Sigma a_{nb} u_{nb} - (p_e - p_w) A_P^y, \tag{5.41}$$

$$y - m: \; a_p v_P = \Sigma a_{nb} v_{nb} - (p_n - p_s) A_P^x, \tag{5.42}$$

$$c - energy: \; a_p T_P = \Sigma a_{nb} T_{nb}, \tag{5.43}$$

$$c - mass: \; a_p (W, C)_P = \Sigma a_{nb} (W, C)_{nb}. \tag{5.44}$$

5.4 Pressure correction

The numerical procedure presented in this chapter is based on a technique named "pressure correction" [91, 95]. The basic idea is to construct a new set of solutions from the results obtained in the previous iteration. Thus, the guess values of pressure p^* are used to calculate new approximations of velocities u^* and $v*$. Then, using the continuity equation, we compute a set of pressure correction p' values to obtain the new value of pressure

$$p = p^* + p'. \tag{5.45}$$

Similarly, we can define corrections for velocities as follows:

$$u = u^* + u', \tag{5.46}$$
$$v = v^* + v'. \tag{5.47}$$

From the new form of the governing equations (5.41) and (5.42) we can construct

$$x - m: \; a_p u_P^* = \Sigma a_{nb} u_{nb}^* - (p_e^* - p_w^*) A_P^y, \tag{5.48}$$
$$y - m: \; a_p v_P^* = \Sigma a_{nb} v_{nb}^* - (p_n^* - p_s^*) A_P^x, \tag{5.49}$$

where super-indices "*" represent initial guess or not corrected values. Subtracting equations (5.48) and (5.49) from (5.41) and (5.42) respectively, and using the expressions from equations (5.45), (5.46) and (5.47), we obtain:

$$x - m: \; a_p u_P' = \Sigma a_{nb} u_{nb}' - (p_e' - p_w') A_P^y, \tag{5.50}$$
$$y - m: \; a_p v_P' = \Sigma a_{nb} v_{nb}' - (p_n' - p_s') A_P^x. \tag{5.51}$$

The first term on the right hand side of the above equations is manipulated depending on what algorithm in the Simple family is used (SIMPLE, SIMPLER or SIMPLEC). In general, we end up with expressions for corrected velocities as follows:

$$u_P = u_P^* + d_p^x (p_e' - p_w'), \tag{5.52}$$
$$v_P = v_P^* + d_p^y (p_n' - p_s'), \tag{5.53}$$

where coefficients $d_p^{(x,y)}$ are equal to $\frac{A^{(x,y)}}{a_p}$ in each direction. Now, substituting this expressions in the integrated conservation equation Eq. (5.1)

$$(\rho u A)_e - (\rho u A)_w + (\rho v A)_n - (\rho v A)_s = 0, \tag{5.54}$$

and after some algebraic manipulations we get the discretization expression for pressure correction at internal node as follows:

$$a_p p' = a_e p' + a_w p' + a_n p' + a_s p' + b_p, \tag{5.55}$$

where the coefficients are:

$$a_e = (\rho dA)_e \,, \tag{5.56}$$
$$a_w = (\rho dA)_w \,, \tag{5.57}$$
$$a_n = (\rho dA)_n \,, \tag{5.58}$$
$$a_s = (\rho dA)_s \,, \tag{5.59}$$
$$a_p = a_e + a_w + a_n + a_s, \tag{5.60}$$
$$b_p = (\rho u^* A)_w - (\rho u^* A)_e + (\rho v^* A)_s - (\rho v^* A)_n \,. \tag{5.61}$$

5.5 Considerations for the boundary conditions

Knowing that the boundary conditions specifically define the problem, it is vital to define the right conditions corresponding to this two-fluids approach. The most challenging part is to deal with the staggered grid arrangement which forces us to use additional control volumes around the physical domain as is shown in Fig. 5.3, where filled arrows and circles are considered as internal nodes and the hollow symbols are either boundary or additional nodes. The calculations are performed for the internal nodes, but not for additional and boundary nodes. Also, an special one-dimensional case is used for the internal interface.

5.5.1 Inlet Boundary

Considering two inlet streams with uniform temperature and concentration values in each sub-domain, the inlet values are saved in the additional nodes shown at the left hand side of Fig. 5.7, sectors I to V. The node at the interface is not used for temperature or concentration calculations, however it is utilized to store the recalculated interfacial inlet pressure. Similarly, the prescribed inlet velocity profile values are stored in the hollow arrows and the flow direction is assumed to be mainly from left to right. Although the inlet vertical velocity and pressure are located outside of the domain a distance of $\delta x/2$, all the conservation fluxes remain satisfied.

5.5.2 Wall boundary

The wall at the bottom is treated as a solid body with no-slip condition for the momentum equations, and as an insulated wall for the energy and mass transport equations as it was presented in boundary conditions Eq. (5.4) and (5.15). The normal component of the velocity is set to be zero and is stored in the additional set

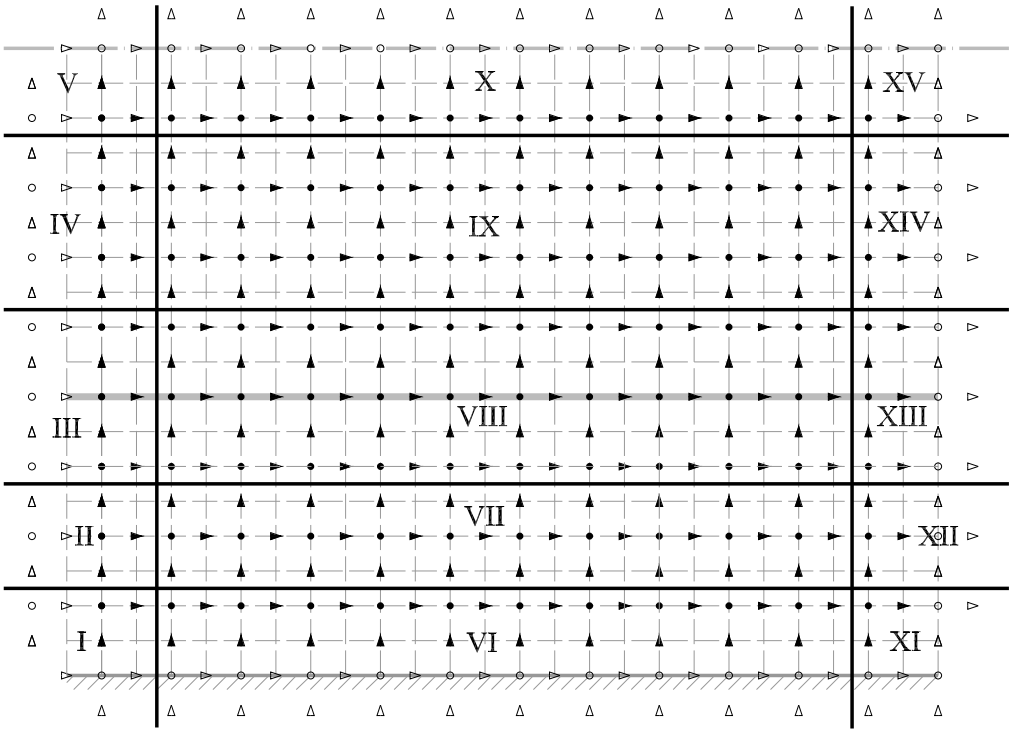

Figure 5.7: Schematic of the sectors in the two fluids domain.

of arrows under the surface. However, the distance considered for the calculations is $\delta y/2$. For all other variables the location is at the surface. Since the horizontal velocities are known, performing the pressure correction is unnecessary for this nodes. The sectors which have to use these formulations are I, VI and XI.

5.5.3 Axisymmetric boundary

The problem analysed here is axisymmetric represented by the boundary in Fig. 5.3. The change of the velocities with respect to y is taken to be zero. Although the velocities in this boundary in sectors V, X and XV, are symbolized with hollow arrows, the stored values are recalculated in each iteration. However, pressure correction is unnecessary once more. The energy and mass governing equations are treated obeying the boundary conditions in Eq. (5.17).

5.5.4 Outlet Boundary

The outlet boundary condition plays an stabilizing role since we assume atmospheric pressure at the boundary as shown in Fig. 5.7 sectors XI to XV. In this case we can assume that the location of this outlet is far enough from the inlet disturbances and the flow has reached fully developed condition. Thus, the gradients of all variables except pressure are considered zero in the x direction as described in the boundary condition given by Eq. (5.9) and Eq. (5.14).

5.6 Interface momentum, energy and species balances

In this section, special considerations are presented, since the interface between the two fluids is the critical aspect to be addressed. Initially, details about the momentum shear stress are described since this is the driving force exerted from the air to the liquid film. An equation that relates the interfacial horizontal velocity with the closest grid nodes is set from the boundary condition in Eq. (5.5) as follows:

$$u_{int} = \left(\frac{\mu_l}{\delta y_l} + \frac{\mu_a}{\delta y_a}\right)^{-1} \times \left[\frac{\mu_l}{\delta y_l} u_l + \frac{\mu_a}{\delta y_a} u_a\right] = 0, \tag{5.62}$$

where δy_a and δy_l are discretization values from the respective air and liquid domains, which in this configuration do not have the same values necessarily.
From equation (5.21), we can compute new values of the interfacial temperature as shown in the following equation:

$$T_{int} = \left(\frac{k_a}{\delta y_a} - \frac{k_l}{\delta y_l}\right)^{-1} \times \left[\frac{k_a}{\delta y_a} T_a - \frac{k_l}{\delta y_l} T_l + \frac{\rho_a \mathcal{D}_a h_{gf}}{\delta y_a} \left(W_a - W_{int}\right)\right]. \tag{5.63}$$

Similarly, from Eq. (5.22) the reference concentration value for liquid at the interface is recalculated from the expression:

$$C_{int} = C_a - \left(\frac{\rho_l \mathcal{D}_l}{\delta y_l}\right)^{-1} \times \frac{\rho_a \mathcal{D}_a}{\delta y_a} \left(W_a - W_{int}\right). \tag{5.64}$$

The above expressions are one-dimensional relations that are obtained from the calculated values. They provide the conditions at the interface for the next iteration.

5.7 Summary of the numerical procedure

To solve the problem introduced in this chapter a Semi-Implicit Method for Pressure-Linked Equations SIMPLE method is used together with an staggered grid mesh. The procedure developed by Patankar and Spalding [24] allows to apply efectivelly the staggered grid discretization presented above together with the pressure correction formula from momentum equations. The specific procedure is as follows:

(a) Set all initial and guess values (u^*, v^*, p^*, T^*, W^* and C^*) in their respective locations.

(b) Calculate temperature-dependent properties ρ, μ, k, Cp and $\mathcal{D}$, for both domains.

(c) Compute the discretized momentum equations at all internal grid nodes by using the actual pressure value p^*.

(d) Substitute the new velocity values, solve for p' in the pressure correction equation.

(e) Correct pressure by substituting p^* and p' into $p^{new} = p^* + \alpha p'$. An underrelaxation value α is used to ensure convergence.

(f) The pressure correction p' obtained is also used to correct velocity values in each domain.

(g) Using new velocities and pressure values, solve for energy and mass transport equations.

(h) Evaluate if convergence was achieved. In a positive case the process stop here and the results are plotted.

(i) If convergence was not achieved, new values for u^*, v^*, p^*, T^*, W^* and C^* are obtained from the above calculations.

(j) New temperature-dependance properties are compute before repeating step (c).

5.8 Results

A schematic of the problem was presented in the description of the problem in Figure 5.1. Inlet conditions are taken from the previous chapters in order to characterize the distribution of some of the properties in the liquid domain. Maximum, minimum and average property values within the domains are presented in Table 5.1. For the air domain only the average values are presented because no significant changes were observed for the range of temperatures tested.

Table 5.1: Liquid and air properties values obtained within the simulations.

Property	**Units**	**Liquid**			**Air**
		Max	Min	Avg	Avg
Density (rho)	(kg m^{-3})	1394.5	1384.4	1388	1.172
Dynamic Viscosiity (μ)	(kg m^{-1} s^{-1})	9.1e-3	6.4e-3	8.5e-3	1.83e-5
Thermal conductivity (k)	(W m^{-1} K^{-1})	0.5556	0.5301	0.5322	0.02635
Heat capacity (Cp)	(J kg^{-1} K^{-1})	2439.8	2347.1	2369.7	1028
Mass Diffusivity ($\mathcal{D}$)	(m^2 s^{-1})	9.56e-9	6.46e-9	7.15e-9	2.5e-5

Figures 5.8 and 5.9 show the average values of some properties along and across the liquid film respectively. As expected, in Fig. 5.8 strong changes are presented at the entrance of the channel due to the inlet absorption capacity of the liquid desiccant, and towards the end of the channel the values show an asymptotic behavior due to the saturation of the solution. The behavior across the liquid film is well characterized in Fig. 5.9 where zero represents the location of wall and the interface is located at δ_l. Some properties like heat capacity, viscosity and diffusivity are asymptotic at the wall meanwhile thermal conductivity shows a linear behavior across the channel. Clearly, the existence of an interface is the driving force that affects the change in the properties.

The interface between the two streams is associated with the energy and mass balances between the two domains. Average values of temperatures along the channel are depicted in Fig. 5.10. Temperature values from the temperature-dependent properties model are compared against the constant properties model from Rahamah which is used as a benchmark [23]. Solid lines are used to represent the constant properties model meanwhile dashed lines represent the results from

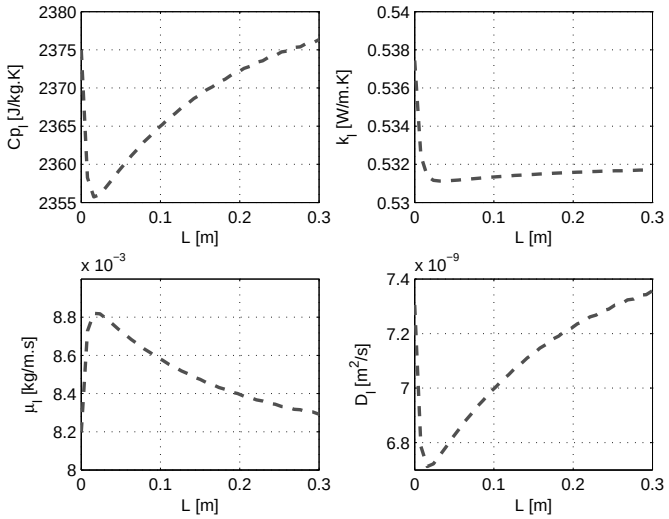

Figure 5.8: Average liquid properties heat capacity, thermal conductivity, dynamic viscosity and mass diffusivity along the channel.

the temperature-dependent model. Liquid and air average temperatures show good agreement along most of the channel length, however, discrepancies are found at the entrance of the channel.

Figures 5.11 and 5.12 show the comparisons for average water concentration along the channel for the air and liquid domain, respectively. At the air domain, the average concentrations of water match the benchmark. However, the values are slightly below Rahamah's results. Conversely, although water concentration in the liquid domain show a similar trend, significant changes are evident, due mainly to dependence of the diffusion coefficient on temperature. The results show a lower initial concentration for the temperature dependent case compared with the constant properties case. On the other hand, the liquid concentration at the end of the channel is higher for temperature dependent properties.

Finally, two non-dimensional parameters, Reynolds and Peclet numbers, are computed along the channel to characterize the change in property values of the liquid. Figure 5.13 shows the calculated local-Reynolds number along the channel for the temperature-dependent model, where average velocity and property values across the liquid film are used for the computations. A significant change in Reynolds number occurs at the inlet of the channel and eventually gets an asymptotic behavior for saturated liquid conditions. Even though the value of the Reynolds number are low, the average change represent approximately 25% of the inlet

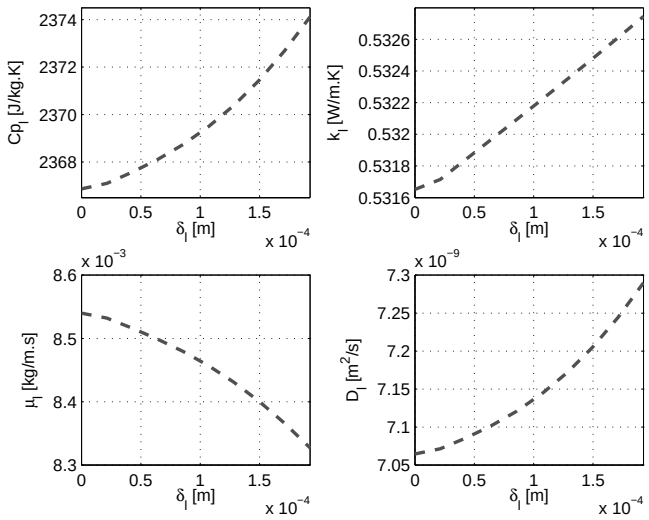

Figure 5.9: Average liquid properties heat capacity, thermal conductivity, dynamic viscosity and mass diffusivity across the channel.

Reynolds number. Moreover, figure 5.14 show the local relationship between the convective and viscous forces associated with the Peclet number along the channel. Asymptotic behavior is shown at both, the inlet and the outlet of the channel at different distances from the wall. The change in the value of Peclet number justifies the hybrid formulation of the finite volume method utilized in this work.

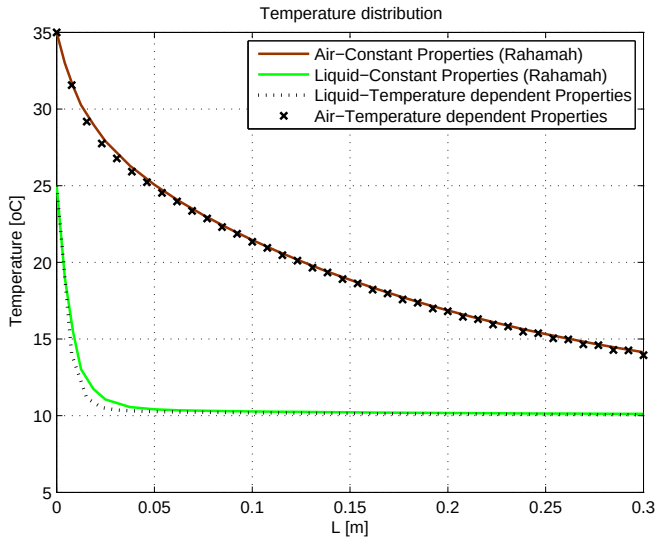

Figure 5.10: Average temperature distribution along the channel for both liquid and gas domains.

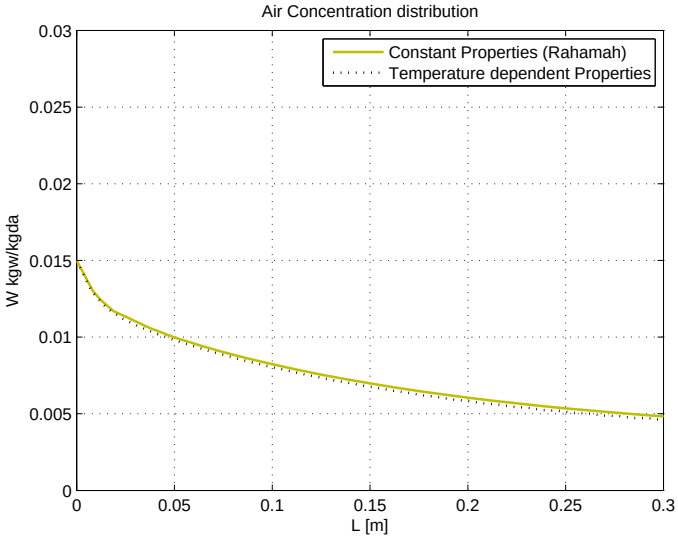

Figure 5.11: Average water concentration along the channel at the air domain.

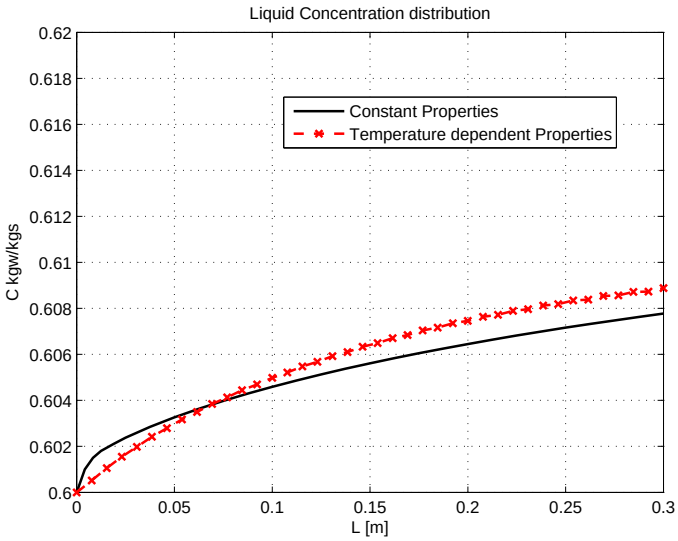

Figure 5.12: Average water concentration along the channel at the liquid domain.

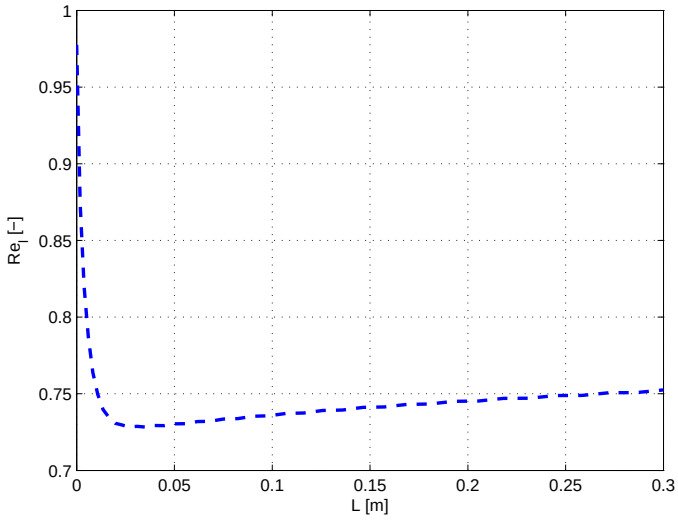

Figure 5.13: Local Reynolds number along the channel within the liquid domain.

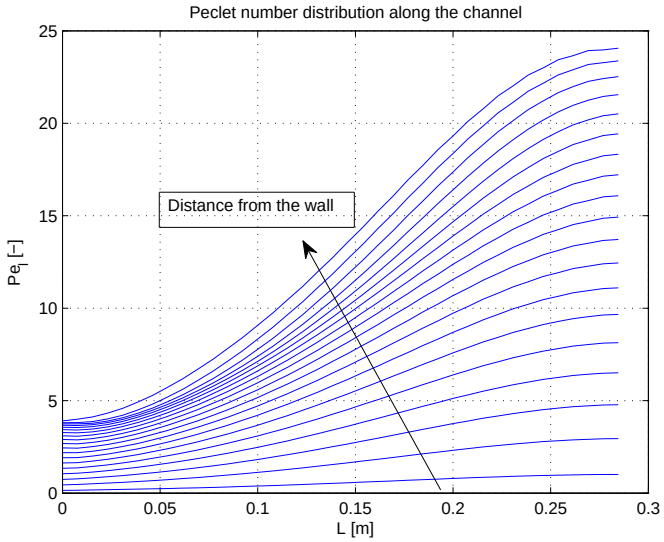

Figure 5.14: Local Peclet number distribution within the liquid domain.

5.9 Conclusions

A numerical approximation to solve hydrodynamics coupled with heat and mass transfer in two dimensional parallel flow of humid air stream and liquid desiccant film with temperature dependent properties, it is analyzed by using finite volume method within a SIMPLE algorithm. Since the properties values were stored at the same node where temperature and water concentrations were computed, the average values across the channel can be compared at the same nodes. However, the velocities and fluxes are computed accordingly with the staggered grid. Thus, a structured mesh was used and tested with uniform and variable distribution along and across the domain. It was shown to be mesh independent for the convenient vertical distribution of 40 divisions in liquid domain and 80 divisions in the gas domain and 100 divisions horizontally with 1.07 distribution factor.

A significant change in local Reynolds number is observed along the channel within the liquid domain, representing approximately 25% of the inlet Reynolds number. The obtained values of Peclet number in the liquid domain justify the hybrid formulation of the finite volume method utilized.

Chapter 6

Hydrodynamic stability of a liquid desiccant film due to momentum, heat and mass transport with a humid air stream

The stability of a liquid desiccant film within a heat and mass exchanger is analyzed not only from the momentum transport point of view but also considering the influence of thermo-physical properties variation due to heat and mass transport, in a parallel two-phase flow configuration. Two approaches were taken using the well known small disturbance stability analysis technique: a) by means of small wavenumber technique and b) by means of a computational model using complete orthonormalization technique, with variable fluid properties across and along the channel. This study shows that the liquid desiccant film is unstable for most of the tested Reynolds numbers and wave numbers close to one, however, particular configurations of density, viscosity and domain thickness ratios between the two fluids, and the consideration of temperature-dependent properties, have a stabilizing effect. Thus, for density ratios smaller than 250, wavenumbers up to one can be found to include the neutral stability curve; Viscosity ratios have a linear relationship with the wavenumber. Moreover, thickness ratios have opposite asymptotic behavior depending on the the reference length. Finally, the absorption process shows a stabilization effect along the channel. However instabilities appear for extremely small domain thickness ratios, even for low values of Reynolds number.

6.1 Introduction

A simplified liquid desiccant absorber (two-dimensional, parallel flow) is studied in order to analyze the hydrodynamic stability within the liquid desiccant film. Previous chapters have dealt with the heat and mass exchange between a liquid desiccant and humid air, however the gas-liquid interface was considered unperturbed. In this chapter, the liquid desiccant film and the humid-air stream interact with each other due to viscous effects which may be analyzed in a two dimensional approximation for laminar flow. The stability analysis of this laminar flow interaction is obtained not only by solving the traditional Orr-Sommerfeld (O-S) problem for a finite value of the Reynolds number above which instability occurs, but also by solving numerically the perturbed equations by the method of complete orthonormalization.

Several books and reviews have been written about hydrodynamic stability problems which have been recognized and formulated, both theoretically and experimentally since the nineteenth century [6, 96–98]. Hermann von Helmholtz in 1868 developed an experiment of wind blowing on an air-water interface. Three years later in 1871, Lord Kelvin solved mathematically the Helmholtz problem [12]. The Belgian physicist Joseph Plateau (1801-1883) was the first to study the instability of cylindrical films, understanding that the instability of these films is driven by the liquid surface tension [99]. Recent studies had shown that gravity driven cylindrical films are unstable even for low Reynolds numbers [100]. Plateau's work was revised and extended by Lord Rayleigh who showed that the instability of cylindrical films is established with a well-defined wavelength [101]. He predicted the existence of the surface waves, known as Rayleigh waves, and formulated a theorem on the role of inflexion points in velocity profiles. However, the most clear stability experiment at that time was conduced by Osborne Reynolds who showed that a laminar flow breaks down within circular pipes when flow parameters cause a critical value condition [102]. This critical parameter is the limit of transition from laminar to turbulent flow and it was calculated based on the average velocity, the kinematic viscosity of the fluid, and the pipe diameter.

Early in the twentieth century, William McFadden Orr [103] and Arnold Sommerfeld [104] named that critical parameter the Reynolds number and also derived the equations for the analysis of small disturbance in viscous parallel flows. But it was Walter Tollmien [105] who was able to solve the Orr-Sommerfeld problem using the Blasius flow profile and calculating the neutral curve which characterizes instabilities in the flow for certain Reynolds numbers. The traditional solution of the Orr-Sommerfeld problem with one dimensional basic flow and two dimensional perturbation behavior has the form $\phi(y)\exp^{i(\alpha x-\omega t)}$, where the basic flow ϕ

changes in y direction only, α is the wave number, and ω is the growth rate parameter calculated by Schlichting in 1933 [106]. In the same year, Squire showed that a three dimensional perturbed approximation with the form $\phi(y)\exp^{i(\alpha x+\beta z-\omega t)}$ can be treated as the two dimensional problem described above at lower Reynolds number.

Schematic examples of stability are presented by White [12], where a ball lies at rest under various conditions. First, the ball is considered in a concave recipient where its position is considered unconditionally stable, because it would always return to its initial position. A second example is the ball at the top of a convex surface showing an unstable state, since any slight disturbance would topple the ball, never to return. A third example shows a flat surface with a resting ball. This is considered neutral stability, since the ball will rest anywhere it is displaced. The final example illustrates the more complicated case, where the ball is stable for small disturbances but will diverge if disturbed far enough to drop over the edge. The last example is often the case for the interaction of two fluids where the leading fluid can cause a finite perturbation and instability to a laminar liquid flow [107]. The stability analysis does not predict turbulence but gives the knowledge for the start of the transition [108].

The interface instabilities between two fluids have also been studied. For example, the Kelvin-Helmholtz instability reads: "The interface between two fluids is unstable if there is a jump in the tangential component of the velocity across the interface" [109]. The shear flows Rayleigh-Taylor instability between two fluids of different densities concludes: "if the heavy fluid pushes the light fluid, the interface is stable. If the light fluid pushes the heavy fluid, the interface is unstable" [110]. Thus, the interacting fluids properties and the perturbation amplification at the interface will lead the stability analysis [111]. Significant studies that deal with instabilities in liquid desiccant films with temperature dependent properties have not been found in the literature.

In this chapter, the procedure for small disturbance is introduced as the central structure for stability analysis of one-phase and two-phase flows. The derivations of the disturbance differential equations that govern the problem are shown for both cases, including several forms of the simplified O-S relation. Various methodologies to dealt with the governing equations are taken. However, two of them are chosen to solve the effects of the heat and mass transport such as the small wavenumber technique and the complete orthonormalization technique. The small wavenumber technique is suitable for one and two-phase flows with average property profiles, but here it is used to solve the two-phase flow stability problem, after the effect of the heat and mass transfer have been used to compute hydrodynamic profiles. The complete orthonormalization technique is also able to solve one and

two-phase flows, but with the advantage to include directly the distribution of the properties in the colocation points. Finally, using operational values for a liquid desiccant film and humid-air stream from previous chapters, stability cases are tested in order to understand the behavior of the two-phase interaction when heat and mass transfer are included.

6.2 Small disturbance stability analysis procedure

The general procedure for small-disturbance stability analysis is explained in detail in the literature such as in Drazin and Reid [96] or in the book by White [12] which is the basis for this section. The procedure follows the following steps:

(a) Setup the basic governing equations to the physical problem.

(b) Add a disturbance variable and substitute into the basic equations that govern the problem.

(c) From the equations resulting from the step above, subtract the basic non-disturbed terms in order to obtain the disturbance equation.

(d) Linearize the disturbance equation by assuming small amplitudes and neglect higher order terms.

(e) If the linearized disturbance equation is complicated and multidimensional, it can be simplified by assuming a form for the disturbances, for instance, in only one direction.

(f) The linearized disturbance equation should be homogeneous and have homogeneous boundary conditions. This is an eigenvalue problem.

(g) The eigenvalues found in the step above are examined to determine the stability region and the neutral curve.

6.3 Stability formulation considering the liquid desiccant domain only (one-phase flow)

The classical stability formulation and the derivation of the traditional Orr-Sommerfeld equation are presented together with their solution for plane profiles

of Poiseuille and Blasius boundary layer flows. Results from numerical models are compared with published literature data. The purpose of this section is to validate the methodology that will be used in the next sections to analyze heat and mass transfer effects on the stability of the liquid desiccant film. Consider a homogeneous three dimensional infinite domain with a traditional coordinate system where the y coordinate is perpendicular to the main flow in the x direction.

6.3.1 Derivation of the governing equation

The famous derivation of the Orr-Sommerfeld equation was developed independently by William McFadden Orr and Arnold Sommerfeld at the beginning of the 20th century. In fluid dynamics, O-S is an eigenvalue problem itself which describes linear two-dimensional disturbance modes in parallel viscous flows. It is included here for purposes of completeness only and it follows the steps described in Section 6.2.

(a) Setup of the governing equations for the physical problem.

Assuming incompressible laminar flow with constant properties (density ρ, dynamic viscosity μ, thermal conductivity k and heat capacity c_p) and no buoyancy effects, the governing equations include continuity and momentum transfer:

$$\nabla \cdot \mathbf{V} = 0, \tag{6.1}$$

$$\frac{D\mathbf{V}}{Dt} = -\frac{1}{\rho}\nabla p + \nu \nabla^2 \mathbf{V}. \tag{6.2}$$

Suitable boundary conditions help to find velocity ($\mathbf{V}_o(\mathbf{x}, t) = (U, V, W)$) and pressure ($p_o(\mathbf{x}, t)$) profiles.

(b) Add a disturbance and substitute it into the basic equation.

Small-disturbance variables $\hat{\mathbf{v}}(\mathbf{x}, t) = (\hat{u}, \hat{v}, \hat{w})$ and $\hat{p}(\mathbf{x}, t)$ are added to the basic flow variables in the governing equations as follows. Replacing $\mathbf{V}$ by $\mathbf{V}_o + \hat{\mathbf{v}}$ and p by $p_o + \hat{p}$.

$$\nabla \cdot (\mathbf{V_o} + \hat{\mathbf{v}}) = 0, \tag{6.3}$$

$$\frac{D(\mathbf{V_o} + \hat{\mathbf{v}})}{Dt} = -\frac{1}{\rho}\nabla(p_o + \hat{p}) + \nu \nabla^2 (\mathbf{V_o} + \hat{\mathbf{v}}). \tag{6.4}$$

(c) Find the disturbance equations and (d) Linearize.

From the equations resulting from the step above, subtract the original profiles $\mathbf{V}_o$ and p_o terms in order to obtain the disturbance equation. Linearize the disturbance equation by assuming small disturbances neglecting higher order terms and products of velocities.

$$\frac{\partial \hat{u}}{\partial x} + \frac{\partial \hat{v}}{\partial y} + \frac{\partial \hat{w}}{\partial z} = 0, \tag{6.5}$$

$$\frac{\partial \hat{u}}{\partial t} + U\frac{\partial \hat{u}}{\partial x} + \hat{u}\frac{\partial U}{\partial x} + V\frac{\partial \hat{u}}{\partial y} + \hat{v}\frac{\partial U}{\partial y} + W\frac{\partial \hat{u}}{\partial z} + \hat{w}\frac{\partial U}{\partial z} \approx -\frac{1}{\rho}\frac{\partial \hat{p}}{\partial x} + \nu\nabla^2\hat{u}, \tag{6.6}$$

$$\frac{\partial \hat{v}}{\partial t} + U\frac{\partial \hat{v}}{\partial x} + \hat{u}\frac{\partial V}{\partial x} + V\frac{\partial \hat{v}}{\partial y} + \hat{v}\frac{\partial V}{\partial y} + W\frac{\partial \hat{v}}{\partial z} + \hat{w}\frac{\partial V}{\partial z} \approx -\frac{1}{\rho}\frac{\partial \hat{p}}{\partial y} + \nu\nabla^2\hat{v}, \tag{6.7}$$

$$\frac{\partial \hat{w}}{\partial t} + U\frac{\partial \hat{w}}{\partial x} + \hat{u}\frac{\partial W}{\partial x} + V\frac{\partial \hat{w}}{\partial y} + \hat{v}\frac{\partial W}{\partial y} + W\frac{\partial \hat{w}}{\partial z} + \hat{w}\frac{\partial W}{\partial z} \approx -\frac{1}{\rho}\frac{\partial \hat{p}}{\partial z} + \nu\nabla^2\hat{w}. \tag{6.8}$$

The solution of these linear partial differential equations for the perturbation variables $(\hat{u}, \hat{v}, \hat{w})$, where the velocities profiles (U, V, W) are already known, can be found by applying numerical methods.

(e) Simplify equations by assuming a form for the disturbances.

Systematically, the above equations can be simplified to a single differential equation by assuming a form for the disturbances as parallel basic flow. In that case, the V velocity is considered negligible, U and W, function only of y, and the most general form of the disturbance is that of a traveling wave (Tollmien-Schlichting waves) as follows:

$$\hat{\mathbf{v}} = \mathbf{v}(y)\exp[i\alpha(x\cos\theta + z\sin\theta - ct)], \tag{6.9}$$

$$\hat{p} = p(y)\exp[i\alpha(x\cos\theta + z\sin\theta - ct)], \tag{6.10}$$

where $\mathbf{v}(y)$ and $p(y)$ are the wave amplitude which varies with y only and moves in x direction at an angle θ. Additionally, $i = \sqrt{-1}$, α is the wave number of the disturbance and c is the propagation speed. Substituting this equations in the simplified equations in the step above, we obtain:

$$i\alpha u\cos\theta + \frac{dv}{dy} + i\alpha w\sin\theta = 0, \tag{6.11}$$

$$i\alpha u(U\cos\theta + W\sin\theta - c) + \frac{dU}{dy}v = -\frac{i}{\rho}\alpha p\cos\theta + \nu(\frac{d^2u}{dy^2} - \alpha^2 u), \tag{6.12}$$

$$i\alpha v(U\cos\theta + W\sin\theta - c) = -\frac{1}{\rho}\frac{dp}{dy} + \nu(\frac{d^2v}{dy^2} - \alpha^2 v), \tag{6.13}$$

$$i\alpha w(U\cos\theta + W\sin\theta - c) + \frac{dW}{dy}v = -\frac{i}{\rho}\alpha p\sin\theta + \nu(\frac{d^2w}{dy^2} - \alpha^2 w). \tag{6.14}$$

Introducing the compact notation

$$u_o = u\cos\theta + w\sin\theta, \tag{6.15}$$

$$U_o = U\cos\theta + W\sin\theta, \tag{6.16}$$

and multiplying the equation (6.12) by $\cos\theta$ and equation (6.14) by $\sin\theta$ add them together, and substituting with the compact notation, we reduce the system to three equations:

$$i\alpha u_o + \frac{dv}{dy} = 0, \tag{6.17}$$

$$i\alpha u_o(U_o - c) + \frac{dU_o}{dy}v = -\frac{i}{\rho}\alpha p + \nu(\frac{d^2u_o}{dy^2} - \alpha^2 u_o), \tag{6.18}$$

$$i\alpha v(U_o - c) = -\frac{1}{\rho}\frac{dp}{dy} + \nu(\frac{d^2v}{dy^2} - \alpha^2 v), \tag{6.19}$$

(f) The eigenvalue problem.

If we assume a total two dimensional problem by considering the W velocity as zero, we can simplify the notation by dropping the subscrips "$_o$", or by applying Squire's theorem: "For a two-dimensional parallel flow $U(y)$, the minimum critical unstable Reynolds number occurs for a two-dimensional disturbance propagating in the same direction ($\phi = 0$)". Eliminating algebraically u and p and using primes to denote differentiation with respect to y, results in the traditional Orr-Sommerfeld equation that in this case is written in dimensional form:

$$(U - c)(v' - \alpha^2 v) - U''v + \frac{i\nu}{\alpha}(v'''' - 2\alpha^2 v'' + \alpha^4 v) = 0. \tag{6.20}$$

This is a fourth-order linear homogenous differential equation for which boundary conditions require that the disturbances must vanish at infinity and at any wall. The proper boundary conditions are of the following types:

Duct flows:

$$v(\pm h) = v'(\pm h) = 0. \tag{6.21}$$

Boundary Layers:

$$\begin{aligned} v(0) = v'(0) = 0, \\ v(\infty) = v'(\infty) = 0. \end{aligned} \tag{6.22}$$

Free-shear Layers:

$$v(\pm\infty) = v'(\pm\infty) = 0. \tag{6.23}$$

By applying mathematical procedures, expressions for the variable v and its derivatives as function of v'''' are defined. Substituting those expressions in equation (6.20) and after some algebra, the formulation of the eigenvalue problem is completed.

(g) The stability region and neutral curve.

The last step is the solution of the O-S equation for a given case, as it is presented in the next two subsections. The problem to be solved can be expressed in a non-dimensional form after applying the perturbation function:

$$\Phi(x, y, t) = \phi(y) \exp[i\alpha(x - ct)], \tag{6.24}$$

where Φ is the stream function defined as follows:

$$u = \frac{\partial \Phi}{\partial y}, \tag{6.25}$$

$$v = -\frac{\partial \Phi}{\partial x}. \tag{6.26}$$

After substitutions and some algebra we can obtain the following Orr-Sommerfeld (O-S) relation:

$$\phi'''' - 2\alpha^2\phi'' + \alpha^4\phi = i\alpha R \left[(U - c)(\phi'' - \alpha^2\phi) - U''\phi\right], \tag{6.27}$$

where R is the Reynolds number and all variables are now non-dimensional. Details about this derivation are shown in the next section. For now we are using this O-S as base for the next two examples. The following examples are presented

in order to validate the developed codes that will be used to analyze the liquid desiccant-humid air system.

6.3.2 Stability analysis of a Poiseuille flow using O-S

The non-dimensional velocity profile in this example is described by:

$$U(y) = 1 - y^2, \tag{6.28}$$

where $y \in [-1, 1]$.
Using equation (6.27) and boundary conditions $\phi(\pm 1) = \phi'(\pm 1) = 0$, the O-S stability problem is analyzed for Poiseuille flow.
To solve this problem we can use different methods such as finite differences or spectral methods. In this case we use the well known and documented Chebyshev polynomials expansion method [112, 113]. Thus, the highest derivative of ϕ can be represented by a finite series expansion of the form:

$$\phi''''(y) = \sum_{n=1}^{N+1} a_n T_{n-1}(y), \tag{6.29}$$

where T_{n-1} are a set of Chebyshev polynomials with collocation points selected as:

$$y_n = \cos(\pi(n-1)/N), \tag{6.30}$$

where $n = 1, 2, ..., N+1$, N represents the chosen number of terms, and the coefficients a_n can be obtained from boundary conditions, and the relation can be expressed in matrix form:

$$a = \hat{T}(y)\phi(y). \tag{6.31}$$

The other derivatives and the function itself can be obtained by successive integration. Thus, we can compute:

$$\Phi(y) = \int_{-1}^{y} \phi(\hat{y}) d\hat{y} = \sum_{n=1}^{N+1} b_n T_{n-1}(y). \tag{6.32}$$

This leads to the relationship

$$\Phi = \tilde{T}b = \tilde{T}Ia = \tilde{T}I\hat{T}\phi = W\phi. \tag{6.33}$$

Substituting the relations obtained into the equation (6.27) allows to obtain the following eigenvalue problem:

$$A\phi'''' = cB\phi'''', \tag{6.34}$$

where we can set values of Reynolds and α in order to solve for the complex values of c. The matrices A and B are defined as follows:

$$\begin{aligned} A_{jl} &= \delta_{jl} - (2\alpha^2 + i\alpha RU) \\ &\quad \times \left[\frac{1}{2}(2W_{1l}^3 - 3W_{1l}^4) + \frac{3}{2}\sum_{m=1}^{N+1} W_{jm}(W_{1l}^4 - W_{1l}^3) + W_{1l}^2\right] \\ &\quad + (\alpha^4 + i\alpha^3 RU + i\alpha RU'') \\ &\quad \times \left[\frac{1}{2}\sum_{m=1}^{N+1} W_{jm}^2(2W_{1l}^3 - 3W_{1l}^4) + \frac{3}{2}\sum_{m=1}^{N+1} W_{jm}^3(W_{1l}^4 - W_{1l}^3) + W_{1l}^4\right], \end{aligned} \tag{6.35}$$

and

$$\begin{aligned} B_{jl} &= i\alpha R\left[\frac{1}{2}(2W_{1l}^3 - 3W_{1l}^4) + \frac{3}{2}\sum_{m=1}^{N+1} W_{jm}(W_{1l}^4 - W_{1l}^3) + W_{1l}^2\right] \\ &\quad + i\alpha^3 R\left[\frac{1}{2}\sum_{m=1}^{N+1} W_{jm}^2(2W_{1l}^3 - 3W_{1l}^4) + \frac{3}{2}\sum_{m=1}^{N+1} W_{jm}^3(W_{1l}^4 - W_{1l}^3) + W_{1l}^4\right], \end{aligned} \tag{6.36}$$

where $W_{jl}^{p=1,2,3,4}$ are elements of the matrix W^p.
A Matlab code was developed to solve the eigenvalue problem and the results compared with the literature as a benchmark. The first comparison looks for the most unstable eigenvalue for $\alpha = 1$ and $R = 10000$, and the results are shown in Table 6.1. Table 6.2 shows a second validation, where the code is tested for a single value of α and several Reynolds numbers. Both tables show good agreement with literature [29, 112].

Table 6.1: The most unstable eigenvalue for plane Poiseuille flow using $\alpha = 1$ and $R = 10000$

N+1	Hatziavramidis and Ku [112]	Present
14	0.237248 + 0.003744i	0.237328 + 0.003746i
15	0.237453 + 0.003740i	0.237433 + 0.003733i
17	0.237528 + 0.003736i	0.237528 + 0.003736i
20	0.237526 + 0.003738i	0.237525 + 0.003737i

Table 6.2: The most unstable eigenvalue for plane Poiseuille flow using $\alpha = 1$ and several R

Re	Davey [29]	Present
10000	0.23753 + 0.00374i	0.237248 + 0.003744i
12000	0.22994 + 0.00416i	0.229935 + 0.004099i
14000	0.22368 + 0.00422i	0.223712 + 0.004219i
16000	0.21836 + 0.00404i	0.218355 + 0.004039i
18000	0.21374 + 0.00372i	0.213725 + 0.003745i

6.3.3 Stability analysis of a Blasius profile using O-S

A Blasius velocity profile and its boundary conditions are used as basic flow to study the stability using O-S, with the form:

$$f'''(\eta) + f(\eta)f''(\eta) = 0, \tag{6.37}$$

$$f(0) = f'(0) = 0, \;\; f'(\eta \to \infty) \sim 1. \tag{6.38}$$

In order to apply Chebyshev polynomials expansion we have to redefine the non-dimensional coordinate axis perpendicular to the flow η and the infinity condition at a finite value of $\eta = \eta_e$ as

$$\frac{\eta}{\eta_e} = \frac{(y+1)}{2}, \;\; [-1 \leq y \leq 1], \tag{6.39}$$

then, the Blasius profile and boundary conditions take the form:

$$f'''(y) + \frac{\eta_e}{2} f(y) f''(y) = 0, \tag{6.40}$$

$$f(-1) = f'(-1) = 0, \;\; f'(1) = \frac{\eta_e}{2}. \tag{6.41}$$

Similarly to the Poiseuille profile, the Chebyshev polynomials expansion method is applied but now directly to the Blasius profile. Thus, the highest derivative of $f(y)$ can be represented by a finite series expansion of Chebyshev polynomials of the form:

$$f'''(z) = \sum_{n=1}^{N+1} a_n T_{n-1}(y). \tag{6.42}$$

The other terms are found by a systematic integration and using boundary conditions. Solving the algebraic system, we can find the basic flow $U(y)$ which is related to $f(y)$ by $U(y) = f'(y)$. With the base flow, we can compute the eigenvalues for this system and find the most unstable values. Table 6.3 shows a list of single unstable eigenvalue for $\alpha = 0.179$ and $R = 580$ in original coordinate system. The results are in good agreement with literature [114].

Table 6.3: The most unstable eigenvalue of Blasius profile for $\alpha = 0.179$ and $R = 580$

η_e	**N-1**	**Zeibib [114]**	**Present**
10	36	0.367590 + 0.006429i	0.367588 + 0.006435i
	42		0.367586 + 0.006434i
	44	0.367591 + 0.006429i	0.367586 + 0.006434i
20	36	0.364034 + 0.007920i	0.363609 + 0.007757i
	44	0.364143 + 0.007959i	0.364146 + 0.007932i
	46	0.364137 + 0.007934i	0.364129 + 0.007967i
30	40	0.362681 + 0.009052i	0.363628 + 0.009389i
	42	0.363419 + 0.007859i	0.363194 + 0.008549i
	44	0.363997 + 0.007903i	0.363492 + 0.007776i

6.3.4 One phase flow contribution

The standard formulation for one phase flow stability analysis is used together with the introduction of the effects of the temperature dependent properties in a known velocity profile and then in its stability. We introduce these effects by computing together hydrodynamics, heat and mass exchange, using the codes presented in Chapter 5, to produce the steady state velocity profiles. Isothermal and non-isothermal eigenvalues are computed to analyze the stability of the flow and are shown in the results section.

6.4 Stability formulation for a liquid desiccant film and humid air interaction (two-phase flow)

6.4.1 Formulation of the governing equations

The configuration of a liquid desiccant film in parallel with a humid-air stream in two dimensions is considered now. The liquid film is at the bottom bounded by a thermally insulated wall, and the air stream flows on top of the film in parallel configuration. The air exerts a shear stress on the liquid, which sets the liquid motion. The thermo-physical properties for liquid and gas phases have been obtained from the references mentioned in previous chapters. Thus, we analyze the stability of the continuity and Navier-Stokes equations for the variables: velocity, V, and pressure, p:

$$\nabla \cdot \mathbf{V} = 0, \tag{6.43}$$

$$\frac{D\mathbf{V}}{Dt} = -\frac{1}{\rho}\nabla p + \nu \nabla^2 \mathbf{V}, \tag{6.44}$$

with boundary conditions

$$V(y=-1) = 0, \tag{6.45}$$

$$\frac{dV(y=1)}{dy} = 0, \tag{6.46}$$

$$\tau_l(y=0) = \tau_a(y=0). \tag{6.47}$$

Now, we assume a solution of the problem of the form: $V_o(y,t)$ and $p_o(x,t)$; and we determine whether these are stable solutions, by adding small disturbance variables $\hat{V}$ and $\hat{p}$, following the procedure described in Section 6.2.

After substituting the superimposed variables, subtracting the original quantities and neglect higher order terms, we obtain the linearized disturbance equations

as follows:

$$\frac{\partial \hat{u}}{\partial x} + \frac{\partial \hat{v}}{\partial y} + \frac{\partial \hat{w}}{\partial z} = 0, \quad (6.48)$$

$$\frac{\partial \hat{u}}{\partial t} + U\frac{\partial \hat{u}}{\partial x} + \hat{u}\frac{\partial U}{\partial x} + V\frac{\partial \hat{u}}{\partial y} + \hat{v}\frac{\partial U}{\partial y} + W\frac{\partial \hat{u}}{\partial z} + \hat{w}\frac{\partial U}{\partial z} \approx -\frac{1}{\rho}\frac{\partial \hat{p}}{\partial x} + \nu\nabla^2\hat{u}, \quad (6.49)$$

$$\frac{\partial \hat{v}}{\partial t} + U\frac{\partial \hat{v}}{\partial x} + \hat{u}\frac{\partial V}{\partial x} + V\frac{\partial \hat{v}}{\partial y} + \hat{v}\frac{\partial V}{\partial y} + W\frac{\partial \hat{v}}{\partial z} + \hat{w}\frac{\partial V}{\partial z} \approx -\frac{1}{\rho}\frac{\partial \hat{p}}{\partial y} + \nu\nabla^2\hat{v}, \quad (6.50)$$

$$\frac{\partial \hat{w}}{\partial t} + U\frac{\partial \hat{w}}{\partial x} + \hat{u}\frac{\partial W}{\partial x} + V\frac{\partial \hat{w}}{\partial y} + \hat{v}\frac{\partial W}{\partial y} + W\frac{\partial \hat{w}}{\partial z} + \hat{w}\frac{\partial W}{\partial z} \approx -\frac{1}{\rho}\frac{\partial \hat{p}}{\partial z} + \nu\nabla^2\hat{w}. \quad (6.51)$$

The resulting equations can be reduced to a single ordinary differential equation by assuming a locally parallel basic flow. Considering y the coordinate normal to the wall, the V velocity component is assumed negligible and U and W are assumed just functions of y. Using the assumption that the flow is two dimensional and incompressible, we can represent the disturbance velocities by the stream functions:

$$u_j = \frac{\partial \Phi}{\partial y}, \quad (6.52)$$

$$v_j = -\frac{\partial \Phi}{\partial x}. \quad (6.53)$$

Following the same nomenclature and because the primary flow only depends on the y-coordinate, the disturbance takes the form:

$$\Phi_j u = \phi_j(y)\exp(i\alpha(x - ct)), \quad (6.54)$$

where i is the imaginary unit, α is a real wavenumber, and c is the complex wave velocity.
Because of Squire's theorem, introducing the stream function into the linearized Navier-Stokes equations results in the well-known Orr-Sommerfeld equations as function of $\phi(y)$. The dimensionless equations for each one of the domains are introduced as follows. In the liquid side the film thickness is utilized as characteristic length for dimensionalization and the mean air velocity is used to dimensionalize the velocities.

$$\phi_1'''' - 2\alpha^2\phi_1'' + \alpha^4\phi_1 = i\alpha R\left[(U_1 - c)(\phi_1'' - \alpha^2\phi_1) - U_1''\phi_1\right]. \quad (6.55)$$

This equation is valid in the domain: $-1 < y < 0$, primes are used to indicate differentiation with respect to y, the subscript 1 identifies the liquid domain, and R represents the Reynolds number for the liquid film. Furthermore, non-penetration and non-slip conditions are considered as boundary conditions:

$$\phi_1(y=-1) = \phi_1'(y=-1) = 0. \tag{6.56}$$

For the humid air domain $0 < y < 1$, the Orr-Sommerfeld equation takes the form:

$$\phi_2'''' - 2\alpha^2\phi_2'' + \alpha^4\phi_2 = \left(i\alpha R\frac{r}{m}\right)\left[(U_2 - c)(\phi_2'' - \alpha^2\phi_2) - U_2''\phi_2\right], \tag{6.57}$$

where subscript 2 indicates the humid air subdomain, $r = \rho_2/\rho_1$ and $m = \mu_2/\mu_1$ are the density and viscosity ratios, respectively. The Boundary conditions in the air domain are:

$$\phi_2(y=1) = \phi_2'(y=1) = 0. \tag{6.58}$$

Continuity of the velocity components is required at the interface as well as the balance of the normal and tangential stresses. Therefore, the boundary conditions become:

$$\phi_1 = \phi_2 \ at\ y = 0, \tag{6.59}$$

$$\phi_1' + \frac{U_1'\phi_1}{c} = \phi_2' + \frac{U_2'\phi_2}{c},\ at\ y = 0, \tag{6.60}$$

$$\phi_1'' + \alpha^2\phi_1 + \frac{U_1''\phi_1}{c} = m\left(\phi_2'' + \alpha^2\phi_2 + \frac{U_2''\phi_2}{c}\right),\ at\ y = 0, \tag{6.61}$$

$$\begin{aligned}(\phi_1''' - 3\alpha^2\phi_1') + i\alpha R(c\phi_1' + U_1'\phi_1) - m(\phi_2'' - 3\alpha^2\phi_2') \\ -ir\alpha R(c\phi_2' + U_2'\phi_2) - i\alpha R(F + \alpha^2 S)\frac{\phi_2}{c} = 0,\ at\ y = 0,\end{aligned} \tag{6.62}$$

where S and F are the inverse Weber and Froude numbers respectively and they are defined as follows:

$$S = \frac{\sigma}{\rho_1 U_{y=0}^2 d_1}, \tag{6.63}$$

$$F = \frac{g(\rho_1 - \rho_2)d}{(\rho_1 U_{y=0}^2)}. \tag{6.64}$$

6.4.2 Small wavenumber technique

This technique was introduced by Yih [115, 116] and applied by him to two parallel fluid flows and wave formation on a liquid layer years later [28,117], where a detailed procedure was introduced. A summary of the procedure is presented here, in order to introduce its application to the liquid desiccant film and humid air interaction.
The governing equations (6.55) and (6.57), and boundary conditions in equations (6.56), and (6.58) to (6.62) are solved by a non-singular perturbation where $\alpha \to 0$. First, all terms in the equations containing α are ignored and the coefficients of the first polynomial approximation are found. The coefficients may be expressed in function of the ratios m and r introduced above, including an expression for the eigenvalue c. Then, the terms in the equations containing α^2 and higher are ignored and the first approximation is used as the known function to solve the new fourth order differential equations together with the corresponding boundary conditions. An expression for the eigenvalue, c of the most unstable mode is obtained, which is function of the wave number, α, the Reynolds number, R, and the function J, that is function of the thickness, density and viscosity ratios, n, r, and m, respectively as follows:

$$c = \alpha R J(m, n, r). \tag{6.65}$$

Figures 6.1 and 6.2 show the relationship between the function J, and the viscosity ratios of two fluids, m. Several cases of thickness ratio, n, and density ratio, r are plotted. One can conclude for instance, that in Fig. 6.1 for $n \leq 1$ the flow is unstable for all m greater than one. Cases where $n > 1$ and $m > 1$ are shown in Fig. 6.2, where most of the examples are stable except for $n = 1.25$ which presents stability for $0 \leq m \leq 9$, and is unstable for $m > 9$. These figures also show how the written codes are matching the reference model [28] for several rations of thickness, density and viscosity. The tested codes are used to find the neutral stability curves shown in the results section of this chapter.

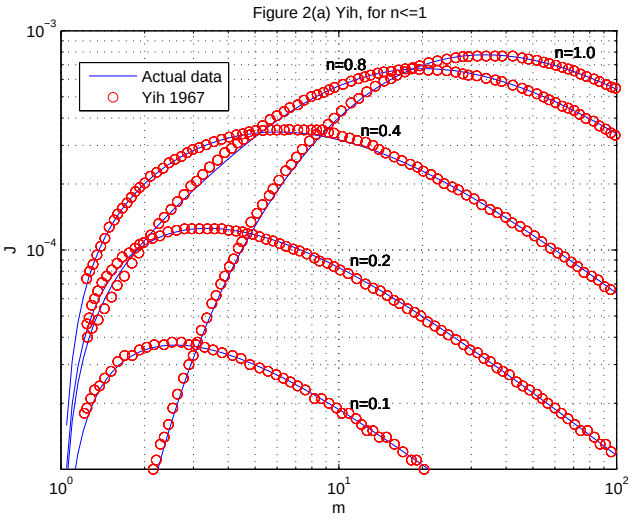

Figure 6.1: The imaginary part of the eigenvalue of the most unstable mode vs viscosity ratio. Benchmark general solution for $n \leq 1$.

6.4.3 Complete orthonormalization technique

This technique allows us to generate a computational model that solves equations (6.55) and (6.57), together with the bounday conditions given by Eq. (6.56) and from Eq. (6.58) to Eq. (6.62). The method was developed by Davey [29] four decades ago, based on the near-orthogonalization method by Kaplan [118] and using a variational approximation from Lee and Reynolds [119], as initial guess for the eigenvalues in the shooting process. A brief description of the method is presented to show how the technique was applied to the benchmark and the present problem.

The shooting method to be implemented considers a general solution for the vector with the form:

$$Y = \left[\phi, \frac{d\phi}{dy}, \frac{d^2\phi}{dy^2}, \frac{d^3\phi}{dy^3}\right]^T, \tag{6.66}$$

where the homogeneous boundary conditions must be satisfied. For instance, in a Poiseuille flow $\phi = \frac{d\phi}{dy} = 0$ at both walls.

The main idea is to look for the most unstable mode by determining its eigenvalue instead of looking for the associated eigenfunction. As it was indicated above, the initial eigenvalue is assumed to be known from a variational approximation. Thus,

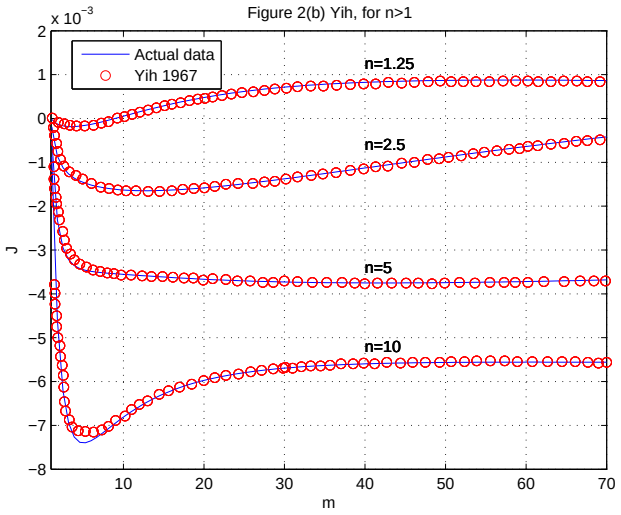

Figure 6.2: The imaginary part of the eigenvalue of the most unstable mode vs viscosity ratio. Benchmark general solution for $n > 1$.

for each value in the discretized domain in the y direction, we integrate the vector Y in the equation (6.66), obtaining

$$Y_{i+1} = AY_i, \tag{6.67}$$

where the elements of the transfer matrix A are linearly independent of Y_i. To build the transfer matrix A for a given eigenvalue, the differential equation can be integrated in each step of the domain in consideration, using as initial Y_0 the orthonormal vectors $[1,0,0,0]^T$, $[0,1,0,0]^T$, $[0,0,1,0]^T$ and $[0,0,0,1]^T$ sequentially. A fourth-order Runge-Kutta method with 150 integration steps is used, and the obtained vector Y_1 is the first column of the matrix A and so on.
Once the transfer matrix is built, we may apply the boundary conditions. In the example of Poiseuille flow, six scalar equations can be obtained, four from Eq.(6.67) and two from the boundary conditions. Thus, a nontrivial solution is required to be satisfied and this is only possible if the determinant of the system vanishes. From the solutions of this determinant we find an eigenvalue that will be the base for the next iteration.
A significant advantage of this method is that, as opposed to the small wavenumber technique with O-S stability analysis, it can be applied to both isothermal and non-isothermal systems. Examples of the implementation of this method may be found in Solorio and Sen [100] for linear stability of a cylindrical falling film, and

Calderon-Munoz et al. [120] where instabilities of a one-dimensional electron flow is studied. In the present study we validate the code by comparison with Daveys results for Poiseuille flow as it is shown in Table 6.4. It is important to note that some of the differences in the results are due to the use of double precision calculations as opposed to single precision used in many older references.

Table 6.4: The eigenvalue c for the most unstable mode of plane Poiseuille flow when $\alpha = 1$ and using one orthonormlization

Re	**Davey [29]**	**Present**
3000	0.29229 - 0.01018i	0.29601 - 0.00941i
3500	0.28488 - 0.00722i	0.28572 - 0.00792i
4000	0.27854 - 0.00495i	0.28314 - 0.00564i
4500	0.27302 - 0.00317i	0.27543 - 0.00351i
5000	0.26810 - 0.00178i	0.27063 - 0.00159i
6000	0.25981 - 0.00010i	0.26241 - 0.00012i
7000	0.25362 + 0.00012i	0.25822 + 0.00003i

6.4.4 Two phase flow contribution

By using the two methodologies presented above, small wavenumber and complete orthonormalization techniques, a novel analysis on the liquid desiccant film is introduced, where the temperature dependent properties are considered to calculate the velocity profiles that are used for the calculation of the eigenvalue of the most unstable mode. Thus, non-uniform temperature profiles across and along the film are used instead of the traditional average temperatures, to compute thermo-physical properties and Navier-Stokes equations, to obtain velocity profiles. Those velocity profiles are used to characterize the flow stability. Theoretical cases with viscosity, density and thickness ratios are tested as well as cases with data from normal operating conditions of liquid desiccants. Results and discussions are presented in the next section.

6.5 Results

By using the methodologies presented above, a series of cases are simulated to characterize the stability of a liquid desiccant film under the influence of the heat and mass exchange process.

6.5.1 Effect of properties distribution in a single fluid

In this subsection, the results for the stability analysis of a single fluid with the complete orthonormalization technique are presented. First, a comparison of isothermal and non-isothermal results for a liquid desiccant Poiseuille flow analysis are shown, and then results for a liquid desiccant film with free surface flow are obtained.

Effect in Poiseuille flow

In this case, the inlet and wall conditions are prescribed, from which it is possible to calculate the inlet value of Reynolds number, and the Navier-Stokes equations can be solved for the rest of the domain by using the methodology explained in Chapter 5. If the stability analysis technique in subsection 6.4.3 is applied to a traditional isothermal velocity profile, an isothermal eigenvalue is obtained. Conversely, if temperature dependent properties are used in the solution of the Navier-Stokes equations, a non-isothermal eigenvalue is computed. Table 6.5 shows the isothermal and non-isothermal comparison together with several conditions for wall and inlet temperatures. Considering a cold inlet temperature a destabilization effect appears if the wall temperature increases, which is consistent with the computed outlet Reynolds number. For a hot inlet temperature and decreasing the wall temperatures, a similar behavior is observed. In general the comparison results are consistently close and low temperatures are recommended to work with the liquid desiccant, which is consistent with the conclusions in chapter 4. Moreover, relatively high Reynolds numbers were chosen to show the stability condition near the transition from laminar to turbulent flow.

Table 6.5: The most unstable eigenvalue for plane Poiseuille flow using $\alpha = 1$ and inlet $Re = 3000$ for isothermal vs non-isothermal properties.

Outlet Re	**Inlet T. [°C]**	**Walls T. [°C]**	**Isothermal Eig.**	**Non-isothermal Eig.**
2504	5	1	0.304643 - 0.014536i	0.305530 - 0.014761i
3000	5	5	0.295927 - 0.010547i	0.296894 - 0.010739i
3434	5	10	0.289474 - 0.007898i	0.290477 - 0.008067i
4479	5	20	0.276990 - 0.003520i	0.278077 - 0.003613i
5629	5	30	0.266843 - 0.001201i	0.268073 - 0.000983i
6877	5	40	0.224961 - 0.000198i	0.223452 - 0.000475i
7534	5	45	0.225031 + 0.000271i	0.225000 + 0.000274i
3712	80	90	0.285787 - 0.006499i	0.287035 - 0.006621i
3000	80	80	0.295927 - 0.010547i	0.296899 - 0.010739i
2245	80	60	0.308014 - 0.016207i	0.308881 - 0.016441i
1604	80	40	0.326399 - 0.026585i	0.327103 - 0.026864i
1045	80	20	0.347377 - 0.040957i	0.347897 - 0.041248i
801	80	10	0.360342 - 0.051020i	0.360755 - 0.051294i

Effect in Couette flow

The second case represents a closer approximation to the problem in the heat and mass exchanger, where operating conditions from Chapter 5 are used as source of data at different positions of the channel. L represents the total length of the channel and is used with dimensions in order to be consisstent with previous chapters. Thus, eigenvalues that correspond to the most unstable mode are computed by using the complete orthonormalization technique at several locations along the channel. Even though the used Reynolds number are low, and that the total variation in Reynolds number along the channel is about 25%, instabilities appears in all the cases for a wave number of one. Similar instabilities are obtained by Solorio and Sen [100] but for a cylindrical falling film.

6.5.2 Effect of change in property ratios in two-phase flows

Several ratios of densities, viscosities and thicknesses are tested in order to analyze the stability of the liquid desiccant film. Initially, keeping most parameters

Table 6.6: The most unstable eigenvalue for the liquid desiccant and humid air flow using $\alpha = 1$, and for non-isothermal properties.

L [**m**]	**Re**	**T** [°**C**]	**C** $[kg_w/kg_{sol}]$	**Non-isothermal Eig.**
0	1	17.4	0.6	0.430464 + 0.041536i
0.008	0.8	14.3	0.6010	0.3949271 + 0.022547i
0.016	0.75	12.4	0.6018	0.247834 + 0.009798i
0.025	0.73	11.2	0.6021	0.227693 + 0.0073520i
0.05	0.732	10.5	0.6032	0.226643 + 0.0076301i
0.1	0.736	10.5	0.6051	0.220161 + 0.007738i
0.2	0.745	10.5	0.6075	0.225031 + 0.009471i
0.3	0.755	10.5	0.6083	0.242533 + 0.009987i

fixed and varying one ratio at a time, the stability of the system is described for a chosen range of α and Re values. For simplicity, the parameters used to characterize the air domain are the starting point for the simulations. For instance, the initial density ratio is taken as one fixing the density of the air and letting the density of the liquid to vary.
First, keeping the thickness ratio fixed, which does not change significantly under real operating conditions of a heat and mass exchanger, averages of densities and viscosities are taken across the main stream of different locations along the channel. The resulting set of parameters are used to study the flow stability characteristics.

Effect of varying the density ratio

The effect of the density ratio ($r = \rho_2/\rho_1$) in the two fluid flow interaction using the small wavenumber technique is shown in Figures 6.3 (a-d), where the neutral stability curve is obtained for different values of r. The contours show the imaginary part of the computed eigenvalue distribution as function of laminar Reynolds numbers Re and wave-numbers α. The result depicts the neutral stability curve ($c = 0$) as a horizontal line traveling upward as r increases. Figure 6.3 (a) shows instabilities everywhere for any combination of wave and Reynolds numbers for a value of $r = 1$ (i.e., fluids with the same density). In Figure 6.3(b) an incipient stable zone appears at the bottom and moves upward as r increases, as seen in Figures 6.3(c) and 6.3(d).

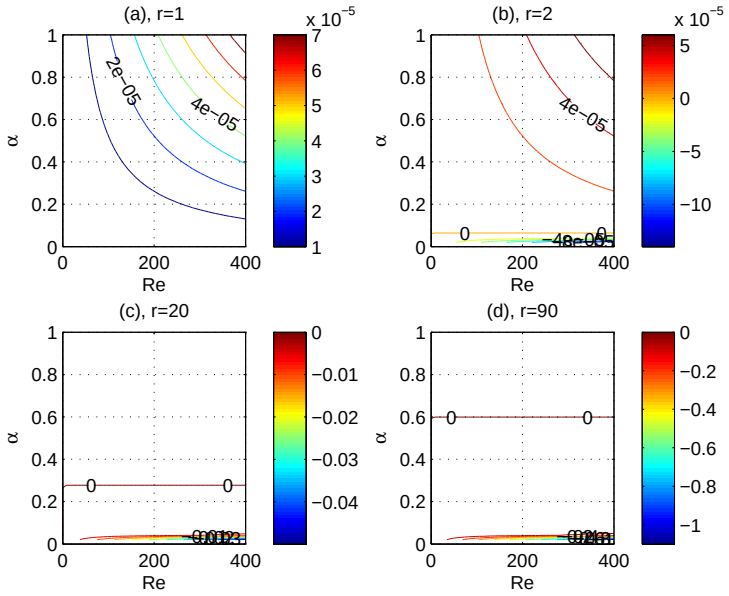

Figure 6.3: Effect of density ratio r in two fluids interaction. α vs Re for real values. m = 50, n = 0.023

The location of the horizontal neutral stability curve is described by a nonlinear curve when plotted as a function of the density ratio, r, as seen in Figure 6.4. By definition, the neutral stability curve is obtained when the imaginary part of the eigenvalue is zero. For values of density ratio from 1 to approximately 250, the horizontal location of the stability curve increase quadratically with respect to $r(\alpha(c = 0)) = p1 \times \alpha^2 + p2 \times \alpha + p3$, where the coefficients are: $p1 = 248.1$, $p2 = -0.1495$ and $p3 = 0.9598$. The statistical parameters are: $R^2 = 1$ and RMSE: 0.02177.

As the density ratio increases (i.e., the density of the liquid domain increases), the location of the neutral stability curve moves to larger values of α covering a larger area of the domain with negative imaginary parts of the eigenvalues which translates into a more stable behavior. As mentioned before, in order to generate the results of Fig. 6.3, the change in r is controlled by fixing the density in the air domain and varying the density in the liquid domain. Thus, the increment in the ratio of densities with m and n fixed, produces a stabilizing effect on the flow

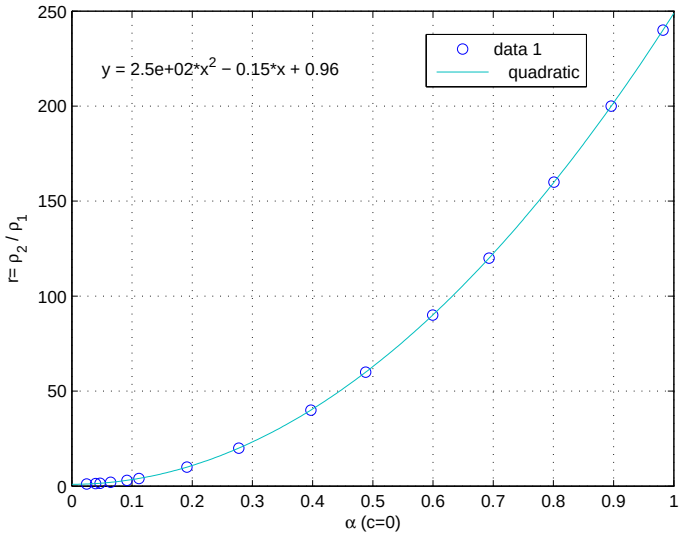

Figure 6.4: Density ratio (r) vs Wavenumber $\alpha(c = 0)$, for Reynolds numbers up to 400.

Effect of varying the viscosity ratio

The effect of the viscosity ratio ($m = \mu_2/\mu_1$) in the described parallel flow is analyzed in this subsection using the small wavenumber technique, velocity profiles from Chapter 5 and property average values. For several values of m, keeping the rest of the parameters fixed, the imaginary part of the eigenvalues are plotted as function of Reynolds and wave-number. Figure 6.5 shows the results for several values of viscosity ratio as follows: (a) $m = 1.25$, (b) $m = 2$, (c) $m = 10$ and (d) $m = 25$. The figure shows the stability of the film as the viscosity of the humid-air is fixed and viscosity of the liquid film is increased.
In this case, the location of the neutral stability curve can be also predicted but it has a more linear behavior, as shown in Figure 6.6 by $m(\alpha(c = 0)) = p1 \times \alpha + p2$, where the linear coefficients are: $p1 = 28.11$ and $p2 = -0.5291$. The statistical parameters are: $R^2 = 0.9997$, and RMSE $= 0.1618$.
Similarly as in density ratios, as the viscosity ratio increases (i.e., the viscosity of the liquid domain increases), the location of the neutral stability curve moves linearly to larger values of α covering a larger area of the domain with negative imaginary parts of the eigenvalues which translates into a more stable behavior. In processes where the liquid film viscosity is increased, stabilization effects will appear.

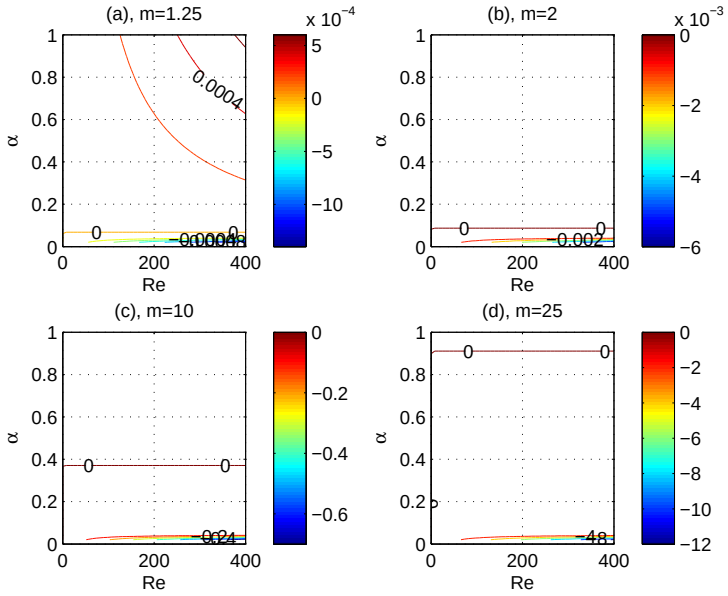

Figure 6.5: Effect of viscosity ratio m in two fluids interaction. α vs Re for real values. r = 830, n = 0.023.

Effect of varying the thickness ratio

The final effect related with two-fluids is the thickness ratio $n = \delta_2/\delta_1$, and its influence in the stability of the liquid desiccant film. In this subsection, we also work with the small wavenumber technique and profiles computed with the finite volume method described in Chapter 5. The traditional way to control wave formation in falling liquid films is to provide small volumetric flow rates which means small liquid film thickness. This effect is evident in Figure 6.7 where it is shown that if the ratio n decreases the stable region increases. No evidence about this issue has been shown in the literature.

In Figure 6.7 the location of the neutral stability curve is shown, and can be predicted by the power function $m(\alpha(c = 0)) = a \times \alpha^b$, as shown in Figure 6.8, where the coefficients are: $a = 0.04087$ and $b = -0.6978$. The statistical parameters are: $R^2 = 0.9991$ and RMSE = 0.004235.

We may conclude from this subsection that as the thickness ratio increases (i.e., the thickness of the liquid film increases), the location of the neutral stability curve moves to smaller values of α covering a smaller area of the domain with negative imaginary parts of the eigenvalues which translates into a more unstable behavior. Reduction of the liquid film thickness increases stability which is in

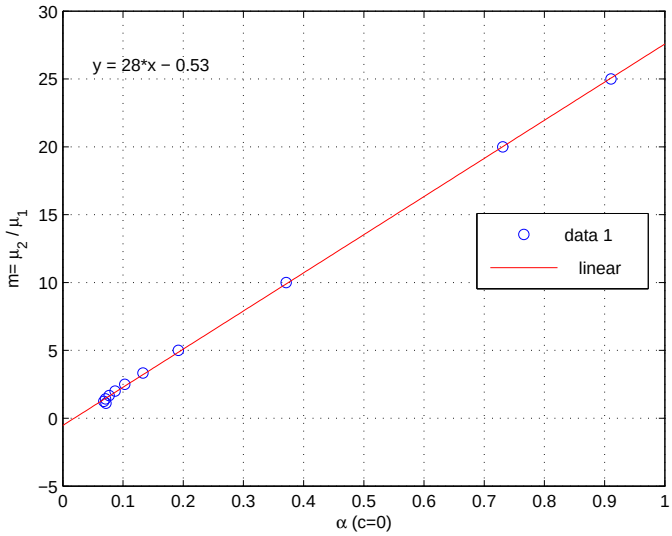

Figure 6.6: Viscosity ratio (m) vs Wavenumber $\alpha(c = 0)$, for Reynolds numbers up to 400.

accordance with the traditional way to ensure stability in the film by reducing volumetric flow rates that guarantee small thickness ratios.

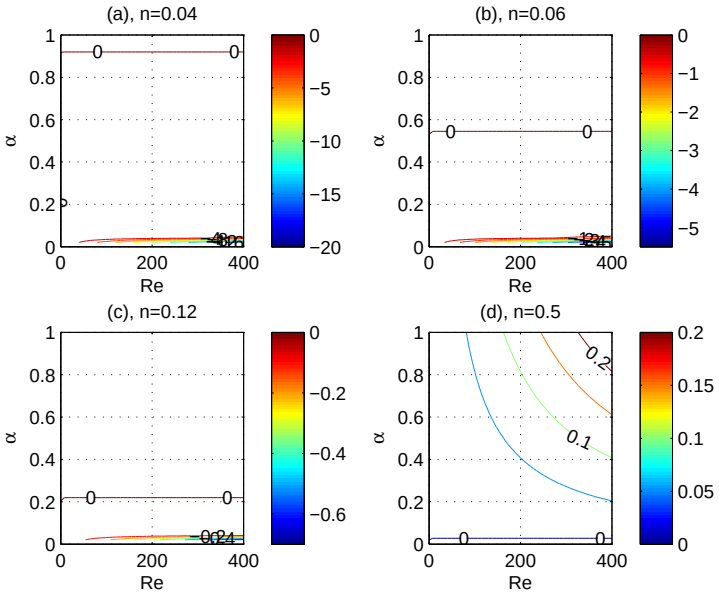

Figure 6.7: α vs Re for real values values. r = 830, m = 50, keeping δ_2 = 7e-5 [m] and recalculating δ_1 = (1/n)*δ_2.

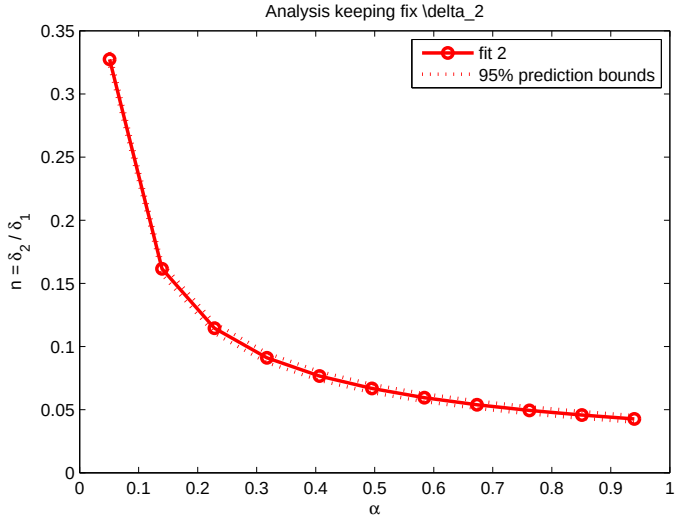

Figure 6.8: Thickness ratio n (Fixed δ_2) vs Wavenumber $\alpha(c = 0)$.

Conclusions

Hydrodynamical instabilities in a liquid desiccant film are analyzed when the film is exposed to the influence of a humid-air stream within a heat and mass exchanger. The small wavenumber analysis, and the complete orthonormalization technique are used to find the instabilities considering one and two-phase flows configurations.

A novel analysis on the liquid desiccant film is introduced, where the temperature dependent properties are considered to calculate the velocity profiles that are part of the calculation of the eigenvalue of the most unstable mode. Thus, non-uniform temperature profiles across and along the film were used instead of the traditional average temperature, to compute properties and Navier-Stokes equations, to find the velocity profiles, and to characterize the flow.

The study shows that the liquid desiccant film is unstable for most of the tested Reynolds numbers and for wave numbers near to one. However, particular configurations of density, viscosity and thickness ratios between the two fluids, and the consideration of temperature-dependent properties, may have a stabilization effect. Thus, the evaluation of the density ratio in the stability analysis shows a stabilizing effect as r increases. Moreover, we presented, how if the thickness ratio n decreases there are more stable conditions, as has been commented in literature without further evidence of support. Finally, even though the Reynolds number in a realistic liquid desiccant film are low, and that the total variation in Reynolds number along the channel is about 25%, instabilities appears in all these cases (for $\alpha = 1$).

The complete orthonormalization technique is suitable to solve the fourth order differential equation O-S. However, this methodology may also be used to solve a non-simplified and disturbed system of differential equations, in which the distribution of the properties in the domain can be integrated directly in the calculations of the stability analysis. Thus, extreme cases with thickness ratios smaller than 0.05 can be solved, including additional equations from the lubrication theory.

Chapter 7

Conclusions and Future work

The interaction of liquid desiccant films and humid air was analyzed in detail, within the understanding of a liquid desiccant system working with calcium chloride solution which absorbs water from moist air near freezing conditions. One, two and three dimensional numerical models using finite differences and finite volume methods were developed in order to simulate the coupled momentum, mass and energy transfer, where velocity, temperature, and concentration distributions were computed. Film stability was studied using the Orr-Sommerfeld equation with the small wavenumber technique and complete orthonormalization method.

The results show that the dew point temperature of the air downstream of the absorber is comparable to the evaporator surface temperature suggesting the potential to delay the formation of ice on the cooling coil, thus reducing the number of defrosting cycles, therefore, lowering operating costs. Moreover, the results show that the internal heat exchanger (IHX) effectiveness has a direct impact on the inlet temperature of the liquid desiccant leaving the absorber. High IHX effectiveness results in high absorber effectiveness. However, IHX effectiveness less than 60% leads to a desorption process where the liquid desiccant concentration increases, augmenting the humidity ratio of the air flowing through the mass exchanger.

A reduction of approximately 25% in Reynolds number is observed, when inlet and outlet average values are compared in the case of temperature dependent properties in the the liquid film. Peclet numbers greater than two are observed in the calculations, showing the necessity to use a hybrid scheme in the finite volume method even though the tested flow had low Reynolds numbers.

The stability analysis of this laminar flow interaction is obtained solving the traditional Orr-Sommerfeld problem for a finite value of the Reynolds number above which instability occurs, leading to the definition of the critical Reynolds

number. Stabilizing and de-stabilizing effects of different parameters were identified in the results.

Bibliography

[1] Mamoru Ishii and Takashi Hibiki. *Thermo-fluid dynamics of two-phase flow.* Springer New York Dordrecht Heidelberg London, 2011.

[2] Robert Byron Bird, Warren E. Steward, and Edwin N. Lightfoot. *Transport Phenomena.* John Wiley and Sons, second edition, 2002.

[3] Ahmad Ali. *Analysis of heat and mass transfer between air and falling film desiccant for different flow configurations in the presense of ultrafine particles.* PhD thesis, The Ohio State University, 2003.

[4] P. Gandhidasan. A simplified model for air dehumidification with liquid desiccant. *Solar Energy*, 76, 2004.

[5] D.D. Joseph and Y.Y. Renardy. *Fundamentals of two-fluid dynamics, Part I: Mathematical theory and applications.* Springer Verlag, New York, 1993.

[6] Robert Betchov and Jr. William O. Criminale. *Stability of Parallel Flows.* Academic Press New York London, 1967.

[7] Lewis G. Harriman III and James Judge. Dehumidification equipment advances. *ASHRAE Journal*, 44(8):S22–S29, August 2002.

[8] S. Agunaga Bialous and S.A. Glantz. ASHRAE Standard 62: tobacco industry's influence over national ventilation standards. *Tobacco Control*, 11:315–328, September 2002.

[9] Andrew Persily. The revision of standard 62: What a difference a decade makes. In National Institute of stabdards and technology NIST, editors, *Preceedings: Indoor Air 2002, 9th International Cnference on Indoor Air Quality and Climate in Monterey, California*, pages 328–333. National Institute of stabdards and technology NIST, June 2002.

[10] IEA. World energy outlook 2006. Technical report, International Energy Agency, 2006.

[11] S.V. Patankar. *Numerical Heat Transfer and Fluid Flow .* Hemisphere, New York, 1980.

[12] F.M. White. *Viscous Fluid Flow.* McGraw-Hill., New York, third edition, 2006.

[13] Sergio Manuel Pineda and Gerardo Diaz. Performance of an adiabatic cross-flow liquid-desiccant absorber inside a refrigerated warehouse. *International Journal of Refrigeration*, 34:138–147, 2011.

[14] Sergio Manuel Pineda and Gerardo Diaz. Analysis of heat and mass transfer of an adiabatic cross-flow liquid desiccant absorber operating at low temperatures. In *Proceedings of ASME Summer Heat Transfer Conference, Paper HT2009-88255*, pages 1–9, San Francisco, 2009.

[15] Sergio Manuel Pineda and Gerardo Diaz. Contribution of an internal heat exchanger to the performance of a liquid desiccant dehumidifier operating near freezing conditions. *International Journal of Thermal Sciences*, 50:2304–2310, 2011.

[16] EIA. International energy outlook 2008 - highlights. Technical Report DOE/EIA-0484, Energy Information Administration, June 2008.

[17] CEC. Title 24 buildings energy effuciency standards. refrigerated warehouses case report. Report, California Energy Commission, Pacific Gas and Electric Company, 2007.

[18] Scott Feyka and K. Vafai. An investigation of a falling film desiccant dehumidification/regeneration cooling system. *Heat Transfer Engineering*, 28(2):163–172, 2007.

[19] Sanjeev Jain and P.K. Bansal. Performance analysis of liquid desiccant dehumidification systems. *International Journal of Refrigeration*, 30:861–872, 2007.

[20] N. Fumo and D.Y. Goswami. Study of an aqueous lithium chloride desiccant system: air dehumidification and desiccant regeneration. *Solar Energy*, 72(4):351–361, 2002.

[21] Xiaohua Liu, Yi Jiang, Jianjun Xia, and Xiaomin Chang. Analytical solutions of coupled heat and mass transfer processes in liquid desiccant air dehumidifier/regenerator. *Energy Conservatins and Management*, 48:2221–2232, 2007.

[22] L.C.S. Mesquita, S.J. Harrison, and D. Thomey. Modeling of heat and mass transfer in parallel plate liquid-desiccant dehumidifiers. *Solar Energy*, 80:1475–1482, 2006.

[23] A. Rahamah, M.M. Elsayed, and N.M. Al-Najem. A numerical solution for cooling and dehumidification of air by a falling desiccant film in parallel flow. *Renewable Energy*, 13(3):305–322, January 1998.

[24] S.V. Patankar and D.B. Spalding. A calculation procedure for heat, mass and momentum transfer in three dimensional parabolic flows. *Int. J Heat Mass Transfer*, 15:1787–1806, 1972.

[25] S.V. Patankar and D.B. Spalding. A computer model for three-dimenisional flow in furnaces. *Proc. 14 Symp. (Int.) Combustion*, page 605, 1972.

[26] I. Heynderickx and W. Potze. Non-isothermal poiseuille flow of a liquid crystalline material 1. flow-aligning nematic. *Journal of Non-Newtonian Fluid Mechanics*, 59(23):155 – 172, 1995.

[27] Felix Sharipov. Non-isothermal gas flow through rectangular microchannels. *Journal of Micromechanics and Microengineering*, 9(4):394, 1999.

[28] Chia-Shun Yih. Instability due to viscosity stratification. *J. Fluid Mech.*, 27(2):337–352, 1967.

[29] A. Davey. A simple numerical method for solving orr-sommerfeld problems. *Q.J. Mech. appl. Math*, 26(4):401–411, 1973.

[30] EIA. World energy outlook 2006. Technical report, International Energy Agency, 2006.

[31] Thosapon Katejanekarn and S. Kumar. Performance of a solar-regenerated liquid desiccant ventilation pre-conditioning system. *Energy and Buildings*, 40:1252–1267, 2008.

[32] George O. G. Lof. *House Heating and Cooling with Solar Energy*. Madison: University of Wisconsin Press, 1995.

[33] Yonggao Yin and Xiaosong Zhang. A new method for determining coupled heat and mass transfer coefficients between air and liquid desiccant. *International Journal of Heat and Mass Transfer*, 51:3287–3297, 2008.

[34] K. Daou, R.Z. Wang, and Z.Z. Xia. Desiccant cooling air conditioning: a review. *Renewable and Sustainable Energy Reviews*, 10:55–77, 2006.

[35] Douglas R. Kosar, Michael J. Witte, Don B. Shirey III, and Roger L. Hedrick. Dehumidification issues of standard 62-1989. *ASHRAE Journal*, March 1998.

[36] Lewis G. Harriman III, Michael J. Witte, Marek Czachorski, and Douglas R. Kosar. Evaluating active desiccant systems for ventilating commercial buildings. *ASHRAE Journal*, October 1999.

[37] S.S. Elsayed, Y. Hamamoto, A. Akisawa, and T. Ksahiwagi. Analysis of an air cycle refrigerator driving air conditioning system integrated desiccant system. *Int. J. Refrigeration*, 29:219–228, 2006.

[38] S.S. Elsayed, T. Miyazaki, Y. Hamamoto, A. Akisawa, and T. Ksahiwagi. Performance analysis of air cycle refrigerator integrated desiccant system for cooling and dehumidifying warehouse. *Int. J. Refrigeration*, 31:189–196, 2008.

[39] PG&E. Aggregated data for investor-owned utilities, publicly owned utilities, and combined utilities. appendix c. Technical report, California Energy Commission, Pacific Gas and Electricity Company, 2007.

[40] Y. K. Yadav. Vapour compression and liquid - desiccant hybrid solar space - conditioning system for energy conservation. *Renewable Energy*, 6(7):719–723, 1995.

[41] Cheng Qin Ren, Min Tu, and Hua Hui Wang. An analytical model for heat and mass transfer processes in internally cooled or heated liquid desiccantair contact units. *International Journal of Heat and Mass Transfer*, 50:3545–3555, 2007.

[42] Douglas R. Kosar. Dehumidification system enhancements. *ASHRAE Journal*, February 2006.

[43] Lewis G. Harriman III, Joseph Lstlburek, and Reinhold Kittler. Improving humidity control for commercial buildings. *ASHRAE Journal*, 42(11):24–32, November 2000.

[44] S. A. Abdul-Wahab, Y.H. Zurigat, and M.K. Abu-Arabi. Predictions of moisture removal rate and dehumidification effectiveness for structured liquid desiccant air dehumidifier. *Energy*, 29:19–34, 2004.

[45] Adnan A. Kinsara, Omar M. Rabghi, and Moustafa M. Elsayed. Parametric study of an energy efficient air conditioning system using liquid desiccant. *Applied Thermal Engineering*, 18(5):327–335, 1997.

[46] Sanjeev Jain, P.L. Dhar, and S.C. Kaushik. Experimental studies on the dehumidifier and regenerator of a liquid desiccant cooling system. *Applied Thermal Engineering*, 20:253–267, 2000.

[47] Sanjeev Jain, P.L. Dhar, and S.C. Kaushik. Evaluation of liquid dessicant based evaporative cooling cycles for typical hot and humid climates. *Heat Recovery Systems and CHP*, 14(6):621–632, 1994.

[48] X.H. Liu, Y. Jiang, X.M. Chang, and X.Q. Yi. Experimental investigation of the heat and mass transfer between air and liquid desiccant in a cross-flow regenerator. *Renewal Energy*, 32:1623–1636, 2007.

[49] Arshad Y. Khan and Jorge L. Martinez. Modelling and parametric analysis of heat and mass transfer performance of a hybrid liquid desiccant absorber. *Energy Convers. Mgmt.*, 39(10):1095–1112, 1998.

[50] E. Mezaache and M. Daguenet. Effects of inlet conditions on film evaporation along an inclined plate. *Solar Energy*, 78:535–542, 2005.

[51] A. Ali, K. Vafai, and A.R.A. Khaled. Comparative study between parallel and counter flow configurations between air and falling film desiccant in the presence of nanoparticle suspensions. *International Journal of Energy Research*, 27:725–745, 2003.

[52] A. Ali and K. Vafai. An investigation of heat and mass transfer between air and desiccant film in an inclined parallel and counter flow channels. *International Journal of Heat and Mass Transfer*, 47:1745–1760, 2004.

[53] Moonsoo Park. *Analysis of couple heat and mass transfer between a falling desiccant film and air in cross flow*. PhD thesis, The University of Texas at Austin, May 1994.

[54] M. S. Park, John R. Howell, Gary C. Vliet, and John L. Peterson. Numerical and experimental results for coupled heat and mass transfer between a desiccant film and air in cross-flow. *International Journal of Heat and Mass Transfer*, 37:395–402, 1994.

[55] A. Ali, K. Vafai, and A.R.A. Khaled. Analysis of heat and mass transfer between air and falling film in a cross flow configuration. *International Journal of Heat and Mass Transfer*, 47:743–755, 2004.

[56] Anthony F. Mills. *Basic heat and mass transfer*. Prentice-Hall, 1999.

[57] Frank P. Incropera and David P. DeWitt. *Fundamentals of heat and mass transfer*. Wiley, third edition edition, 1990.

[58] A.K. Singh, Harpal Singh, S.P. Singh, and R.L. Sawhney. Numerical calculations of psychrometric properties on a calculator. *Building and Enviroment*, 37:415–419, 2002.

[59] Sergio Manuel Pineda. Analytical and experimental study of a liquid desiccant heat and mass exchanger operating near water freezing temperature. Master's thesis, Mechanical Engineering, University of California, Merced, April 2009.

[60] M. S. Park, John R. Howell, Gary C. Vliet, and John L. Peterson. Coupled heat and mass transfer between a falling desiccant film and air in cross flow: Part i - numerical model and experimental results. *AIAA/ASME Heat Transfer Conf. Colorado Springs*, 275:81–90, 1994.

[61] M. S. Park, Gary C. Vliet, and John R. Howell. Coupled heat and mass transfer between a falling desiccant film and air in cross flow: Part ii - parametric analysis and results. *AIAA/ASME Heat Transfer Conf. Colorado Springs*, 275:73–79, 1994.

[62] J. Navarro-Esbri, R. Cabello, and E. Torrella. Experimental evaluation of the internal heat exchanger influence on a vapour compression plant energy efficiency working with R22, R134a, and R407C. *Energy*, 30:621–636, 2010.

[63] Masafumi Nakagawa, Ariel R. Marasigan, and Takanori Matsukawa. Experimental analysis on the effect of internal heat exchanger in transcritical CO_2 refrigeration cycle with two-phase ejector. *International Journal of Refrigeration*, pages 1–10, 2010.

[64] D.E. Boewe, C.W. Bullard, J.M. Yin, and P.S. Hrnjak. Contribution of internal heat exchanger to transcritical R-744 cycle performance. *HVAC&R Research*, 7(2):155–168, 2001.

[65] Sung Goo Kim, Yoon Jo Kim, Gilbong Lee, and Min Soo Kim. The performance of a transcritical CO_2 cycle with an internal heat exchanger for hot water heating. *International Journal of Refrigeration*, 28:1064–1072, 2005.

[66] R. Vijayan and P.S.S. Srinivasan. Influence of internal heat exchanger on performance of window AC retrofitted with R407C. *Journal of Scientific and Industrial Research*, 68:153–156, 2009.

[67] Ciro Aprea and Angelo Maiorino. An experimental evaluation of the transcritical CO_2 refrigerator performances using an internal heat exchanger. *International Journal of Refrigeration*, 31:1006–1011, 2008.

[68] Jahar Sarkar. Review on cycle modifications of transcritical CO_2 refrigeration and heat pump systems. *Journal of Advanced Research in Mechanical Engineering*, 1:22–29, 2010.

[69] Manuel R. Conde. Aqueous solutions of lithium and calcium chlorides: Property formulations for use in air conditioning equipment design. M. Conde Engineering, Zurich Switzerland, 2004.

[70] Manuel R. Conde. Properties of aqueous solutions of lithium and calcium chlorides: formulations for use in air conditioning equipment design. *Int. J. Thermal Sci.*, 43(4):367–382, 2004.

[71] Gerardo Diaz. Numerical investigation of transient heat and mass transfer in a parallel-flow liquid-desiccant absorber. *Heat and Mass Transfer*, 46:1335–1344, 2010.

[72] Nelson Fumo and D. Y. Goswami. Study of an aqueous lithium chloride desiccant system: air dehumidification and desiccant regeneration. *Solar Energy*, 72(4):351–361, 2002.

[73] D.I. Stevens, J.E. Braun, and S.A. Klein. An effectiveness model of liquid-desiccant system heat/mass exchangers. *Solar Energy*, 42(6):449–455, 1989.

[74] Jesse D. Killion and Srinivas Garimella. A critical review of models of coupled heat and mass transfer in falling-film absorption. *International Journal of Refrigeration*, 24(8):755 – 797, 2001.

[75] G. Grossman. Analysis of interdiffusion in film absorption. *International Journal of Heat and Mass Transfer*, 30:205–208, 1987.

[76] G. Grossman. Simultaneous heat and mass transfer in film absorption under laminar flow. *International Journal of Heat and Mass Transfer*, 26(3):357 – 371, 1983.

[77] Vikas Patnaik and Horacio Perez-Blanco. A study of absorption enhancement by wavy film flows. *International Journal of Heat and Fluid Flow*, 17(1):71 – 77, 1996.

[78] L.P. Kholpanov and E.Ya. Kenig. Coupled mass and heat transfer in a multicomponent turbulent falling liquid film. *International Journal of Heat and Mass Transfer*, 36(14):3647 – 3657, 1993.

[79] Hamza M. Habib and Byard D. Wood. Simultaneous heat and mass transfer in film absorption with the presence of non-absorbable gases. *Journal of Heat Transfer*, 123(5):984–989, 2001.

[80] Yong Tae Kang, Richard N. Christensen, and Kambiz Vafai. Analysis of absorption process in a smooth-tube heat exchanger with a porous medium. *Heat Transfer Engineering*, 15(4):42–55, 1994.

[81] Gommed K, Grossman G, and Koenig MS. Numerical study of absorption in a laminar falling film of ammonia-water. *Forthcoming in ASHRAE Transactions*, 2001.

[82] M.A. Leschziner. Modeling turbulent recirculating flows by finite-volume methodscurrent status and future directions. *International Journal of Heat and Fluid Flow*, 10(3):186 – 202, 1989.

[83] M. Zeng and W.Q. Tao. A comparison study of the convergence characteristics and robustness for four variants of simple-family at fine grids. *Engineering Computations*, 20(3):320 – 340, 2003.

[84] Heimo Walter. Dynamic simulation of natural circulation steam generators with the use of finite-volume-algorithms a comparison of four algorithms. *Simulation Modelling Practice and Theory*, 15(5):565 – 588, 2007.

[85] D.B. Spalding. A novel finite-difference formulation for differential expressions involving both first and second derivatives. *Int'l J. Num. Methods in Engineering*, 4:551–559, 1972.

[86] L.S. Caretto, R.M. Curr, and D.B. Spalding. Two numerical methods for three-dimensional boundary layers. *Computer Methods in Applied Mechanics and Eng.*, 1:39–57, 1972.

[87] A.K. Runchal. Convergence and accuracy of three finite difference schemes for a twodimensional conduction and convection problem. *Int'l J. Num. Methods in Engineering*, 4:540–550, 1972.

[88] S.V. Patankar. *Numerical Heat Transfer and Fluid Flow*. Hemisphere, Washington, 1980.

[89] S.D. Connell and P. Stow. The pressure correction method. *Computers & Fluids*, 14(1):1 – 10, 1986.

[90] H.S. Udaykumar, R. Mittal, P. Rampunggoon, and A. Khanna. A sharp interface cartesian grid method for simulating flows with complex moving boundaries. *Journal of Computational Physics*, 174(1):345 – 380, 2001.

[91] H. K. Versteeg and W. Malalasekera. *An introducction to computational fluid dynamics*. Prentice Hall, 2007.

[92] A.D. Ferreira, A.M.G. Lopes, D.X. Viegas, and A.C.M. Sousa. Experimental and numerical simulation of flow around two-dimensional hills. *Journal of wind engineering and industrial aerodynamics*, 55:173 – 181, 1995.

[93] H.S. Udaykumar, R. Mittal, and P. Rampunggoon. Interface tracking finite volume method for complex solid-fluid interactions on fixed meshes. *Communications in numerical methods in engineering*, 18:89 – 97, 2001.

[94] J. P. Van Doormaal and G. D. Raithby. Enhancements of the simple method for predicting incompressible fluid flows. *Numerical Heat Transfer*, 7(2):147–163, 1984.

[95] John D. Jr. Anderson. *Computational Fluid Dynamics*. McGraw-Hill, Inc., 1995.

[96] P.G. Drazin and W.H. Reid. *Hydrodynamic stability*. Cambrige Univ. Press, London, 1981.

[97] P.G. Drazin. *Introduction to Hydrodynamic stability*. Cambrige Univ. Press, New York, 2002.

[98] Vassilios Theofilis. Global linear instability. *Annual Review of Fluid Mechanics*, 43:319 – 352, 2011.

[99] J. Plateau. Statique experimentale et theorique des liquides soumis aux seules forces moleculaire. *Gauthier-Villars, Paris*, 1873.

[100] Francisco J. Solorio and Mihir Sen. Linear stability of a cylindrical falling film. *J. Fluid Mech.*, 183:365–377, 1987.

[101] L. Rayleigh. Scientific papers. *Cambridge University Press*, 3, 1902.

[102] O. Reynolds. An experimental investigation of the circumstances which determine whether the motion of water shall be direct or sinuous, and of the law of resistance in parallel channels. *Philos. Trans. R. Soc. London*, 174:935–82, 1883.

[103] Orr W.M. The stability or instability of the steady motions of a perfect liquid and a viscous liquid. *Proc. R. Irish Acad*, A 27:927, 69138, 1907.

[104] Sommerfeld A. Ein beitrag zur hydrodynamischen erklarung der turbulenten flussigkeitsbewegung. *In Atti del 4. Congr.Internat. dei Mat., Roma*, III:11624, 1908.

[105] Tollmien W. Uber die entstehung der turbulenz. *Nachr. Ges. Wiss. Gottingen, Math.- Phys.*, KI:2144, 1929.

[106] Schlichting H. Zur entstehung der turbulenz bei der plattenstromung. *Nachr. Ges. Wiss. Gottingen, Math.- Phys.*, KI:181208, 1933.

[107] P.A.M. Boomkamp and R.H.M. Miesen. Nonaxisymmetric waves in core-annular flow with a small viscosity ratio. *Physics of Fluids A*, 4(8):1627–1636, 1992.

[108] P.A.M. Boomkamp and R.H.M. Miesen. Classification of instabilities in parallel two-phase flow. *International Journal of Multiphase Flow*, 22, Supplement(0):67 – 88, 1996.

[109] P.A.M. Boomkamp, B.J. Boersma, R.H.M. Miesen, and G.V. Beijnon. A chebyshev collocation method for solving two-phase flow stability problems. *Journal of Computational Physics*, 132(2):191 – 200, 1997.

[110] P.A.M. Boomkamp. *Stability of parallel two-phase flow*. Universiteit Twente, Netherlands, 1998.

[111] R. V. Craster and O. K. Matar. Dynamics and stability of thin liquid films. *Rev. Mod. Phys.*, 81:1131–1198, Aug 2009.

[112] H.-C. Ku and D. Hatziavramidis. Solutions of the two-dimensional navier-stokes equations by chebyshev expansion methods. *Computers and Fluids*, 13(1):99–113, 1985.

[113] Michael D. Greenberg. *Advanced Engineering Mathemathics*. Prentice Hall, 1998.

[114] Abdelfattah Zebib. A chebyshev method for the solution of boundary value problems. *Journal of Computational physics*, 53:443–455, 1984.

[115] Chia-Shun Yih. Stability of parallel laminar flow with free surface. *Quart. Appl. Math.*, 12(434):623–628, 1955.

[116] Chia-Shun Yih. Stability of liquid flow down an inclined plane. *The physics of Fluids*, 6(3):321–334, 1963.

[117] Chia-Shun Yih. Wave formation on a liquid layer for de-icing airplane wings. *J. Fluid Mech.*, 212:41–53, 1990.

[118] R.E. Kaplan. Report asrl-tr. *Mass. Inst. Tech., Aeroelastic and Structures LAb.*, 116-1, 1964.

[119] L.H. Lee and W.C. Reynolds. Variational method for investigating the stability of parrallel flow. *Q.J. Mech. appl. Math*, 20(1), 1967.

[120] Williams R. Calderon-Munoz, Debdeep Jena, and Mihir Sen. Temperature influence on hydrodynamic instabilities in a one-dimensional electron flow in semiconductors. *Journal of applied physics*, 107, 2010.